ERUPTIONS AND JETS IN THE SUN

Eon Jui Lee

A Thesis Submitted for the Degree of PhD
at the
University of St Andrews

2017

Eruptions and Jets in the Sun

Eon Jui Lee

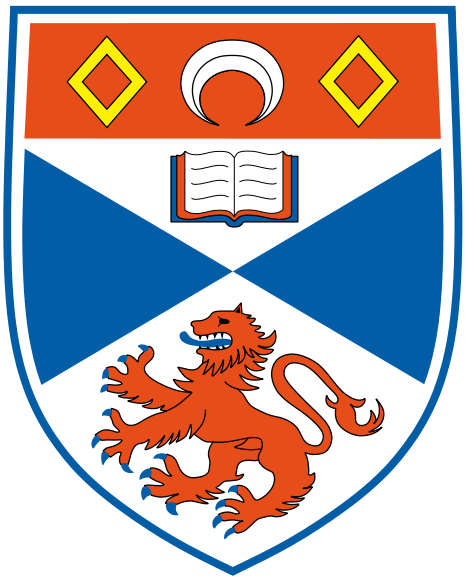

Thesis submitted for the degree of Doctor of Philosophy

of the University of St Andrews

26 Sept 2016

Declarations

Candidate's Declarations

I, Eon Jui Lee, hereby certify that this thesis, which is approximately 25,000 words in length, has been written by me, and that it is the record of work carried out by me and that it has not been submitted in any previous application for a higher degree.

I was admitted as a research student in September 2012 and as a candidate for the degree of Doctor of Philosophy in September 2012; the higher study for which this is a record was carried out in the University of St Andrews between 2012 and 2016.

Date: _____ Signature of Candidate: _____.

Supervisor's Declaration

I hereby certify that the candidate has fulfilled the conditions of the Resolution and Regulations appropriate for the degree of Doctor of Philosophy in the University of St Andrews and that the candidate is qualified to submit this thesis in application for that degree.

Date: _____ Signature of Supervisor: _____.

Permission for Publication

In submitting this thesis to the University of St Andrews we understand that we are giving permission for it to be made available for use in accordance with the regulations of the University Library for the time being in force, subject to any copyright vested in the work not being affected thereby. We also understand that the title and the abstract will be published, and that a copy of the work may be made and supplied to any bona fide library or research worker, that my thesis will be electronically accessible for personal or research use unless exempt by award of an embargo as requested below, and that the library has the right to migrate my thesis into new electronic forms as required to ensure continued access to the thesis. We have obtained any third-party copyright permissions that may be required in order to allow such access and migration, or have requested the appropriate embargo below.

PRINTED COPY

Embargo on all or part of print copy for a period of 1 year (maximum five) on the following ground(s):

Publication would preclude future publication

ELECTRONIC COPY

Embargo on all or part of electronic copy for a period of 1 year (maximum five) on the following ground(s):

Publication would preclude future publication

Date: _____ Signature of Candidate: _____ Signature of Supervisor: _____.

Acknowledgements

Firstly, I would like to thank my main supervisor Vasilis Archontis for the continuous support during my PhD study. I would like to thank him also for his patience, motivation, and immense knowledge. I would also like to thank my second supervisor, Alan Hood, who introduced me into the field of Solar Physics, and for all the help and continuous support he has provided me. A sincere thanks also goes to Petros Syntelis for all his help and encouragement. They have all helped me a lot during the whole period of my PhD research. Without this support, the completion of my PhD thesis would not have been possible.

I don't forget the help and support by the whole Solar and Magnetospheric Theory Group. I have also found that the weekly seminars provided me with extra knowledge and ideas on different research topics, which sometimes were closely related to my topic of research. They have been extremely helpful to me.

I would also like to thank all the friends I've met in the last four years, for making my life in St Andrews so wonderful. Last but not least, I would like to thank my family for supporting me spiritually throughout writing this thesis and my life in general.

Abstract

Magnetic flux emergence is a fundamental process in the Sun, during which magnetic fields emerge from the solar interior to the surface, to build up active regions and give onset to spectacular dynamic phenomena, such as eruptions and jets. In this thesis, we performed 3D, resistive MHD simulations to study the emergence and the associated magnetic activity of a quadrupolar region in the Sun. Our aim behind the setup of this initial condition (i.e. a quadrupolar region) was to study a magnetic field configuration, which has not been studied in detail before, although it has been repeatedly observed in the Sun and it has been shown that it can host intense magnetic activity (e.g. in the form of jets, flares and eruptions).

The results of our experiments showed that the internal dynamics of such regions leads to the onset of eruptions in the form of twisted magnetic flux tubes (flux ropes). These eruptions are recurrent but they cannot escape the outermost field of the emerging flux (envelope field). They remain confined within the envelope field, as the downward tension of the outermost field lines overwhelms the upward Lorentz force of the erupting field. When we add an ambient magnetic field in the solar atmosphere, external reconnection between the emerging and the ambient field triggers the emission of (standard) reconnection jets. The external reconnection also releases the tension of the ambient field lines and, thus, the eruptions move in an ejective way towards the outer space. Namely, the confined eruptions become ejective eruptions, which escape from the numerical domain. These ejective eruptions drive a newly observed class of jets, the so called "blowout" jets. Our experiments reproduce some of the main observed characteristics of the "blowout" jets. We showed that "blowout" jets emit hot and cool plasma into the outer solar atmosphere simultaneously, and they undergo untwisting motion due to the relaxation of twist during their ejection. We found that the untwisting motion of the "blowout" jets is associated with the propagation of torsional Alfvén waves. Finally, we performed a parametric study to explore the effect of the ambient field strength on the onset and dynamics of the eruptive events. We found that one of the main effects is that the stronger ambient field suppresses the vertical expansion of the magnetic envelope of the quadrupolar region due to the higher magnetic pressure above it. This result has an effect on the emission of jets, which are emitted due to reconnection between the two fields. When the ambient field is relatively weak, it is pushed away from the strong emerging field and reconnection between them is not so persistent. On the other hand, when the ambient field is

relatively strong, we find that more jets are ejected due to more efficient and more frequent reconnection between the two flux systems. As a consequence, we find that more mass and flux is being transferred into the solar corona by the reconnection jets. Also, we find that there are more eruptions when the ambient field is stronger. The study of the total energy flux carried by the jets showed that it is sufficient to provide the energy required to accelerate the high speed solar wind. This indicates that the "blowout" jets may play an important role in driving the solar wind.

Contents

List of Figures

Chapter 1

Introduction

1.1 The Sun

The Sun is the only star in our solar system, which then provides heat and light to our planet Earth. The Sun weighs $1.99 \times 10^{30}\,\mathrm{kg}$ or $333,000$ times the weight of Earth, and its mass is roughly 99% of the mass in the solar system. The diameter of the Sun is $1.39 \times 10^{6}\,\mathrm{km}$, about 109 times the diameter of the Earth. Now, the Sun is a middle age star, at about $4.6\,\mathrm{billion}$ years old. It is made up of hot plasma, and it mainly consists of hydrogen (73.46%) and helium (24.85%), the rest includes oxygen, carbon, iron and other elements (Eddy et al., 1979).

1.1.1 Solar Interior

The Sun's interior cannot be observed directly as we cannot see through its optically thick surface. Thus, it is mainly explored by using methods of helioseismology, which are typically based on the propagation of wave oscillations inside the Sun combined with surface observations. It is widely believed that the Sun's interior consists of three broad layers (Figure 1.1b), which we briefly describe below.

The innermost layer is the core, and through helioseismology, the core is defined to be within $0.2 \sim 0.25R_{\odot}$, where $R_{\odot}$ is the solar radii (García et al., 2007). The energy on the Sun is mainly generated through nuclear fusion, where hydrogen nuclei are converted into helium nuclei, and this mainly happens in the core. The core also has the highest temperature and density in the Sun, with temperature reaching up to $1.5 \times 10^{7}\,\mathrm{K}$, and density up to $150\,\mathrm{g\,cm^{-3}}$.

Between $0.25R_{\odot}$ and $0.7R_{\odot}$ lies the radiative zone, about $300,000\,\mathrm{km}$ thick, where the temperature drops from $1.5 \times 10^{7}\,\mathrm{K}$ to $1.5 \times 10^{6}\,\mathrm{K}$ and density drops from $20\,\mathrm{g\,cm^{-3}}$ to $0.2\,\mathrm{g\,cm^{-3}}$,

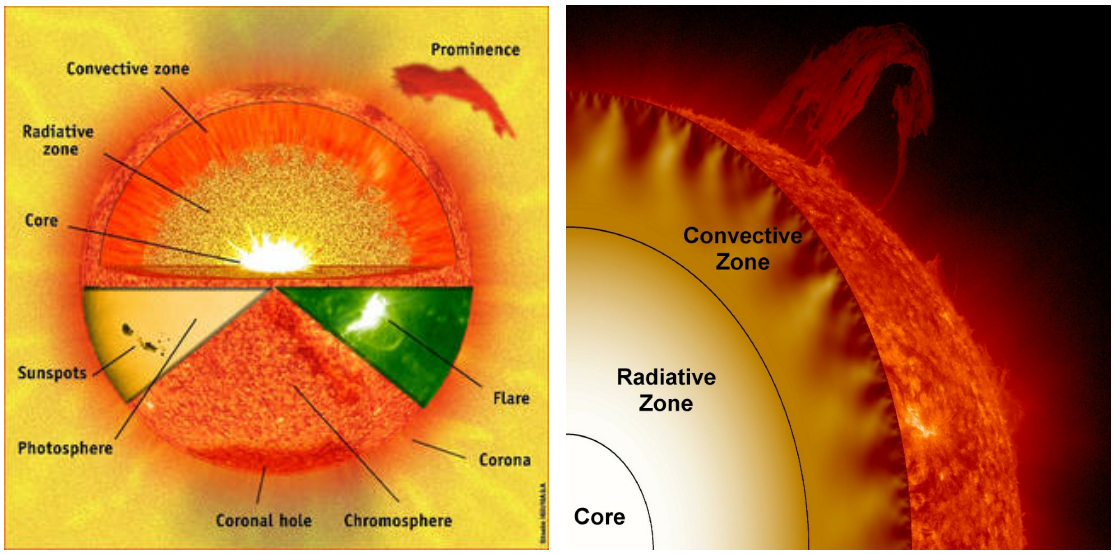

(a) (b)

Figure 1.1: (a) The overview of Sun's structure. (Image credit: `http://www.nasa.gov/mission_pages/sunearth/spaceweather/index.html`) (b) The Sun's interior layers. (Image credit: `http://solarscience.msfc.nasa.gov/interior.shtml`)

from the bottom to the top of the radiative zone (Elkins-Tanton, 2006). The energy generated from the core is transported to the top of the radiative zone by radiative diffusion. Due to the high density in radiative zone, the high frequency gamma rays consisting of high energy photons produced in the core, collide with other particle while passing through the radiative zone. During this process, the frequency is lowered down and the wavelength is increased, and energy is released. The motion of the photons is considered to follow a random walk motion, and in average it would take up to 1.7×10^5 years for the photon to escape from the radiative zone into the higher layer in the Sun.

Above the radiative zone lies a thin transition layer, called the tachocline. Above the tachocline at the convection zone, the rotation rate differs along latitude: at the equator the rotation rate is much higher than at the poles; whereas beneath the tachocline at the radiative zone, the rotation rate remains constant. The rapid change in the rotation rate has caused the tachocline to be a transition layer with a large shearing motion. The tachocline is about $0.04R_\odot$ thick. It is currently believed that the large shearing motion in the tachocline generates and strengthens the large scale magnetic fields in the convection zone (see Fan, 2004, and the references therein).

The convection zone is the outer layer of the solar interior, lying above the tachocline, which is about $200,000\,\mathrm{km}$ thick. The temperature in the convection zone drops from $1.5 \times 10^6\,\mathrm{K}$ at the base of the convection zone to $5,700\,\mathrm{K}$ at the top of the convection zone, and the density drops from $0.2\,\mathrm{g\,cm^{-3}}$ to $2 \times 10^{-7}\,\mathrm{g\,cm^{-3}}$. The temperature is not high enough for some heavier ions to be fully ionised and hence the efficiency of radiative diffusion has decreased, and the energy is

mainly transported through convection motions. The material at the base of the convection zone is heated and expands, lowering the density and hence rises towards the surface. The density then increases again when it cools down at the surface, and hence it sinks down to the base of convection zone again.

1.1.2 Solar Atmosphere

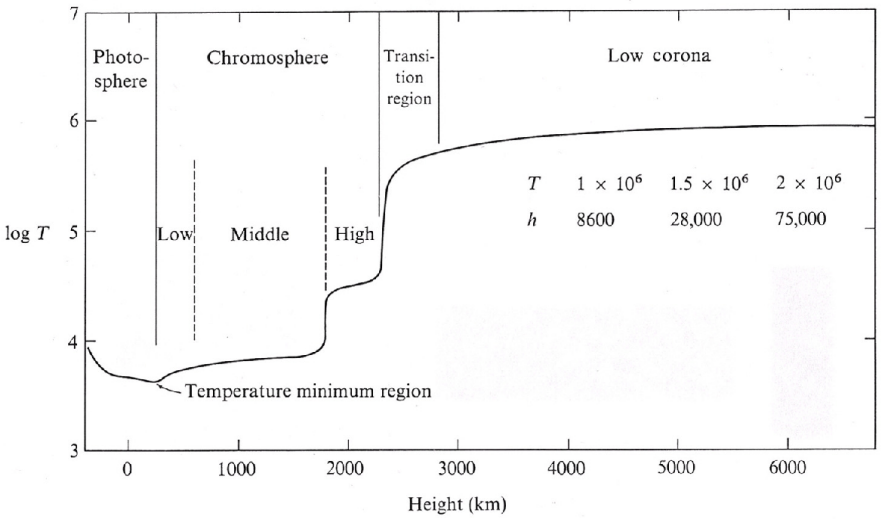

Figure 1.2: Temperature distribution in the solar atmosphere. (Athay, 1976)

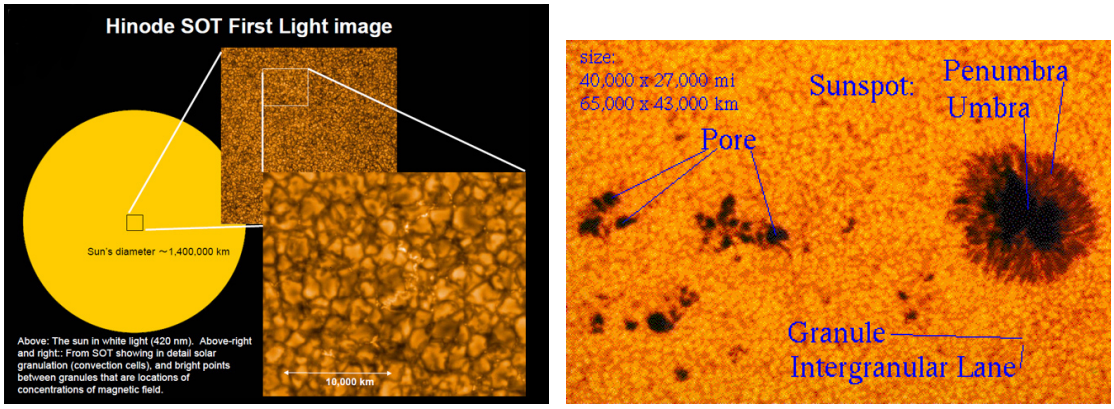

(a) (b)

Figure 1.3: Image showing granules, solar pores, and sunspots. (a) Hinode SOT white light image showing the granules. (Image credit: `http://global.jaxa.jp/press/2006/10/20061031_hinode_e.html`) (b) The sunspot, solar pores & granule observed on the photosphere. (Image credit: `http://starchild.gsfc.nasa.gov/docs/StarChild/questions/question17.html`)

The photosphere is the visible surface of the Sun, and it is often considered as the innermost

layer of the solar atmosphere. The photosphere has the following properties: average temperature of $5,700\,\mathrm{K}$, average density around $2 \times 10^{-7}\,\mathrm{g\,cm^{-3}}$, and average thickness of $500\,\mathrm{km}$. The temperature in photosphere decreases along height, as shown in Figure 1.2. The photosphere includes some important features observed on the Sun, such as granules, supergranules and sunspots. Granules are the small cellular features which are at the top of the convection cells in the convection zone, and have an average diameter of $1,000\,\mathrm{km}$ with average lifetime of $8\,\mathrm{min}$. (see Figure 1.3a) Supergranules are the larger versions of granules, with an average diameter of $1.6 \times 10^4\,\mathrm{km}$ and average lifetime of $24\,\mathrm{hr}$ (Leighton et al., 1962).

Sunspots are features that appear to be dark spots on the photosphere, with a lower temperature than the surrounding area, and they typically live for a few days or even up to a few weeks, with sizes in the range $16\,\mathrm{km}$ to $1.6 \times 10^5\,\mathrm{km}$. Sunspots normally appear as pairs, one with positive polarity and the other with negative polarity. The dark region in sunspot is called umbra, and the penumbra is the relatively light region surrounding the umbra (see Fig 1.3b). Sunspots without penumbra are called solar pores. Sunspot groups are widely known to be classified by the Mount Wilson magnetic classification (Hale et al., 1919; Hale and Nicholson, 1938). According to the sign of the embedded magnetic polarities, sunspot groups are classified into four different types:

1. α: unipolar sunspot group, sunspot group that contains only one polarity.
2. β: bipolar sunspot group, sunspot group that contains both positive and negative polarities.
3. γ: complex sunspot group, the sunspot has intermixed polarities and that it is too complex to be classified as a simple bipolar sunspot.
4. δ: inside a single penumbra of the sunspot contains both positive and negative polarities.

The original definition of the classification suggested by Hale et al. (1919) includes only the first three types of sunspot groups, α, β and γ. The idea of the δ sunspot classification in addition to the original three classes is proposed by Künzel (1965), where he named the δ sunspot to be a sunspot that contains different polarities of umbra in a single penumbra.

Above the photosphere lies the chromosphere, which is about $1,500\,\mathrm{km}$ thick. The temperature in chromosphere decreases to around $3,800\,\mathrm{K}$ (Avrett, 2003) before rising to about $3 \times 10^4\,\mathrm{K}$ at the top of the chromosphere. The density decreases along height, from about $2 \times 10^{-7}\,\mathrm{g\,cm^{-3}}$ at the base of chromosphere to about $1.6 \times 10^{-14}\,\mathrm{g\,cm^{-3}}$ at the top of the chromosphere (Kontar et al., 2008). Several features are observed in the chromosphere, such as prominences, filaments and spicules. Prominences are bright arcade structures observed at the solar limb (see Figure 1.5a), which are cool and dense chromospheric materials supported by the magnetic field loops, and have a typical length scale of $10^4 \sim 10^5\,\mathrm{km}$ (Hansen and Bellan, 2001). Due to the temperature being significantly lower than the surrounding corona, they appear to be bright when observed in the

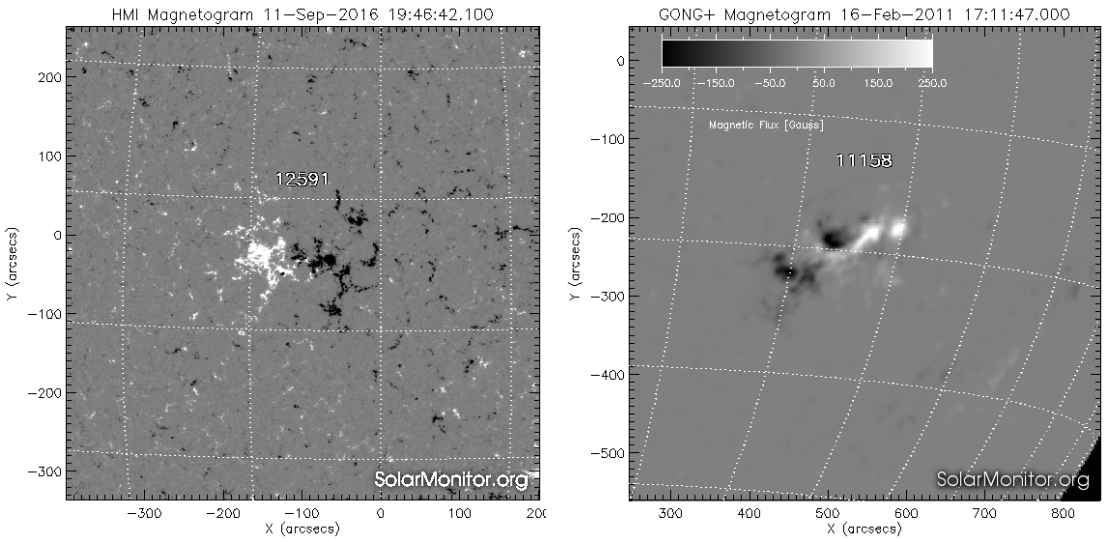

(a) (b)

Figure 1.4: Image showing sunspots of different magnetic configurations. (a) A sunspot with a β magnetic configuration observed on 11 Sept 2016 by SDO/HMI. (Image credit: `https://www.solarmonitor.org/index.php?date=20160911&region=12591`) (b) A sunspot with a $\beta\gamma\delta$ magnetic configuration observed on 16 Feb 2011 by the Global Oscillation Network Group (GONG). (Image credit: `https://www.solarmonitor.org/region.php?date=20110216&type=1&region=11158`)

chromospheric temperature line (e.g. He II 304Å). Prominences root into the solar surface at the photosphere, and extend into the corona, sometimes reaching up to $1.5 \times 10^5\,\mathrm{km}$. The formation of prominences takes days, and after their formation, they may stay stable for weeks or even months (Parenti, 2014). When the magnetic loops change along time, the prominence is then either drained down into photosphere or erupts and it evolves into a Coronal Mass Ejection (CME), which are often associated with solar flares. Filaments are the same features as prominences, but they are observed on disk rather than above the solar limb (See Figure 1.5b). They appear to be dark structures, due to their lower temperature compared to the surrounding plasma.

The other main feature observed in the chromosphere is spicules. Spicules were first described by Secchi (1877) and they were named as spicules by Roberts (1945). Spicules are observed at the solar limb as bright features in the Hα and $\mathrm{Ca_{II}}$ images. Typically, they are classified into type-I and type-II (e.g. (de Pontieu et al., 2007)). Type-I spicules have a lifespan of $3 - 7\,\mathrm{min}$ with usually a maximum velocity of $40\,\mathrm{km\,s^{-1}}$, and have a parabolic trajectory, i.e. they fall back to the chromosphere after being ejected. They are driven by shock waves and they are formed as a result of p-mode waves. Type-II spicules are a type of spicule that are much more dynamic with a much shorter lifespan of $10 - 150\,\mathrm{s}$. They have a velocity of $50 - 150\,\mathrm{km\,s^{-1}}$, and they fade away after time due to being heated up to at least transition region temperatures while being ejected. The driver of the type-II spicules is thought to be magnetic reconnection, as a result of the

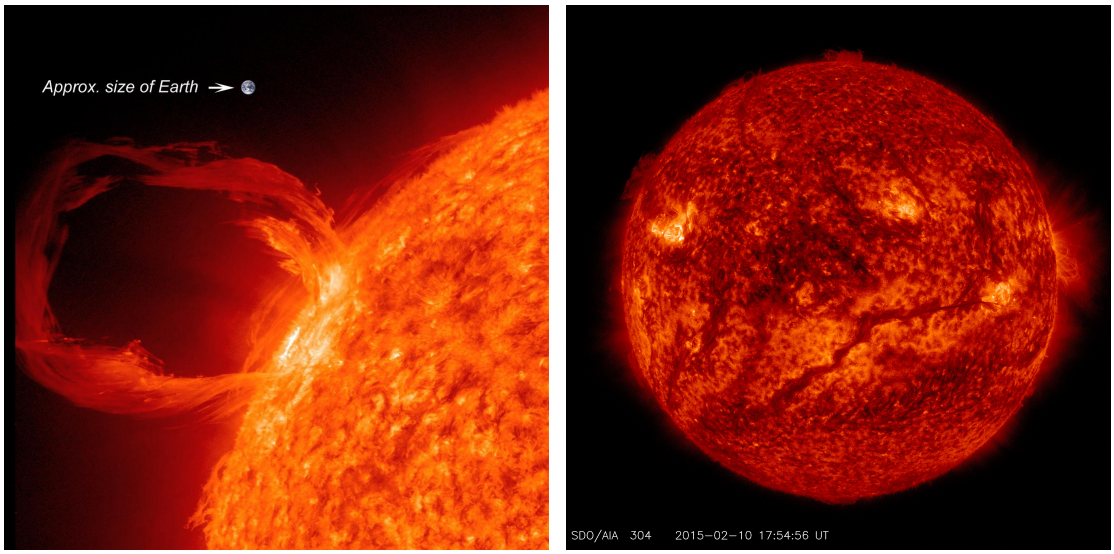

(a) (b)

Figure 1.5: Image showing a prominence/filament. When observed over the solar limb, it is called a prominence; when observed on the solar disk, it is called a filament. (a) An eruptive prominence observed by SDO/AIA 304Å on 30 March 2010. (Image credit: `http://www.nasa.gov/mission_pages/sunearth/spaceweather/index.html`) (b) A filament observed by SDO/AIA 304Å on 10 February 2015. (Image credit: `http://www.nasa.gov/content/goddard/sdo-sees-giant-filament-on-the-sun`)

interaction between photospheric flux concentrations of opposite polarities. In De Pontieu et al. (2011), they suggested that the type-II spicules might play an important role in the heating of the solar corona.

In between the chromosphere and corona, there lies a thin and very irregular layer called the transition region, which is about $100\,\mathrm{km}$ thick. Within the transition region, the temperature rises from $3 \times 10^4\,\mathrm{K}$ to about $5 \times 10^5\,\mathrm{K}$. Above the transition region, there is the corona layer, where the temperature ranges from $5 \times 10^5\,\mathrm{K}$ to $\mathcal{O}(10^6)\,\mathrm{K}$. The exact mechanism for the heating of the solar corona remains unknown and it is currently one of the big open questions in solar physics. The corona starts at about $2,100\,\mathrm{km}$ above the solar surface, and it does not have an upper boundary. Coronal loops are observed in the corona, and mostly around sunspots and active regions. They are bright arcade structures formed by closed magnetic field lines which are anchored in the photosphere, and they contain hot plasma. Depending on the magnetic field structure, a region on the Sun can be divided into an active region (AR), a coronal hole (CH), and a quiet Sun region (QS). Active regions are areas on the Sun with very strong and highly dynamic magnetic fields. Active regions can host most (if not all) of the known dynamic features on the Sun, i.e. sunspots which are observed in the photosphere, spicules and filaments (prominences) in the chromosphere, and flares and CMEs in the corona. Coronal holes are areas where the Sun's corona appears to be darker than the surrounding, due to lower density, and it is mostly observed at the solar poles.

The magnetic field structure in the coronal holes have a weaker field and it also has an 'open' configuration, which then allows solar particles to escape. The low density in the coronal region also helps the escape of the solar particles, which then builds up into high speed solar winds. The high speed solar winds are a major source of energy loss in coronal holes. Quiet Sun regions are the regions that are neither active regions nor coronal holes.

1.2 Coronal Jets

1.2.1 Observations

A common phenomena observed on the Sun is jets. Jets are small-scale emissions of plasma into the higher atmosphere with high speeds ($20 - 1000\,\mathrm{km\,s^{-1}}$). Observations of coronal jets are more prominent in coronal holes, since coronal holes appear to be darker than the surrounding area. Over the last 30 years, coronal jets are studied in detail based on the observation data from different space missions showing their formation and evolution (e.g. *Yohkoh*, *SOHO*, *TRACE*, *STEREO*, *Hinode*, *SDO* etc.). The higher spatial and temporal resolution in the recent space missions (e.g. *Hinode*, *SDO*) have provide us with a better understanding of the morphology of the jets.

Coronal jets were first described as coronal disturbances by Demastus et al. (1973), who observed them using ground based, green-line observations. Following the launch of *Skylab* in 1973, macrospicules with EUV wavelengths were observed and reported in Bohlin et al. (1975); Withbroe et al. (1976). Macrospicules are spike-like structures with features very similar to chromospheric spicules, except with a relatively larger size and longer lifetime ($5 - 40\,\mathrm{min}$), and hence the name macrospicules. Brueckner and Bartoe (1978, 1983) have then suggested that coronal jets might be the source to coronal heating (e.g. through shock waves accompanying the jets) and also to the acceleration of high speed solar winds, as they are able to balance out the energy and mass flux loss in the corona.

Coronal jets were studied in more detail after the launch of the *Yohkoh* satellite (Solar-A mission) in 1991. Through the Soft X-Ray Telescope (SXT) on board the *Yohkoh* satellite (Tsuneta et al., 1991), the solar corona was observed in the X-ray wavelength with a spatial resolution of $2.5''$ pixel size. Through the SXT, several features in the corona were observed, e.g. X-ray jets (Shibata et al., 1992a, 1994, 1996; Shimojo et al., 1996, 1998).

Shibata et al. (1992a) first reported the observations of the X-Ray jets through the *Yohkoh*/SXT, showing the typical size of a coronal X-Ray jet to be $5 \times 10^3 - 4 \times 10^5\,\mathrm{km}$, translational velocity to be $30 - 300\,\mathrm{km\,s^{-1}}$, and estimated kinetic energy to be of the order $\mathcal{O}(10^{25}) - \mathcal{O}(10^{28})\,\mathrm{erg}$. They reported that many of the X-Ray jets are associated with flaring in the X-Ray bright points

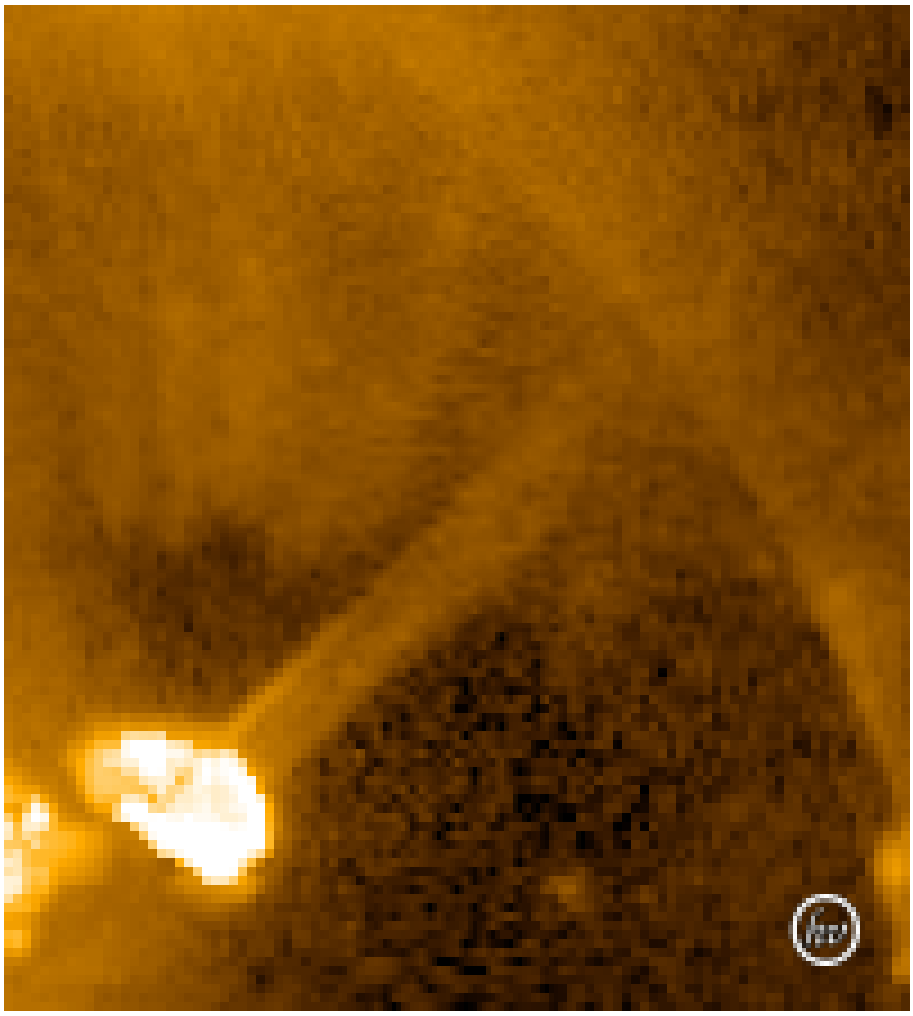

Figure 1.6: X-Ray jet observed by *Yohkoh*/SXT at $11:28:20$ UT on 12 November 1991 with filter (Al/Mg/Mn). (Image credit: `http://helioviewer.org/`)

(XBP), emerging flux region (EFR), or active regions. They observed a void in the SXT images at the footpoint of the jet following the ejection. They also showed the co-existence of cool Hα surges and X-Ray emission. They also proposed a model as a possible scenario of the emission of the jet (Section 1.2.2). Figure 1.6 shows an image of the X-Ray jet while being emitted. Both the jet spire and bright point at the base is seen. This is the jet reported in (Fig. 1 Shibata et al., 1992a).

Shibata et al. (1994) reported on a coronal hole X-Ray jet ejected on 11 January 1992, which is one of the largest coronal X-Ray jets observed until then. The jet is reported to be greater than 3×10^5 km in length, and is ejected from an "anemone-type" active region in a coronal hole. The jet is described to have an inverted-Y shape configuration. Shimojo et al. (1996) carried out a statistical study of 100 X-Ray jets observed by SXT from November 1991 to April 1992. They concluded that: (1) most of the jets are associated with small flares at the footpoints; (2) the jets

are few $\times 10^4 - 4 \times 10^5$ km in length and $5 \times 10^3 - 10^5$ km in width; (3) average outflow of jet is $\sim 200\,\mathrm{km\,s^{-1}}$; (4) the lifetime of the jets ranges between few minutes and 10 hours, with the distribution of the observed lifetime to be a power law with an index of ~ 1.2; (5) the jet is highly collimated in the direction of the flow.

The Extreme-ultraviolet Imaging Telescope (EIT) onboard *Solar and Heliospheric Observatory* (*SOHO*) have shown high temporal resolution observation of the polar coronal holes, and showed EUV jets similar to the X-Ray jets observed with *Yohkoh*/SXT (Moses et al., 1997; Wang et al., 1998). Wang and Sheeley (2002) studied the coronal white-light jets observed on the Large Angle and Spectrometric Coronagraph (LASCO) onboard *SOHO* during the 1996-1997 solar maximum period. They reported that comparing to the solar minimum period, the coronal jets observed during solar maximum are brighter, wider, and they are also distributed over a wider range of latitudes. They find that many of the jets originate from the active regions located inside or near the boundary of the equatorial coronal holes, comparing to the jets originating mostly from polar regions during solar minimum.

The observations from the *Transition Region and Coronal Explorer* (*TRACE*) satellite have shown higher spatial and temporal resolution of the EUV jets and they have provided more details of the jets (Alexander and Fletcher, 1999). Alexander and Fletcher (1999) shows simultaneous ejections of both cool ($\sim 1 \times 10^5$ K) and hot ($\sim 1 \times 10^6$ K) plasma during the emission of coronal jets. They reported observations of jets with both one-sided (single spire) anemone-type and two-sided loop (two spires) morphology, and they concluded that the form of the jet is decided by the inclination angle of the ambient field which the emerging loop interacts with. A one-sided anemone-type jet is ejected if the ambient field is vertical or oblique, and a two-sided loop jet is ejected if the field is predominantly horizontal. Chen et al. (2008, 2009) has reported that EUV (171Å) and UV (1600Å) jets are observed to be emitted above active regions where flux cancellation and flux emergence in the photosphere is found. The line-of-sight magnetograms are obtained from the Michelson Doppler Image (MDI) onboard *SOHO* (Scherrer et al., 1995).

Patsourakos et al. (2008) have reported on the observations of polar coronal jets from the Extreme Ultraviolet Imager (EUVI) of the Sun Earth Connection Coronal and Heliospheric Investigation (SECCHI) (Wuelser et al., 2004) onboard the *Solar Terrestrial Relations Observatory* (*STEREO*) satellites. They observed the helical structure of a jet from two different viewpoints (*STEREO*-A and *STEREO*-B) during the untwisting motion of the jet. This revealed the helical structure of the jet. A 3D MHD simulation was later carried out by Pariat et al. (2009) modelling the polar coronal jet, which was reported in Patsourakos et al. (2008). They reported a qualitative agreement between the simulations and observations of the jet. Nisticò et al. (2009) reported on a statistical study of the EUV coronal jets observed with EUVI/SECCHI onboard *SOHO* during March 2007 to April 2008 (solar minimum). Out of the 79 polar jets observed, 31 of them were reported to obtain a helical structure, showing a torsional motion around the propagation axis.

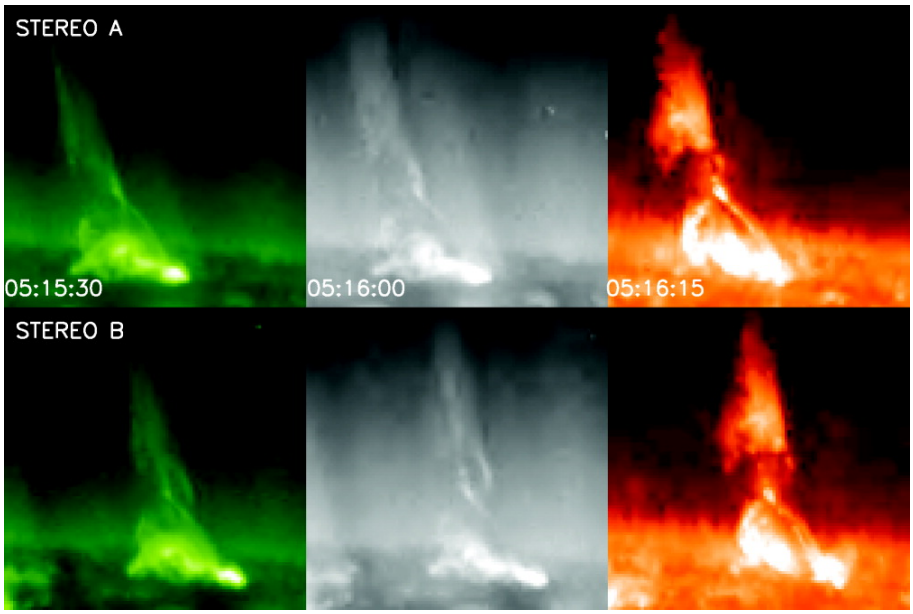

Figure 1.7: Simultaneous images of a jet in EUVI 195Å, 171Å, and 304Å channels (left, middle and right columns respectively) observed by *STEREO*-A and -B (top and bottom rows respectively). From Patsourakos et al. (2008). (Image credit: `http://iopscience.iop.org/article/10.1086/589769/meta`)

The *Hinode* satellite (Solar-B mission) was the successor to the *Yohkoh* mission, and it was launched in 2006 (Kosugi et al., 2007). The X-Ray Telescope (XRT) (Golub et al., 2007) and the Extreme-ultraviolet Imaging Spectrometer (EIS) (Culhane et al., 2007) on *Hinode* have provided unprecedented quality observations of the EUV and X-ray jets in coronal holes, of $1''$ spatial and $30\,\mathrm{s}$ temporal resolution, and also wide temperature coverage, between $1 \times 10^6\,\mathrm{K}$ to $3 \times 10^7\,\mathrm{K}$.

Cirtain et al. (2007) reported about the observations of polar coronal hole jets from the *Hinode*/XRT. They found that X-Ray jets were emitted much more frequently than previously observed. During their 100 hours of observations, an average of 10 jet events per hour were observed, compared to few events per day as previously reported (Shibata et al., 1996). The lifetime of the observed X-Ray jets ranges from $100 - 1500\,\mathrm{s}$. They have also discovered some of the jets with two velocity components. Apart from the typical outflow of $\sim 200\,\mathrm{km\,s^{-1}}$, they reported on the observation of high speed outflow of $\sim 800\,\mathrm{km\,s^{-1}}$, which is of the order of the local Alfvén speed during the initial phase of the ejection of the jet. It is interpreted as the evidence of plasma being ejected at Alfvén speed during the magnetic reconnection process. The observed X-Ray jets are also seen to undergo a transverse oscillation, with a period of $\sim 200\,\mathrm{s}$ and peak-to-peak magnitude of $8000\,\mathrm{km}$. Since in the corona the plasma is considered to be 'frozen' to the flux, the transverse motions of the jets would then indicate that the magnetic field undergoes a transverse motion, thus creating Alfvén waves. Figure 1.8 shows the evolution of a solar coronal jet.

Savcheva et al. (2007) carried out a statistical study based on the polar coronal hole jet events

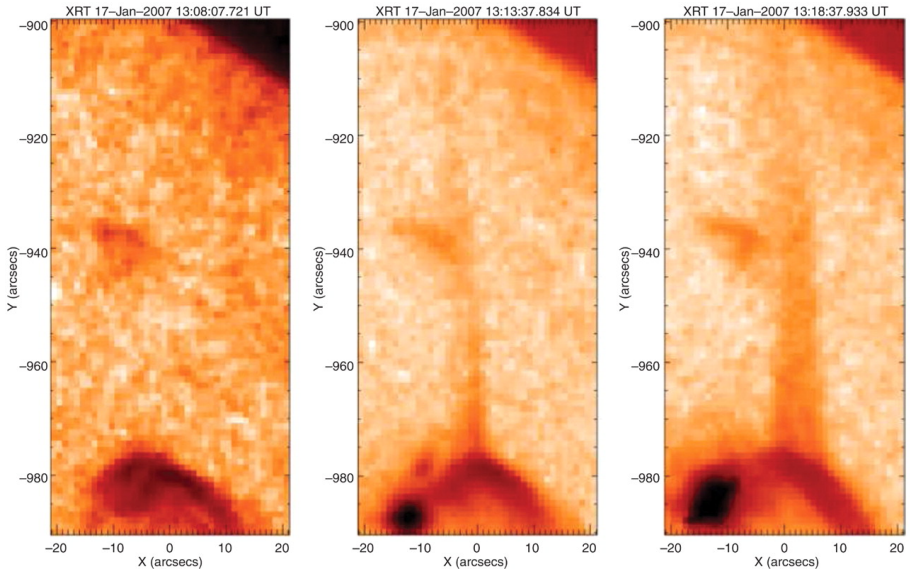

Figure 1.8: *Hinode*/XRT false-colour images of three stages of a jet's evolution. From Cirtain et al. (2007). (Image credit: `http://science.sciencemag.org/content/318/5856/1580.full`)

observed during 08-21 January 2007 by XRT. They showed that most of the jets have a maximum outward velocity of $\sim 160\,\mathrm{km\,s^{-1}}$, reaching up to a height of $\sim 5\times10^4\,\mathrm{km}$, width of $8\times10^3\,\mathrm{km}$, and lifetime of $10\,\mathrm{min}$. They also showed that the transverse velocity of the jet ranges in $0-35\,\mathrm{km\,s^{-1}}$.

Moore et al. (2010) introduced a dichotomy of polar coronal hole jets based on their morphology when observed in *Hinode*/XRT and *STEREO*/EUVI, categorizing solar jets into "standard" and "blowout" jets. The "standard" jets are the jets, which are formed based on the scenario described by Heyvaerts et al. (1977); Shibata et al. (1992a). From the *Hinode*/XRT images, the spire of the "standard" jets remains thin and narrow during their emission. The base of the jet is relatively dim and only a bright point is observed at one side of the jet's base, which is the jet's bright point (e.g. Fig 1.9). Most of the "standard" jets are not observed in the *STEREO*/EUVI 304Å, which indicates that there is no cool component ejected along the jet. In Fig 1.9, the first panel shows the emission (at $2\,\mathrm{min}$) before the jet event starts. The jet is being emitted at $16:54$ UT (second panel), and fades away at $17:04$ UT (last panel). Throughout the jet event, only a brightening at the base of the jet is seen, and is interpreted as the jet's bright point. The jet spire remained thin and narrow throughout the emission. The structure of a "standard" jet seems to consist of a thin spire that is anchored opposite to the bright point at the base arch.

In a "blowout" jet, X-Ray brightening is observed not only at the jet bright point as seen in the "standard" jet case, but also inside the base arch of the jet. As time evolves, an eruption emanates from the jet's base, containing cool plasma that can be observed in *STEREO*/EUVI 304Å. This

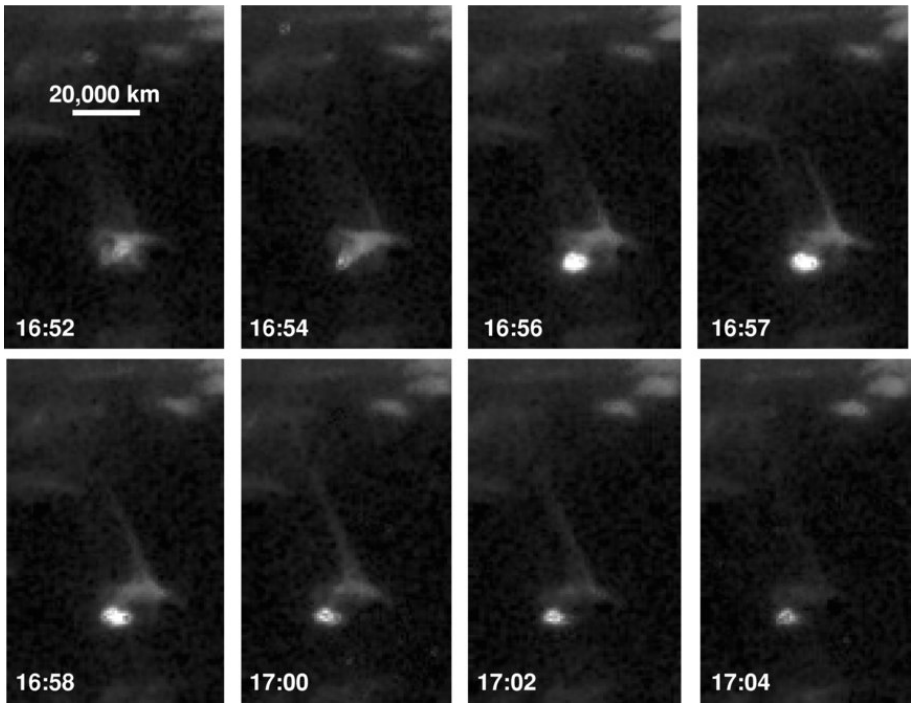

Figure 1.9: Progression of the "standard" jet of 22 September 2008 observed in coronal X-Ray images (Thin Al Poly filter) from *Hinode*/XRT. The lower left of each frame is the universal time in hours and minutes. From Moore et al. (2010). (Image credit: `http://iopscience.iop.org/article/10.1088/0004-637X/720/1/757/meta`)

results in the simultaneous emission of cool (EUVI 304Å) and hot (XRT) plasma along the jet. The jet spire of the "blowout" jet begins as a thin narrow channel, and then widens up following the eruption. The width of the jet channel gets as wide as the width of the jet's base (e.g. Fig 1.10). Fig 1.10 shows the progression of the "blowout" jet observed in coronal X-Ray images from *Hinode*/XRT. At $19:06$ UT (first panel), the jet event has not yet started. In the second panel at $19:09$ UT, the jet is being emitted with a thin and narrow jet channel. The formation of the flare arcade bright point is also seen at the base of the jet. The jet channel starts to widen up at $19:12$ UT (third panel), and also the brightening in the interior of the base arch is seen. The jet is seen to decay at $19:23$ UT.

Among the 55 polar coronal hole jets examined in Moore et al. (2010), they found that 34 of the jets are considered as "standard" jets, and 18 of the jets are considered as "blowout" jets, with the remaining 3 left ambiguous. They concluded that a certain amount of shear and twist along the base arch is required in order for the base arch to erupt open and undergo a "blowout" jet scenario. Moore et al. (2013) continued on the work and studied another 54 polar coronal hole X-Ray jets in between 2010 and 2011. The cool component of the jets are observed using the He II 304Å band of the Atmospheric Imaging Assembly (AIA) (Lemen et al., 2012) onboard *Solar Dynamics Observatory* (*SDO*) (Pesnell et al., 2012), with a higher spatial resolution of $0.6''$ pixel size and

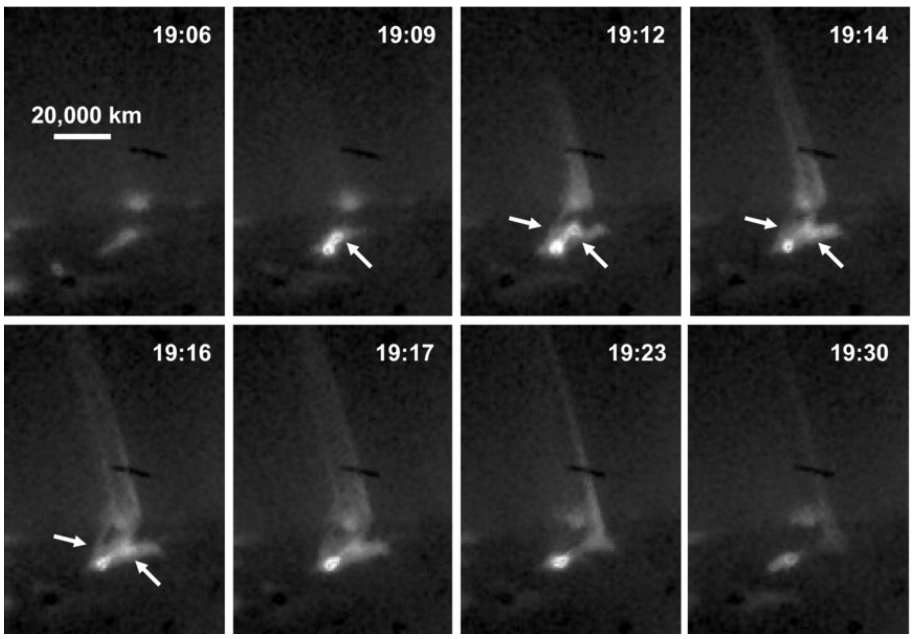

Figure 1.10: Progression of the "blowout" jet of 20 September 2008 observed in coronal X-Ray images (Thin Al Poly filter) from *Hinode*/XRT. The upper right of each frame is the universal time in hours and minutes. From Moore et al. (2010). (Image credit: `http://iopscience.iop.org/article/10.1088/0004-637X/720/1/757/meta`)

higher cadence of 12 s. They showed that among the newly studied 54 jets, 19 of them fall in the category of the "standard" jet, 32 of them in the "blowout" jet category, and the remaining 3 left ambiguous again. Combining this with the previous study (Moore et al., 2010), out of the 109 jets nearly half of them (53) are "standard" jets and another half of them (50) are "blowout" jets.

Liu et al. (2011); Hong et al. (2011); Shen et al. (2012); Adams et al. (2014); Young and Muglach (2014) all reported on observations of "blowout" jets. Liu et al. (2011) reported on the observation of the evolution of a jet from the "standard" stage to the "blowout" stage. Hong et al. (2011) reported on a "blowout" EUV jet which results from a mini-filament eruption in the quiet Sun region. They showed that the eruption was accompanied by a small flare-like brightening, a small coronal dimming, and also a micro-CME. Shen et al. (2012) suggested that the external reconnection between the emerging loop and the coronal field leads to the rising of the erupting filament.

Figure 1.11 shows time sequences of the "blowout" jet in various images: *BBSO* Hα images (top, cool), *SDO*/AIA 304Å images (middle, cool), *SDO*/AIA 193Å images (bot, hot). This figure shows simultaneous ejections in all three different lines which represents three different temperature ranges. This indicates that during the emission of the "blowout" jet, both hot and cool plasma are being ejected. The vertical short arrows in (b1), (c1), (d1) indicate the bright patch before the ejection, which may result from a small-scale reconnection event in the lower atmosphere.

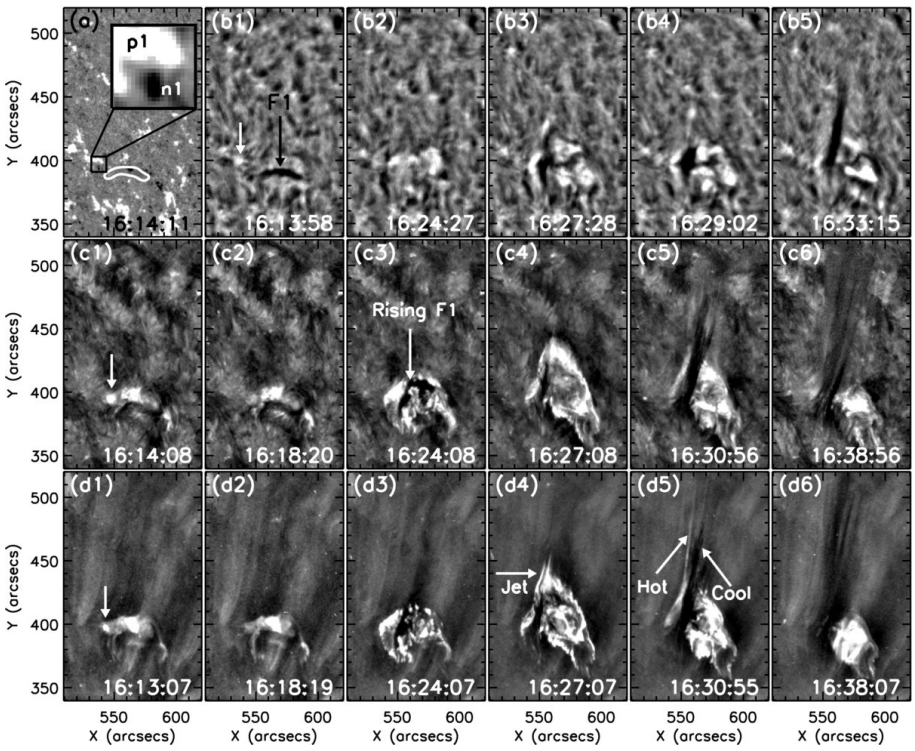

Figure 1.11: (a): HMI line-of-sight magnetogram just prior to the initiation of the jet, and the white contour is the profile of a filament, F1. (b1)-(b5): time sequences of *Big Bear Solar Observatory* (*BBSO*) Hα center; (c1)-(c6): *SDO*/AIA 304Å images; (d1)-(d6): *SDO*/AIA 193Å images, showing the "blowout" jet and the associated erupting filament at the base. From Shen et al. (2012). (Image credit: `http://iopscience.iop.org/article/10.1088/0004-637X/745/2/164/meta`)

Sterling et al. (2015) reports on the observations of 20 polar coronal hole X-Ray jets on both *Hinode*/XRT and *SDO*/AIA images. They claimed that all of the 20 jets originate from mini-filament eruptions. Namely, it is the mini-filament eruption that drives the reconnection, which leads to the emission of the jets. They proposed that both "standard" and "blowout" jets are triggered by the same mechanism, and that the type of the emitted jet depends on the strength of the eruption. If the mini-filament eruption is confined or weak, a "standard" jet is ejected; however if the eruption is strong enough, it opens up the overlying field and evolves into a "blowout" jet. Based on this theory they assume that there is a continuum of morphological jet types, from a pure "standard" jet to a full "blowout" jet.

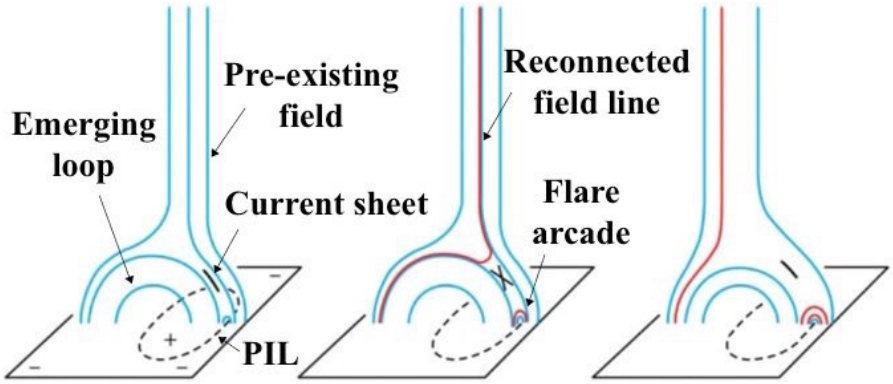

Figure 1.12: The standard reconnection scenario of coronal jets as described by Shibata et al. (1992a). From Moore et al. (2010). (Image credit: `http://iopscience.iop.org/article/10.1088/0004-637X/720/1/757/meta`)

1.2.2 Formation of Jets: Theory

"Standard" Jets

A schematic model of a possible scenario of the emission of the X-Ray jet is shown in Fig. 1.12 (Fig. 1 in Moore et al., 2010). They proposed that the X-Ray jet is ejected due to the magnetic reconnection between an emerging loop and the pre-existing coronal field. Initially a bipolar field emerges into a unipolar open ambient field, e.g. coronal hole.

Following the emergence of the bipolar field, a current sheet is formed in between the emerging loop and the ambient field, near the end of the emerging loop with an opposite polarity to the ambient field. As the bipolar field continues to emerge, part of the current sheet is then compressed and triggers a burst of reconnection, which then releases the free energy of the magnetic field around the current sheet.

Magnetic reconnection also heats up the plasma along the reconnected field lines, causing strong emission in the X-Ray lines to be observed by *Yohkoh*/SXT and *Hinode*/XRT. The reconnected field lines, which are released upwards due to reconnection, become part of the open field. The reconnected field lines that are released downwards are closed field lines, which form a bright (flare) arcade containing hot plasma, anchoring over the polarity inversion line between the emerging bipole and the ambient field. This results in a miniature X-Ray flare arcade, which is observed as the jet's bright point (Savcheva et al., 2007). As time evolves, the jet spire would move away from the jet's bright point. Both the spire and the bright point would fade away as the reconnection process stops. This most likely happens when the magnetic fields that build the current sheet are removed due to reconnection.

The above scenario for the formation of solar jets was used / suggested by Heyvaerts et al.

(1977) to explain solar flares in emerging flux regions. They described how field lines from an emerging flux system reconnect with the open ambient field, to emit hot and fast outflows (jets) from the reconnection region, and lead to flare heating at (and around) the reconnection site. Yokoyama and Shibata (1995, 1996) used the same idea as initial setup, to perform the first (2D and 2.5D) numerical experiments on the formation of X-ray jets and cool surges from the same emerging flux region.

Eruption-driven "Blowout" Jets

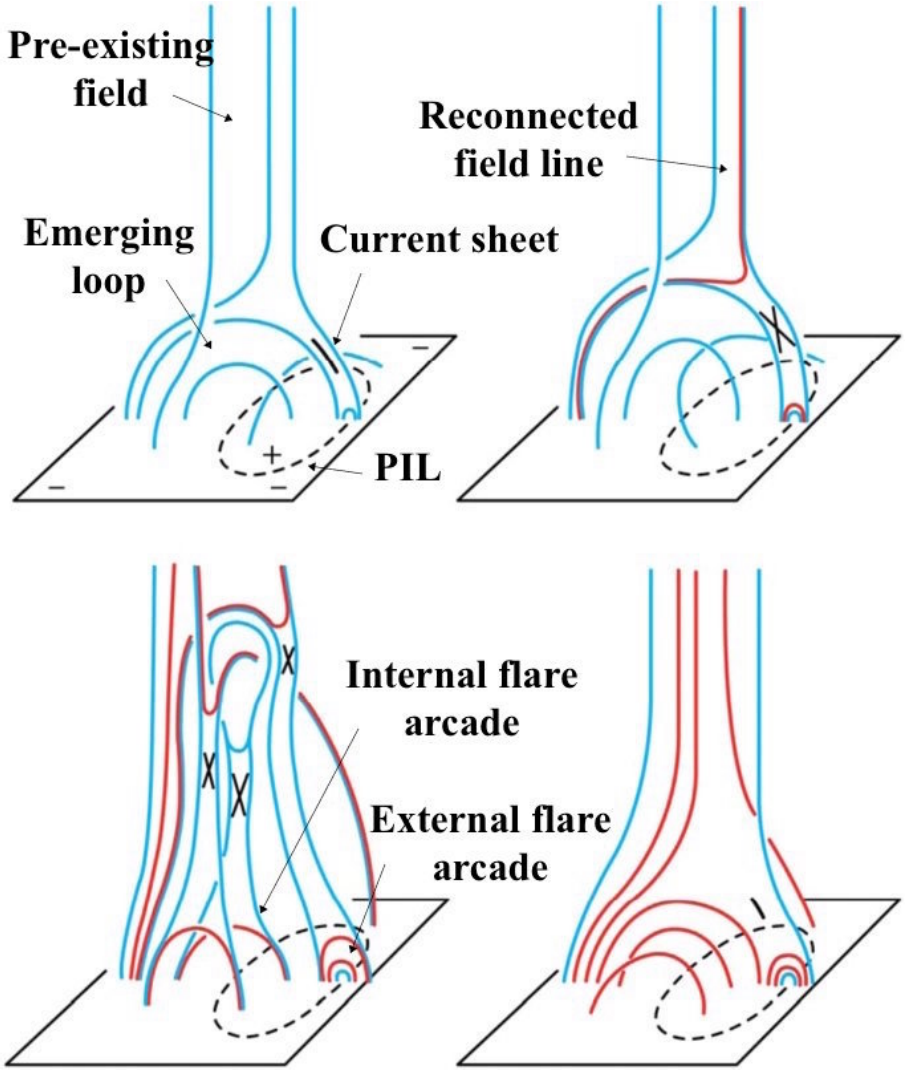

Figure 1.13: The schematic model of a "blowout" jet. From Moore et al. (2010). (Image credit: `http://iopscience.iop.org/article/10.1088/0004-637X/720/1/757/meta`)

The schematic model of a "blowout" jet is shown in Fig. 1.13 (Fig. 10 in Moore et al., 2010).

Initially a bipolar field emerges into a unipolar open ambient field. In contrary to the case of a standard jet, the core of the emerging bipole is extremely sheared and twisted. In the early stage of the "blowout" jet, a jet is emitted from the interface of the emerging loop and the ambient field due to magnetic reconnection at the current sheet, similar to the "standard" jet case. The reconnection process also produces the external X-Ray flare arcade, similar to the "standard" jet case.

Moore et al. (2010) suggested that the "blowout" eruptions are similar to CME eruptions but they occur on a much smaller scale. They suggested that there are two main mechanisms, which could be responsible for the onset of the eruptions. One possibility is that breakout reconnection (Antiochos et al., 1999) occurs first, at the current sheet between the emerging loop and the ambient field. The reconnection process removes the overlying field around the erupting core, releasing the downward tension above it, and, thus, helps it to erupt. The rise of the erupting core increases the pressure at the current sheet, which triggers more reconnection and assists the core to rise further. This mechanism leads to an ejective (full) eruption of magnetized plasma towards the outer solar atmosphere. In this case, the formation of the jet spire and the bright point can occur before the brightening of the base.

The other possibility is that the core erupts first, before the onset of the breakout reconnection at the current sheet. The core might have erupted due to MHD instability within the flux rope, or by tether-cutting reconnection at the field lines underneath the erupting core. When the core erupts, breakout reconnection occurs at the current sheet. In this case, the brightening of the base is observed before the formation of the jet spire and the appearance of the bright point.

The eruption-driven "blowout" jets transfer hot and cool material towards the outer solar atmosphere. The cool plasma is located within the erupting core of the field and it comes from the chromosphere / transition region layers. The hot material is the plasma, which is heated during reconnection above and underneath the erupting flux rope.

In this thesis, we study eruptions and eruption-driven ("blowout") jets, which emanate from quadrupolar emerging flux regions. In general, eruptions can be classified into two very broad types: ejective or confined (Moore et al., 1999). In the ejective eruptions, the magnetic field that erupts (e.g. a sheared magnetic arcade or a magnetic flux rope) has the energy to break-out or blow-out the ambient field and be ejected with high speed towards outer space. In the confined eruptions, the downward tension of the ambient field lines overwhelms the upward motion of the erupting plasma and, thus, it halts the eruption. The erupting core remains trapped within the envelope field. The total amount of energy, flux and twist of the erupting field are important factors, towards determining whether the eruption will be ejective or confined (Schrijver, 2009).

Chapter 2

MHD Equations

Magnetohydrodynamics (MHD), is the study of the behaviour of an electrically-conducting fluid in the presence of a magnetic field, which applies to the solar environment where hot ionised plasma flows in the magnetized solar atmosphere. The plasma flows here are considered to be continuous fluids.

Under Faraday's law of induction, the plasma flow with velocity, $\mathbf{v}$, interacts with the magnetic field, $\mathbf{B}$, which then produces an electromotive force (emf) of the order of $\mathbf{v} \times \mathbf{B}$. The induced current will then form an additional magnetic field which adds into the original magnetic field, resulting in the flow 'dragging' the magnetic field lines. The combined magnetic field then interacts with the induced current density, $\mathbf{j}$, which then produces a Lorentz force, $\mathbf{j} \times \mathbf{B}$. The produced Lorentz force is applied to the flow, hence resulting in the magnetic field 'pulling' the flow. The above process results in the well-known idea of 'flux freezing', where the magnetic field is 'frozen' into the flow.

2.1 Ideal MHD Equations

In the most simplified case, we consider a plasma which is sufficiently collisional. In this case, the macroscopic behaviour of the plasmas can be described by MHD. The plasma is defined with the following properties: mass density ρ, momentum density $\rho\mathbf{v}$, pressure p, electric field $\mathbf{E}$, magnetic field $\mathbf{B}$, which are all functions of both position and time. The heat flow among the plasma is negligible and both the ion and electron pressures would be isotropic if the collision is strong enough. Also, if the length scale L is large, the dimensionless magnetic Reynolds number $R_m = vL/\eta$ would be large as well, hence the resistivity, η, can be neglected.

In this case, the plasma can be described by a set of equations which is a combination of

the basic equations of electrodynamics and hydrodynamics, and is defined as the ideal MHD equations. The set of equations consists of the Maxwell's equations, conservation laws & the Euler's equation. In ideal ($\eta = 0$) MHD, the plasma is defined with the following properties: mean density ρ, mean velocity $\mathbf{v}$, mean pressure p & magnetic field $\mathbf{B}$.

Conservation of mass The conservation of mass implies that mass is a conserved quantity and hence the transport of mass can be shown by the continuity equation for density, with the following form,

$$\frac{\partial \rho}{\partial t} + \nabla \cdot (\rho \mathbf{v}) = 0. \tag{2.1}$$

Euler's equation Euler's equation, also named as the equation of motion, shows the changes of velocity in the system, has the following form:

$$\rho \left(\frac{\partial \mathbf{v}}{\partial t} + (\mathbf{v} \cdot \nabla)\mathbf{v} \right) = -\nabla p + \frac{\mathbf{j} \times \mathbf{B}}{\mu_0} + \rho \mathbf{g}. \tag{2.2}$$

where $-\nabla p$ is defined as the pressure gradient, $\mathbf{j}$ the current density, $\mathbf{j} \times \mathbf{B}$ the Lorentz force, μ_0 the permeability of free space and $\rho \mathbf{g}$ the gravitational force.

Energy equation Given the heat change in the plasma is small, the plasma is considered to be adiabatic and hence the adiabatic energy equation would be

$$\frac{\partial}{\partial t} \left(\frac{p}{\rho^\gamma} \right) + \mathbf{v} \cdot \nabla \left(\frac{p}{\rho^\gamma} \right) = 0, \tag{2.3}$$

where γ is the ratio of specific heats.

Maxwell's equations The evolution of the electric field $\mathbf{E}$ and magnetic field $\mathbf{B}$ is governed by Maxwell's equations, which are the following:

$$\nabla \times \mathbf{E} = -\frac{\partial \mathbf{B}}{\partial t} \tag{2.4}$$

$$\nabla \times \mathbf{B} = \mu_0 \mathbf{j} + \frac{1}{c^2} \frac{\partial \mathbf{E}}{\partial t} \tag{2.5}$$

$$\nabla \cdot \mathbf{B} = 0 \tag{2.6}$$

$$\nabla \cdot \mathbf{E} = \frac{\rho}{\epsilon_0}, \tag{2.7}$$

Eq 2.4 is the induction equation from Faraday's law of induction. Eq 2.5 is Ampère's law where c is the speed of light. Eq 2.6 is the solenoidal equation. Finally, Eq 2.7 is Poisson's equation,

which is not required in a non-relativistic theory where $\mathbf{v}$ is significantly small compared to the speed of light. ϵ_0 in Eq 2.7 represents the permittivity of free space. In the following, we retrieve Ampère's law and the magnetic induction equation.

Ampère's Law Considering Ohm's law, we have

$$\mathbf{j} = \sigma \left(\mathbf{E} + \mathbf{v} \times \mathbf{B} \right), \tag{2.8}$$

where σ is the electrical conductivity. From the equation above, we know that the electric field has a dimension of

$$E_0 = \frac{L_0}{T_0} \cdot B_0,$$

where L_0 the length scale, T_0 the time scale, and E_0 and B_0 are the dimensions of the electric and magnetic field respectively. Thus from Ampère's law (Eq 2.5), we have the second term on the right hand side (R.H.S.) to have a dimension of

$$\frac{1}{c^2} \cdot \frac{1}{T_0} \cdot \frac{L_0}{T_0} \cdot B_0 = \frac{L_0 B_0}{c^2 T_0^2}.$$

Comparing it with the dimension of the left hand side (L.H.S.), which has a dimension of B_0/L_0, we get

$$\begin{aligned} \frac{|\frac{1}{c}\frac{\partial E}{\partial t}|}{|\nabla \times \mathbf{B}|} &\sim \frac{L_0 B_0 / c^2 T_0^2}{B_0 / L_0} \\ &\sim \frac{L_0^2}{c^2 T_0^2} \\ &\sim \frac{V_0^2}{c^2}, \end{aligned}$$

where we define V_0 as the dimension of the plasma velocity. This then implies that if the plasma velocity is significantly smaller than the speed of light, the displacement current term, $\frac{1}{c^2}\frac{\partial \mathbf{E}}{\partial t}$, can be neglected. Hence Ampère's law becomes

$$\nabla \times \mathbf{B} = \mu_0 \mathbf{j}. \tag{2.9}$$

Induction equation We could again eliminate the electric field notation, $\mathbf{E}$ from Maxwell's equations by substituting Ohm's law, eq 2.8, into the Induction equation, eq 2.4, which we then

have

$$\frac{\partial \mathbf{B}}{\partial t} = \nabla \times (\mathbf{v} \times \mathbf{B}) - \frac{1}{\sigma} \nabla \times \mathbf{j}. \tag{2.10}$$

From the Ampere's law, eq 2.9, we have that

$$\mathbf{j} = \frac{1}{\mu_0} \nabla \times \mathbf{B}, \tag{2.11}$$

and substituting this into eq 2.10, and taking into account that $\eta = \dfrac{1}{\sigma \mu_0}$ we get

$$\begin{aligned} \frac{\partial \mathbf{B}}{\partial t} &= \nabla \times (\mathbf{v} \times \mathbf{B}) - \eta \nabla \times (\nabla \times \mathbf{B}) \\ &= \nabla \times (\mathbf{v} \times \mathbf{B}) - \eta \left(\nabla (\nabla \cdot \mathbf{B}) - \nabla^2 \mathbf{B} \right) \\ &= \nabla \times (\mathbf{v} \times \mathbf{B}) + \eta \nabla^2 \mathbf{B}. \end{aligned} \tag{2.12}$$

Thus, in ideal state where resistivity $\eta = 0$, the induction equation becomes

$$\frac{\partial \mathbf{B}}{\partial t} = \nabla \times (\mathbf{v} \times \mathbf{B}) \,. \tag{2.13}$$

Magnetic Reynolds number The induction equation is used to describe the temporal evolution of the magnetic field. The first term in the R.H.S. of eq 2.12 is considered as the magnetic advection term, and the second term the magnetic diffusion term. Magnetic advection describes how the plasma motions would affect the magnetic field, while the magnetic diffusion term describes how the magnetic field is smoothed out by the plasma flow. The ratio of these two terms is what we define as the Magnetic Reynolds number $R_m = v_0 L_0 / \eta$, as mentioned above. This dimensionless number can be used to determine which term would dominate in a given plasma field.

In the solar corona, the typical velocity and length scale are large such that the magnetic Reynolds number is very large ($R_m \sim 10^{14}$). Under this circumstance, the plasma flow is considered to be perfectly conducting, and that the magnetic field lines are 'frozen' into the plasma, where the magnetic field moves with the plasma flow. With a sufficiently large R_m, the magnetic diffusion term in the induction equation can be neglected.

However, considering a small region where the length scale L_0 is significantly small, R_m becomes significantly smaller than unity, $R_m \ll 1$. In this case, the magnetic diffusion term dominates the induction equation, and the magnetic advection term is neglected. This results in the magnetic field tends to relax towards a purely diffusive state, and magnetic energy is dissipated to other types of energy such as thermal energy.

Lorentz force The equation of motion, eq 2.2, is an equivalent form of Newton's law of motion $\mathbf{F} = m\mathbf{a}$, and the R.H.S. of eq 2.2 denotes the total external force applied onto the plasma. The second term in the R.H.S., $\mathbf{j} \times \mathbf{B}$, is called the Lorentz force. By substituting Ampère's law, eq 2.11, into the Lorentz force notation, we have that

$$\begin{aligned}\mathbf{j} \times \mathbf{B} &= \frac{1}{\mu_0} (\nabla \times \mathbf{B}) \times \mathbf{B} \\ &= \frac{(\mathbf{B} \cdot \nabla)\, \mathbf{B}}{\mu_0} - \nabla \left(\frac{B^2}{2\mu_0} \right).\end{aligned} \tag{2.14}$$

The first term in the R.H.S. is considered as the magnetic tension force term, and the second term the magnetic pressure force term.

Force-free equilibria In the static equilibria of the MHD equations (i.e. magnetohydrostatics, MHS), we assume that the plasma velocity is zero ($\mathbf{v} = 0$) and $\dfrac{\partial \rho}{\partial t} = 0$. Then, the momentum conservation equation becomes a force balance equation:

$$0 = -\nabla p + \mathbf{j} \times \mathbf{B} + \rho \mathbf{g}, \tag{2.15}$$

which is called the magnetohydrostatic equilibrium. Considering the ratio between the magnitude of the pressure gradient and of the gravitational force, we have

$$\begin{aligned}\frac{|-\nabla p|}{|\rho \mathbf{g}|} &= \frac{p_0 / L_0}{\rho_0 g} \\ &= \frac{\mathrm{H}}{L_0},\end{aligned} \tag{2.16}$$

where $\mathrm{H} = \dfrac{p_0}{\rho_0 g}$ is defined as the pressure scale height. This implies that if the length scale is sufficiently smaller than the pressure scale height, then gravitational forces can be neglected.

Considering the ratio between the magnitude of the pressure gradient and the Lorentz force, we have

$$\begin{aligned}\frac{|-\nabla p|}{|\mathbf{j} \times \mathbf{B}|} &= \frac{|-\nabla p|}{|(\nabla \times \mathbf{B}) \times \mathbf{B} / \mu_0|} \\ &= \frac{p_0 / L_0}{B_0^2 / \mu_0 L_0} \\ &= \frac{p_0}{B_0^2 / \mu_0}.\end{aligned} \tag{2.17}$$

The RHS of Eq 2.17 can be rewritten as $\dfrac{p_0}{B_0^2 / 2\mu_0}$, which is then the ratio of gas pressure to magnetic pressure, and is defined as the plasma beta β. If $\beta \gg 1$, then the gas pressure of

the plasma dominates and hence the plasma motion is determined by the plasma pressure force; however if $\beta \ll 1$, then the magnetic pressure dominates the plasma motion. Thus if β is small, we can neglect the pressure gradient. So if both the gravitational forces and the pressure gradient are neglected, we have $\mathbf{j} \times \mathbf{B} = 0$. This then implies that $\mathbf{B}$ is a force-free field. Such conditions are met in the solar corona, where the plasma velocity $\mathbf{v} \ll \mathbf{v_A} \approx 1000\,\mathrm{kms}^{-1}$, length scale $L_0 \ll \mathrm{H}$, and plasma beta $\beta \ll 1$.

Force-free field As mentioned above, the magnetic field $\mathbf{B}$ is considered to be force-free if

$$\mathbf{j} \times \mathbf{B} = 0,$$

which then implies that $\mathbf{j} \parallel \mathbf{B}$, and hence

$$\nabla \times \mathbf{B} = \alpha \mathbf{B}, \tag{2.18}$$

where α is a scalar function of position and is considered as a measurement of the twist of the magnetic field. And since $\mathbf{j} = \nabla \times \mathbf{B}$, we have that the magnitude of the current density is proportional to α.

Considering the case where $\alpha = 0$, we have that $\mathbf{j} = \nabla \times \mathbf{B} = 0$. This suggests that $\mathbf{B} = \nabla\phi$, with ϕ a scalar field, since the curl of the gradient of any scalar field is always 0. Since we have $\mathbf{B} = \nabla\phi$ and $\nabla \cdot \mathbf{B} = 0$,

$$\nabla \cdot (\nabla\phi) = \nabla^2\phi = 0,$$

which satisfies Laplace's equation. The magnetic field in this case is known as a potential field, which has the lowest possible energy state of the magnetic field.

If α is considered as a non-zero constant value everywhere in the field, the magnetic field is then considered as a linear force-free field (LFFF). A vector Helmholtz equation $\nabla^2\mathbf{B} + \alpha^2\mathbf{B} = 0$ is met by taking the curl of eq 2.18 and simplify it together with using the solenoidal constraint eq 2.6.

If α is considered not as a non-zero constant value but varies along field lines, then we obtain a nonlinear force-free field (NLFFF) with the following two conditions met:

$$\mathbf{B} \cdot \nabla\alpha = 0 \quad \text{and} \quad \nabla \times \mathbf{B} = \alpha\,(\mathbf{r})\,\mathbf{B} \tag{2.19}$$

2.2 Resistive, Compressible MHD Equations

In the ideal MHD case, the resistivity η is considered to be relatively small and hence treated as 0. However at smaller length scales, η is important and should be considered as well. While $\eta \neq 0$, we have the induction equation as in the form of eq 2.12,

$$\frac{\partial \mathbf{B}}{\partial t} = \nabla \times (\mathbf{v} \times \mathbf{B}) + \eta \nabla^2 \mathbf{B}.$$

The ideal MHD also treats the plasma to be incompressible, which is defined by $\nabla \cdot \mathbf{v} = 0$. This can be derived from the mass continuity equation, eq 2.1:

$$\begin{aligned} \frac{\partial \rho}{\partial t} + \nabla \cdot (\rho \mathbf{v}) &= 0 \\ \frac{\partial \rho}{\partial t} + \rho \nabla \cdot \mathbf{v} + (\mathbf{v} \cdot \nabla)\, \rho &= 0 \\ \frac{\partial \rho}{\partial t} + (\mathbf{v} \cdot \nabla)\, \rho &= 0 \\ \frac{\mathrm{D}\rho}{\mathrm{D}t} &= 0, \end{aligned} \tag{2.20}$$

where $\frac{\mathrm{D}}{\mathrm{D}t} = \frac{\partial}{\partial t} + \mathbf{v} \cdot \nabla$ is the material derivative.

Here we consider $\nabla \cdot \mathbf{v} \neq 0$. In the equation of motion in the ideal MHD, eq 2.2, viscous force is neglected in the external forces term, as no viscosity is considered. Considering the viscosity of the plasma to be ν, a viscous force is applied onto the plasma and is described as $\rho\nu\nabla^2\mathbf{v}$. Thus the equation of motion becomes

$$\rho \left(\frac{\partial \mathbf{v}}{\partial t} + \mathbf{v} \cdot \nabla \mathbf{v} \right) = -\nabla p + \mathbf{j} \times \mathbf{B} + \rho \mathbf{g} + \rho \nu \nabla^2 \mathbf{v}. \tag{2.21}$$

In the non-ideal case of MHD, the energy equation has also changed. From the adiabatic energy equation, eq 2.3, we have that

$$\frac{\mathrm{D}}{\mathrm{D}t} \left(\frac{p}{\rho^\gamma} \right) = 0,$$

where in this case it becomes

$$\frac{\rho^\gamma}{\gamma - 1} \frac{\mathrm{D}}{\mathrm{D}t} \left(\frac{p}{\rho^\gamma} \right) = \nabla \cdot (\kappa \nabla T) - \rho^2 Q\,(T) + \frac{j^2}{\sigma} + H, \tag{2.22}$$

where $\nabla \cdot (\kappa \nabla T)$ represents the thermal conduction term, $\rho^2 Q\,(T)$ represents the radiation losses, $\dfrac{j^2}{\sigma}$ is the Ohmic heating (or Joule heating), and H is just any other heating terms such as the

viscous heating. However, in this thesis, we do not consider both thermal conduction and radiation losses in the energy equation of our model.

2.3 Limitations of MHD

As mentioned in the beginning of this chapter, in order to apply MHD equations to the plasma, the plasma has to be hot and ionised. MHD starts to fail when the plasma is very weakly ionised. Also, an important condition for MHD to work is that the plasma velocity should be significantly smaller than the speed of light.

In addition, the collisions between the plasma have to be sufficient such that the pressures remains isotropic. This means that the collision time scale has to be significantly less than the time scale T_0, the mean free path to be much less than the length scale L_0, and also the gyroradius to be significantly smaller than the length scale L_0.

Chapter 3

Numerical Models

Over the past decades, numerical simulations have been carried out to simulate magnetic flux emergence from the convection zone of the Sun into the ambient solar atmosphere. In this chapter, we firstly report on the numerical simulations, which have been performed and published in the literature in the past (from 2D to 3D) and then we present the numerical setup of our numerical model(s).

3.1 2D & 2.5D Models

Shibata et al. (1989a) performed numerical experiments using a 2D ideal MHD model, which studies the non-linear evolution of the undular mode of the magnetic buoyancy instability (Parker instability) in a magnetic flux sheet. In their model, they mimic a simplified solar atmosphere, which consists of the solar corona and a chromosphere/photosphere layer. Initially (at $t = 0$) a horizontal magnetic flux sheet with $\beta \simeq 1$ is placed at the bottom of the photosphere and satisfies magnetostatic balance under a constant gravitational acceleration. A small velocity perturbation is introduced to the system at the middle of the magnetic flux sheet initially to drive the instability, and has the form

$$v_x \propto \sin\left[\frac{2\pi\left(x - x_{max}/2\right)}{\lambda}\right].$$

v_x is the horizontal velocity, λ the horizontal wavelength of the perturbation, and x_{max} is the horizontal size of the numerical domain.

A few cases were considered in their work. They found that when $\lambda = x_{max}$, the magnetic loop undergoes a bubble-like expansion and initially the instability grows linearly. As instability grows, the loop rises upwards into the corona. However when the loop enters the corona, the

rising motion is seen to decelerate while comparing to the acceleration in the chromosphere. This is because the loop is unstable to the undulating perturbation in the chromosphere and the magnetic buoyancy force is greater than the restoring magnetic curvature force. However, due to the corona being stable against the horizontal perturbation in this given wavelength, the restoring magnetic curvature force is greater than the magnetic buoyancy force thus the deceleration. Downflows exceeding the local sound speed are seen along the loop, which then produces shock waves near the footpoints of the loop. In the case where $\lambda \ll x_{max}$, they found that the expansion of the magnetic loop shows self-similar evolution with height. It is also found that the acceleration of the rising motion of the loop decreased in the corona, similar to the previous case. However the decrease rate is smaller than the previous case due to smaller magnetic curvature force in the corona. This is because of the larger effective wavelength and that the perturbation is more pronounced. They have also found that the larger the coronal base height, the higher the maximum rise velocity of the loop.

In Shibata et al. (1989b), the effect of the inclusion of an overlying magnetic field in the corona is being studied. A very similar numerical setup as Shibata et al. (1989a) is being considered. The only difference was that they solved the resistive MHD equations rather than the ideal MHD equations. They found that the expansion rate of the magnetic loop is significantly slower when the overlying field is parallel to the emerging field. However when the overlying field is anti-parallel to the emerging field, the expansion is not decelerated due to magnetic reconnection between the overlying field and the emerging field. A jet-type flow, which was produced by the gas pressure gradient was found to be emitted along the reconnected field line.

Shibata et al. (1992b) performed 2D numerical simulations with a numerical model similar to that of Shibata et al. (1989b). In this paper, they also included a convection zone in the numerical domain, and an anomalous resistivity rather than uniform resistivity. Initially a horizontal magnetic flux sheet (unstable to the undular mode of the magnetic buoyancy instability) was placed in the convection zone, and the corona was filled with an anti-parallel magnetic field. They showed that magnetic reconnection at the current sheet between the emerging field and the overlying coronal field starts when the chromospheric plasma in the current sheet has drained down. They suggested that the formation of the X-ray bright point (due to reconnection) happens after the disappearance of the arch filament (chromospheric plasma).

Apart from the emergence of a magnetic flux sheet, theoretical studies considered the emergence of a magnetic flux tube. It was found that a non-twisted magnetic flux tube would fail to emerge into the solar surface. For instance, Schuessler (1979) showed that a non-twisted buoyant magnetic flux tube would experience distortion and it will fragment as it rises through the convection zone. More precisely, it will fragment into two smaller magnetic field segments with equal but opposite vorticity.

Longcope et al. (1996) have carried out a detailed study about the emergence of a non-twisted flux tube by solving 2D MHD equations numerically. They report that an isolated horizontal flux tube can only rise a few radii of its own before fragmenting into smaller flux tubes. The further rise is held back because the initial upward velocity is transformed into horizontal velocity in the fragments. They also suggested that if the flux tube contained sufficient twist, the flux tube might have risen coherently. This is in agreement with the work by Parker (1979) who reported that twist of the magnetic field can provide integrity to the tube.

Moreno-Insertis and Emonet (1996) showed the first results of the 2D numerical simulation of the emergence of twisted buoyant magnetic flux tube in the convection zone. They showed that the transverse component of the field can suppress the fragmentation of the flux tube into two vortex filaments under certain conditions. The magnetic stress of the transverse field becomes important when Ψ (i.e. the pitch angle of the field lines around the tube) satisfies

$$\tan\Psi = \left(\frac{R}{H_p}\right)^{1/2}, \tag{3.1}$$

where R is the radius of the tube and H_p the pressure scale height.

Emonet and Moreno-Insertis (1998) confirmed the result that sufficient twist of the magnetic field lines around the tube axis can suppress the fragmentation of the flux tube during the rise of the flux tube through convection zone. They showed that given a flux tube with a relative density deficit on the order of $\delta\rho/\rho \sim \mathcal{O}(1/\beta)$ and a radius significantly smaller than the pressure scale height, $R^2 \ll H_p^2$, an average pitch angle of the order $\Psi \sim \sin^{-1}\left[(R/H_p)^{1/2}\right]$ is required such that the flux tube remains coherent. They reported that most of the flux tube is still fragmented in the case where the flux tube is weakly twisted, whereas when the flux tube is highly twisted, the flux tube rises while maintaining its own shape and with no substantial loss of magnetic flux.

Krall et al. (1998) reported on numerical simulations, solving a set of 2.5D compressible MHD equations. They modelled the flux-rope emergence from the chromosphere to corona, and found that a weak, vertically oriented overlying magnetic field with $(B_{overlying}/B_{tube})^2 \ll 1$, can prevent a non-twisted flux tube from being fragmented and also direct the upward buoyancy-driven flow such that the flux tube penetrates the chromosphere-corona boundary. The upward buoyant motion is seen to stop at the chromosphere-corona boundary due to the significant drop in pressure gradient, and the flux tube breaks up rapidly.

Magara (2001) reported on numerical simulations of a 2.5D MHD model with a twisted magnetic flux tube placed in the upper convection zone initially. The Gold-Hoyle flux tube model was used to provide the initial magnetic field distribution. Initially the pressure between the flux tube

and the surrounding area were in balance so that:

$$p_{tg} + p_{tmag} = p_{ext}, \tag{3.2}$$

where p_{tg} is the gas pressure within the flux tube, p_{tmag} is the magnetic pressure within the flux tube and p_{ext} is the surrounding gas pressure. The requirement for thermal equilibrium together with the ideal gas law ($p = \rho RT$, p - gas pressure, ρ - density, R - gas constant, T - temperature), leads to the condition that $\rho_{tg} < \rho_{ext}$ (i.e. the density within the flux tube ρ_t is smaller than the surrounding density ρ_{ext}). In turn, this leads to the buoyancy effect and thus the magnetic flux tube rises through the convection zone. Moreover, since the convection zone is a (convectively) unstable layer, continuous convection motion arises, which assists the rising of the flux tube.

Since the photosphere is a (convectively) stable layer that inhibits buoyancy, the flux tube cannot persist through the photosphere, and hence the emerging field slows down when it reaches the solar surface. The flux tube starts to spread out horizontally due to the different velocity at the top and bottom of the flux tube. A flattened magnetic layer is then formed underneath the photosphere and as the flattening process continues, the density of the magnetic layer drops as the plasma is being pushed to the edges of the layer by the horizontal surface motions. When the density of the magnetic layer is lower and more strongly magnetized than the overlying layer, the magnetic Rayleigh-Taylor instability criterion is met and thus causing the flux tube to emerge into the photosphere.

3.2 3D Models

3.2.1 Bipolar Region Formation

Although the 2D or 2.5D simulations are easier to study, a more realistic approach would be to perform the simulations in a 3D domain. Matsumoto and Shibata (1992) and Matsumoto et al. (1993) were among the first to perform 3D MHD simulations. In their simulation, the numerical domain is a very simplified model of the solar atmosphere and consists of only the chromosphere/photosphere layer and the solar corona, which both layers are isothermal gas layers. Cases of the evolution of magnetic flux sheets and magnetic flux tubes are shown. The original magnetic fields are placed at the bottom of the photosphere/chromosphere layer initially. Both, the magnetic flux sheet and flux tube, are unstable to the magnetic buoyancy instability and thus they rise. The 3D simulations confirmed the main results found in the 2D simulation studied by Shibata et al. (1989a).

In Matsumoto et al. (1998) and Magara and Longcope (2001, 2003), a numerical layer representing the convection zone in a 3D numerical domain is included, and a twisted magnetic flux

tube is placed in the convection zone initially. Similarly the system is set to evolve by introducing a small vertical velocity perturbation at the middle of the flux tube, and is switched off after several timesteps. In Matsumoto et al. (1998), both short and long wavelength perturbations are studied. It is reported that for the short wavelength perturbation case, the flux tube undergoes kink instability forming helical structures, and it rises through the convection zone due to convective instability. When the flux tube rises into the photosphere, magnetic buoyancy instability takes place and the magnetic loop formed continues to rise into the corona. When the flux tube emerges into the photosphere, a sigmoidal structure is seen to be formed.

Magara and Longcope (2001) developed the 2.5D study of Magara (2001) into a 3D study while using the same temperature and magnetic field distribution. Magara and Longcope (2003) has a similar setup as Magara and Longcope (2001) except for the initial velocity perturbation and also the profile for the magnetic flux. They did a more detailed study by reporting also on the magnetic energy, helicity and the field line topology. They found that the injection of the magnetic energy and helicity through flux emergence into the solar atmosphere is carried out by two different motions, the shearing motions and the emerging motions. They also found that the emerging motions are dominant during the early stage of emergence, when the photospheric area of magnetic polarity regions expands. Then as the emergence saturates, the polarity region deforms and fragments through shearing motions, which dominate the emergence.

Instead of driving the flux tube to rise by injecting a small vertical velocity perturbation at the beginning, Fan (2001) has reported on the emergence of a Ω-shape magnetic flux tube with a constant twist, which would result in the formation of a single bipolar region while emerging into the photosphere. The Ω-shape magnetic flux tube which lies along the x-axis at $y = 0$, is obtained by implying a density deficit along the magnetic flux tube,

$$\rho(x, y, z) = \frac{p(x, y, z)}{p_0(z)} \rho_0(z) \exp(-x^2/\lambda^2), \tag{3.3}$$

where p_0 & ρ_0 denotes the pressure and density of the unperturbed plasma respectively, and λ is the length of the buoyant part of the flux tube. Given this density distribution, the middle part of the flux tube would be more buoyant than the rest of the tube due to smaller density, and thus rises through the convection zone under buoyancy effect. The upper part of the tube then expands into the solar atmosphere under a combination of both Rayleigh-Taylor instability and magnetic buoyancy instability. The solar atmosphere is modelled by including the solar interior (convection zone), the photosphere/chromosphere layer, the transition region, and the corona. The azimuthal component dominates as the flux tube expands, and thus when the flux tube first emerges, the outermost field lines are almost perpendicular to the axis of the flux tube. This is also reported in many other simulations of Ω-shape flux tube emergence (e.g. Magara and Longcope, 2003; Archontis et al., 2004; Manchester et al., 2004, etc.).

Archontis et al. (2004) gives a detailed description on the emergence of an Ω-shape magnetic flux tube, similar to Fan (2001), but by solving the resistive MHD equations. They studied the emergence of the flux tube in detail in order to understand the physical processes of the emergence. When the flux tube reaches the photosphere, the Parker instability causes the field to emerge into the photosphere, as reported in previous simulations. They then showed that the precise criterion for the onset of the instability (Acheson, 1979) is that

$$-H_p \frac{\partial}{\partial z} (\log B) > -\frac{\gamma}{2}\beta\delta + \tilde{k}_{\parallel}^2 \left(1 + \frac{\tilde{k}_{\perp}^2}{\tilde{k}_z^2}\right), \tag{3.4}$$

where H_p the pressure scale height, γ the specific heat ratio, β the plasma beta. $\tilde{k}_{\parallel}$ is the horizontal component of the wave vector which is parallel to the field, $\tilde{k}_{\perp}$ perpendicular to the field, and $\tilde{k}_z$ the vertical component of the wave vector. δ is the superadiabatic excess with $\delta = \nabla - \nabla_{ad}$, where ∇ is the logarithmic temperature gradient in the equilibrium stratification and ∇_{ad} is its adiabatic value. In the photosphere, an isothermal layer, $\delta = -0.4$ causes strong stabilization. However β decreases when the flux tube reaches the photosphere due to the increase of magnetic pressure, the term $\beta\delta$ becomes small as well. This causes the onset of the Parker instability.

They also studied the emergence of the twisted magnetic flux tube into a pre-existing horizontal coronal field, and they reported evidence of magnetic reconnection between them. This interaction has also been studied in detail in other simulations (Archontis et al., 2005; Galsgaard et al., 2005; Archontis et al., 2006; Galsgaard et al., 2007), and it is reported that the reconnection between the anti-parallel magnetic fields give rise to hot and fast outflows. However, it is also reported that if the two system of magnetic fields are more parallel to each other, magnetic reconnection is less efficient and the amount of reconnected flux is limited, hence no such outflows are seen. Archontis and Hood (2012) investigated the conditions of eruptions in various orientations of the coronal ambient field.

Manchester et al. (2004) used the same initial setup as in the work by Fan (2001), but they reduced the buoyant part of the tube λ by a half. They reported that the emergence of a twisted flux tube drives shear flows along the polarity inversion line that eventually leads to the formation of a flux rope. The flux rope is then seen to be ejected. This is also reported in many other flux emergence simulations (e.g. Archontis and Török, 2008; Archontis and Hood, 2010; Leake et al., 2013, etc.). They also found that the twist is transferred to the coronal field through the upward propagation of shear Alfvén waves.

Archontis and Török (2008) reported that the emergence of a magnetic flux tube into a unmagnetized corona would lead to the formation of a coronal flux rope due to the induced shearing motion and magnetic reconnection at low atmospheric heights. However, the expanding envelope field suppresses the flux rope from erupting, resulting in a confined eruption. They furthermore

showed that the presence of the pre-existing coronal field would then allow the expanding envelope field to reconnect with it, and thus allowing the flux rope to be fully erupted. This is shown to be similar to the observed filament eruptions and CMEs. They also suggested that the formation of a flux rope in the emerging field region is a generic phenomenon, regardless of the amount of twist and the length of the buoyant part (λ) in the tube.

Moreno-Insertis et al. (2008) showed that the emergence of a twisted flux tube into an oblique coronal ambient field triggers reconnection between the two field systems and ejects a jet along the coronal field lines. This study was extended by Moreno-Insertis and Galsgaard (2013) where the flux emergence simulation is carried out in a larger numerical domain for a longer computational time. They reported on the onset of homologous eruptive events from the emerging flux region after the initial emission of the reconnection jet.

Archontis and Hood (2012) found that the stronger the twist in the coronal flux rope, the more dense plasma is being carried into the corona following the eruption. They also showed that if the pre-existing coronal field is too strong compared to the erupting field, the flux rope would collide with the non-reconnected ambient field and undergoes deformation, resulting in no eruption being emitted. In the case where the pre-existing coronal field is anti-parallel to the erupting field, the flux rope erupts into the outer solar atmosphere in an ejective manner, whereas when the pre-existing coronal field is parallel to the erupting field, reconnection is not sufficient and the overlying envelope flux traps the erupting flux rope and halts the eruption (i.e. confined eruption).

Archontis and Hood (2013) reported on 3D MHD simulations of jets in emerging flux regions. It was found that following the emergence and during the eruption, recurrent jets are formed and emitted along the reconnected coronal field lines. They showed that the interaction between the emerging field and the ambient field (i.e. external reconnection) leads to the emission of the standard reconnection jets (Heyvaerts et al., 1977; Shibata et al., 1992a). Following the shearing motion along the polarity inversion line (PIL) in the emerging flux region (EFR), a flux rope is being formed and starts to erupt. The erupting flux rope then blows out the ambient field and is ejected to the outer solar atmosphere. The twisted field lines underneath the erupting core undergoes reconnection internally (internal reconnection) when the core erupts, and emits a reconnection jet as well. The emission of the cool erupting plasma from the erupting core together with the hot reconnection jets due to both the external and internal reconnection, form a wide "blowout" jet (Moore et al., 2010). The "blowout" jet is seen to undergo an untwisting motion as it is ejected towards the outer solar atmosphere.

Fang et al. (2014) included heat conduction in the emergence of a twisted magnetic flux tube into a pre-existing coronal field. They reported on the emission of coronal jets following the emergence of the flux tube, and that both hot and cool plasma are being ejected along the unwinding

field lines during the eruption. This produced the observed transverse motion of the ejected jet spires. They also found that no rotation motion occurs in the downward companion jet, which matches the observations (Liu et al., 2009). They reported that the inclusion of thermal conduction allows more mass being ejected into the corona together with the "blowout" jets. The ejected mass is reported to fall back to the lower atmosphere in the case without thermal conduction due to the lack of support. They have also found that during the emission of "blowout" jets, a 2% increase of mass in the corona occurs, which suggests that the "blowout" jets might act as a source of the heated mass of the solar wind.

3.2.2 Quadrupolar Region Formation

In the previous section, we briefly discussed the studies where a magnetic flux structure (e.g. a flux tube) emerges into the photosphere to form a single bipolar region. The results of such simulations have been commonly used to compare with observations of the formation of a single bipolar sunspot group (β sunspots). Other observations have reported that many sunspots originate in quadrupolar regions adopting a more complex (δ-type) configuration (e.g. Morita and McIntosh, 2005; Komm et al., 2008; Schrijver et al., 2011; Sun et al., 2012; Toriumi et al., 2014, etc.). It has been found that these sunspots have shorter lifespan but they are more active and lead to the onset of considerable flaring activity (e.g. M, X class flares). Sammis et al. (2000) concluded that 82% of X class flares, and all of the X4 and stronger flares occur in δ-spots after studying an 8 year period of active region observations. Therefore, the study of quadrupolar regions (their emergence and evolution) is very important towards understanding the manifestation of solar magnetic activity. However, a very small number of relevant (numerical) studies are found in the literature.

Toriumi et al. (2014) has reported on the formation of a quadrupolar region in a 3D MHD model. Their aim was to reproduce NOAA AR 11158 reported by Schrijver et al. (2011) and Sun et al. (2012). They carried out two cases to test if the quadrupolar region is formed by the emergence of a single magnetic flux tube with a double Ω-shape configuration or the emergence of two single Ω-shape flux tubes which are parallel to each other. They reported that the first case would reproduce exactly what is observed: a single quadrupolar region, with clearly a long, sheared PIL in between the inner polarities and the adjacent elongated polarities. In the second case, the inner polarities of the quadrupolar region just slip through each other and did not form a clear PIL.

Fang and Fan (2015) reported on the emergence of a magnetic flux tube with a double Ω-shape setup into a non-magnetized corona. They showed that the expansion and rotation of the emerging fields drive the inner polarities to come together and form a compact δ-sunspot with a sharp PIL. Along the PIL, they found strong transverse field with highly sheared magnetic and velocity field and strong currents. However, they reported that there was no formation of a coherent helical

coronal flux rope in the emerging flux region, which might be due to numerical diffusion because of the large cell size in the corona ($1237.4\,\mathrm{km}$).

Takasao et al. (2015) performed numerical simulations on the formation of a quadrupolar region, but with a different approach. They report on the emergence of an initially kink-unstable flux tube from the solar interior to the corona. The flux tube rises through the convection zone and emerges into the photosphere, forming a single bipolar region. As the magnetic field expands, due to the continuous emergence of flux at each pole and the relatively weaker twist between the poles, plasma condenses at the region between the poles. Due to downward gravitational force, the heavy plasma accumulated in the center region is then being dragged down, causing a submergence in the magnetic field. The submerged magnetic field then intersects with the photosphere which then leads to the apparent formation of a new bipolar structure. Therefore, a new bipolar field is formed in between the original bipolar region, thus forming a quadrupolar region.

3.3 Our Model Setup

In this thesis, we use a numerical model similar to Fan (2001) and Archontis et al. (2004) with one difference. In the solar interior, we do not impose a single Ω-shape magnetic flux tube but a double Ω-shape flux tube, which forms a quadrupolar region when it intersects the photosphere. This configuration for the magnetic field is similar to that of Toriumi et al. (2014). The main reason that we used this magnetic field distribution is to examine how the solar magnetic activity occurs (e.g. the onset of eruptions and jets) in a quadrupolar region.

To perform our simulations, we solved (numerically) the 3D time-dependent, resistive and compressible MHD equations in a Cartesian geometry, by using the Lare3D code (Arber et al., 2001). Viscous and Ohmic heatings are considered through shock viscosity and Joule dissipation. We use explicit resistivity, which is treated either as uniform or a non-uniform variable. In the latter case, the resistivity depends on the value of the local current. If the current exceeds a threshold, we focus dissipation at interfaces with steep gradients of the magnetic field.

3.3.1 Lare3D Code

Lare3D code is a Lagrangian remap codes, which can be used to solve the full set of the 3D MHD equations. The code uses a staggered grid and has a second order accuracy in both spatial and temporal resolution. In every timestep, the calculation is split into two parts, namely the 3D Lagrangian step and the remap step. The time update in every time step is split into the Lagrangian step first, and then remapped onto a new grid before stepping into the next time step.

The variables are staggered on the computational grid (staggered grid). All scalar variables (e.g. ρ, pressure, energy) are calculated in the middle of the 3D computational cell. The magnetic field components (B_x, B_y, B_z) are calculated in the middle of each cell faces such that the solenoidal constraint $\nabla \cdot B = 0$ can be maintained to machine precision by the Evans and Hawley (1988) constrained transport. The velocity components (v_x, v_y, v_z) are calculated at the cell vertex, and all three components are calculated at the same vertex.

The Lagrangian step is fully 3D and has a second order predictor-corrector scheme. Artificial viscosity is applied in the Lagrangian step and has the form taken from Wilkins (1980) in order to capture the shocks accurately. The remap step uses van Leer (1979) gradient limiters in order to preserve monotonicity. The remap step uses a third order estimate despite the fact that the Lagrangian step is only second order accurate. The third order estimate is used as the computational cost can be neglected while doing no harm to the calculation.

3.3.2 Initial Background Stratification

The initial background stratification in our model consists of the following layers: upper solar interior, photosphere, chromosphere, transition region and solar corona. Hydrostatic equilibrium is assumed everywhere in the numerical domain.

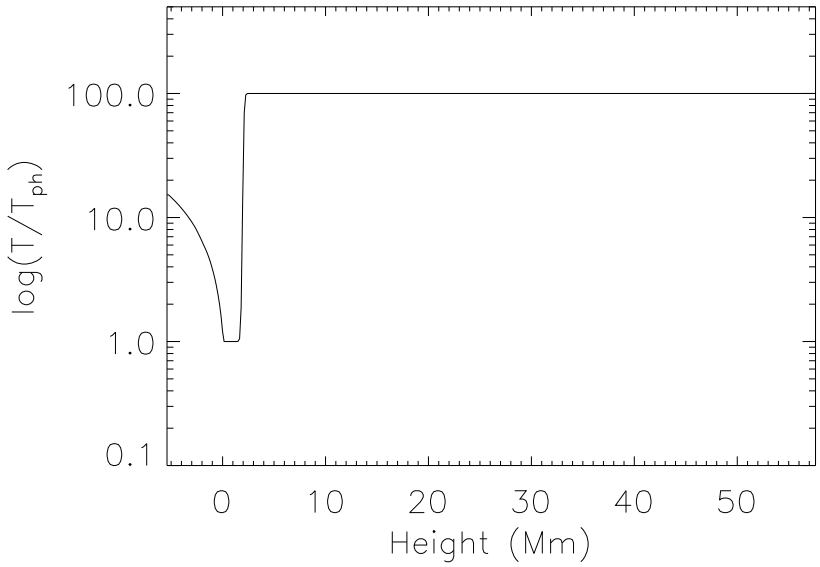

Figure 3.1: The initial temperature distribution which is normalised by the initial photospheric temperature, taken along $(0, 0, z)$.

The upper solar interior layer, which is the convection zone, is reproduced by an adiabatic layer

and lies at $-5.4\,\mathrm{Mm} \leq z \leq 0\,\mathrm{Mm}$. The temperature in the convection zone has the following distribution,

$$T(z) = T_{ph} - \frac{(\gamma - 1)}{\gamma} g, \tag{3.5}$$

where T_{ph} is the photospheric temperature, $\gamma = \frac{5}{3}$ is the ratio of heat capacity, and g the gravity distribution.

Above the convection zone is a layer which is combined by the photosphere & chromosphere, which lies at $0\,\mathrm{Mm} \leq z \leq 1.9\,\mathrm{Mm}$. The photosphere is an isothermal layer and has a temperature of $T_{ph} = 5100\,\mathrm{K}$. The temperature gradually increases in the chromosphere and reaches up to $\sim 3 \times 10^4\,\mathrm{K}$ at the top of the chromosphere.

In between the chromosphere and the corona lies a very thin layer with a steep temperature gradient, the transition region. The transition region lies at $1.9\,\mathrm{Mm} \leq z \leq 2.7\,\mathrm{Mm}$ and the temperature increases by up to 2 order of magnitude within the layer.

The corona, which is an isothermal layer, is placed on top of the transition region up to the upper boundary of the numerical domain. The temperature in the corona is set to be $T_{cor} = 100\,T_{ph}$, and the corona lies at $2.7\,\mathrm{Mm} \leq z \leq 57.6\,\mathrm{Mm}$.

The initial temperature distribution in the solar atmosphere is modelled by a simple distribution function as following,

$$T(z) = T_{ph} + \frac{1}{2}(T_{cor} - T_{ph}) \left[\tanh\left(\frac{z - z_{tr}}{w_{tr}} \right) + 1 \right], \tag{3.6}$$

where z_{tr} is the height of the middle of the transition region and w_{tr} is a variable indicating the thickness of the transition region. w_{tr} is chosen such that $T(0\,\mathrm{Mm} \leq z \leq 1.5\,\mathrm{Mm}) = T_{ph}$ & $T(2.7\,\mathrm{Mm} \leq z \leq 57.6\,\mathrm{Mm}) = T_{cor}$.

Numerical Domain

The numerical grid is set to be a uniformly spaced $420 \times 420 \times 420$ box, which corresponds to a numerical domain of $(x, y, z) = ([-31.5, 31.5]\,,\, [-31.5, 31.5]\,,\, [-5.4, 57.6])\,\mathrm{Mm}$. The horizontal boundaries (both x & y) are set to have periodic boundary conditions. The lower boundary of the box is set to be a non-penetrating conducting wall and the top boundary is set to be open, which allows plasma to flow out of the numerical domain.

Open boundary The open boundary is obtained via far-field Riemann characteristics, where a fixed far-field with fixed properties (e.g. ρ, T etc.) is required. The code then calculates the propagating wave velocity at the boundary and projects the 1D Riemann invariants into the ghost cells. The values are carried into the ghost cells provided the wave is an outward propagating wave, or if the wave is an inward propagating wave, the values from the far-field are carried in.

3.3.3 Magnetic Field Configuration

The flux tube is placed at height $z_0 = -2.1\,\mathrm{Mm}$, which is $2.1\,\mathrm{Mm}$ beneath the photosphere initially. The flux tube is oriented in parallel to the horizontal (y) axis. The magnetic field of the flux tube is defined by

$$\begin{aligned} B_y &= B_0 \exp\left(-r^2/R^2\right), \\ B_\theta &= \alpha r B_y, \end{aligned} \tag{3.7}$$

where R represents the radius of the flux tube, and r is the radial distance away from the axis of the tube, which has the form

$$r^2 = x^2 + (z - z_0)^2 . \tag{3.8}$$

α is set to be the twist of the magnetic flux tube. In order to maintain the flux tube's coherence while the flux tube rises through the convection zone, the magnetic flux tube must have a minimum twist (Moreno-Insertis and Emonet, 1996). The twist is set to be uniform across the flux tube, and is set to have a value such that the magnetic flux tube is marginally stable to the kink instability.

The density deficit applied to the flux tube initially has the form of

$$\Delta\rho = \frac{p_t(r)}{p(z)}\rho(z)\exp(-y^2/\lambda^2)\sin^2(2\pi y/\omega), \tag{3.9}$$

where $\Delta\rho$ is the density deficit, p_t the pressure inside the flux tube, λ is half of the length of each buoyant part of the flux tube, and ω is set to be half of the length of the flux tube. The density deficit along the flux tube is then plotted as in Figure 3.2.

In the Sun, the solar atmosphere is magnetized. Therefore, to make our model more realistic, we add an ambient magnetic field in the background atmosphere (see Figure 3.3). This field is (mathematically) defined by the following equation

$$B_c = B_c(z)(0, \cos\theta, \sin\theta), \tag{3.10}$$

where θ is the angle between the ambient field lines and the y-axis. We choose an angle of 80

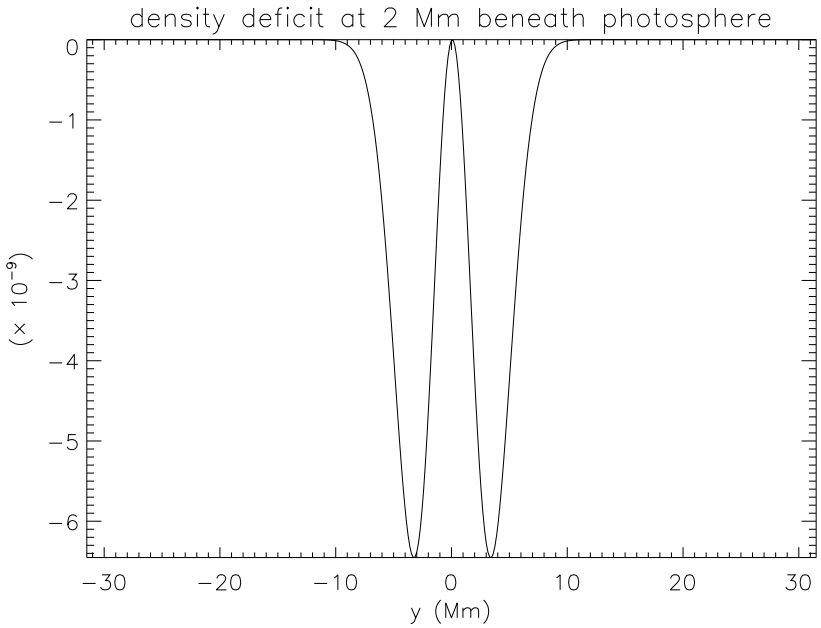

Figure 3.2: The density deficit distribution along the flux tube.

degrees (as measured from the negative y-axis), so that the ambient field is oblique, mimicking e.g. the magnetic field environment in a coronal hole. The ambient field extends from the corona into the convection zone. The field strength B_c is set to be constant in the corona. Then it starts to decrease (gradually), from the transition region and downwards, until it reaches very small values (practically 0 in the convection zone, so that it does not affect the emergence of the sub-photospheric field).

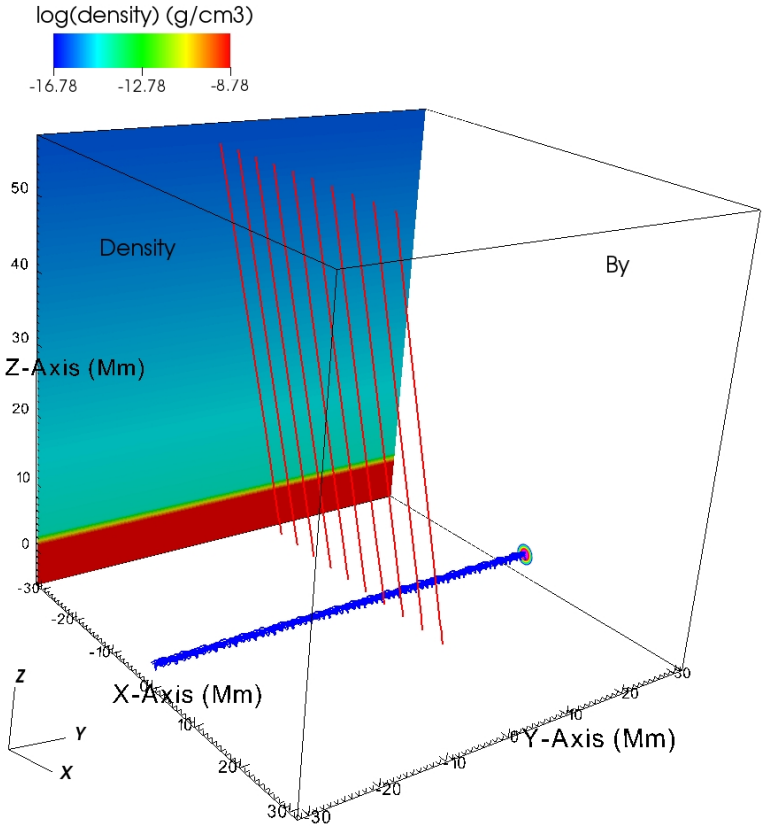

Figure 3.3: The red field lines show some selected magnetic field lines of the pre-existing magnetic field, and the blue field lines show the twisted magnetic flux tube, which lies at the convection zone. The coloured y-z plane shows the initial density distribution of the background atmosphere, and the x-z plane shows the isocontours of B_y.

Chapter 4

Emergence Into an Unmagnetized Corona: The Onset of Confined Eruptions

Numerical simulations of the formation of a single bipolar emerging flux region through magnetic flux emergence have been well studied over the past 30 years, as mentioned in the previous chapter (Chapter 3). However, not many numerical experiments consisting of a quadrupolar region setup have been reported. It is observed that quadrupolar regions are common phenomena on the Sun, and quadrupolar regions would normally consist of a δ-sunspot group within the EFR. δ-sunspots, which are short living sunspots, are known to be very active and produce most of the major solar flares. Hence it is very important to study the formation and evolution of a quadrupolar region in a simulated EFR.

In this chapter, we use the model introduced in Section 3.3. Initially a twisted magnetic flux tube is placed at $2.1\,\mathrm{Mm}$ beneath the photosphere. The magnetic field configuration of the flux tube is defined as in Eq 3.7. The flux tube strength is set to be $B_0 = 2.4 \times 10^3\,\mathrm{G}$, and the radius is $R = 450\,\mathrm{km}$. The flux tube has a twist of $\alpha = 0.4$ such that it is marginally stable to kink instability. The density deficit has the form of Eq 3.9, with $\lambda = 3.6\,\mathrm{Mm}$ and $\omega = 31.5\,\mathrm{Mm}$. This causes the density at $y = \pm 3.3\,\mathrm{Mm}$ to be lower than the surrounding area (Fig 3.2). Here, we consider the corona to be non-magnetized and the resistivity to be uniform everywhere in the numerical domain ($\eta = 0.01$).

In the Sun, the magnetic diffusivity η is very small (and the magnetic Reynolds number is huge). Thus, gradients of the magnetic field must become very large before dissipation of the energy begins. In our numerical experiment, we use an explicit resistivity, which is many orders of magnitude larger than on the Sun, and dissipation starts at much smaller magnetic field gra-

dients. However, the total amount of energy that is dissipated in our numerical domain (e.g. in the chromosphere-corona region) and the amount of flux, which is transferred into the solar atmosphere, are not unrealistic (see Chapter 6). In fact, they lie within a typical range of values, which is commonly provided by observations of eruptive jets.

Also, the value of $\eta = 0.01$ is the typical value of explicit resistivity that we can use, so that the energy of the system does not diffuse because of the numerical resistivity. The explicit resistivity together with the high numerical resolution used in the experiment, guarantee that energy dissipation is controlled explicitly (i.e. by the user) and not numerically (i.e. by the code).

4.1 Emergence: Initial Stage and Dynamic Evolution

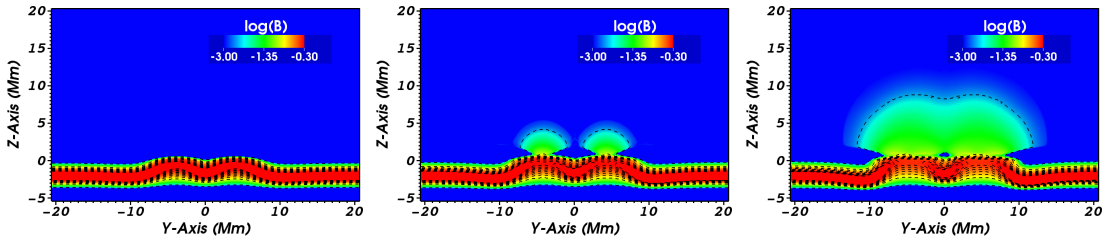

(a) $t = 142.83\,\mathrm{min}$. (b) $t = 178.54\,\mathrm{min}$. (c) $t = 214.25\,\mathrm{min}$.

Figure 4.1: Magnetic field strength distribution along the magnetic flux tube at various times, taken at $x = 0$. The overplotted dashed lines are the contour lines of the magnetic field strength.

The sub-photospheric flux tube is buoyantly unstable at two locations along its length, causing two segments of the flux tube to rise. This rise is shown by the magnetic field strength distribution along the flux tube axis at $x = 0$ (e.g. $t = 142.83\,\mathrm{min}$, Fig 4.1a). The segments rise and reach the photosphere simultaneously. There, each of them become compressed and expands horizontally, similar to the case of flux tubes with one rising segment (e.g. Archontis et al., 2004). This compression increases the magnetic field strength at the apex of the segments. Eventually, both segments emerge above the photosphere forming two magnetic lobes (e.g. $t = 178.54\,\mathrm{min}$, Fig 4.1b). At that stage, the photospheric magnetogram shows the formation of two small bipolar regions (Fig 4.2a and Fig 4.2c). The horizontal velocity field (arrows, Fig 4.2a) show the emergence of new flux.

The continuous emergence of new magnetic flux and the expansion of the magnetic lobes eventually brings the two lobes in contact (e.g. $t = 214.3\,\mathrm{min}$, Fig 4.1c). The magnetogram shows two well-formed bipolar regions (e.g. see at $t = 314.3\,\mathrm{min}$, Fig 4.2b and Fig 4.2d). The bipolar region formed at the positive (negative) y-axis is named as BR1 (BR2), with the polarities P1 & N1 (P2 & N2). We refer to the set of N1 and P2 as the outer polarities and P1 and N2 as inner polarities. From the velocity vectors in Fig 4.2b we identify the presence of shearing motions

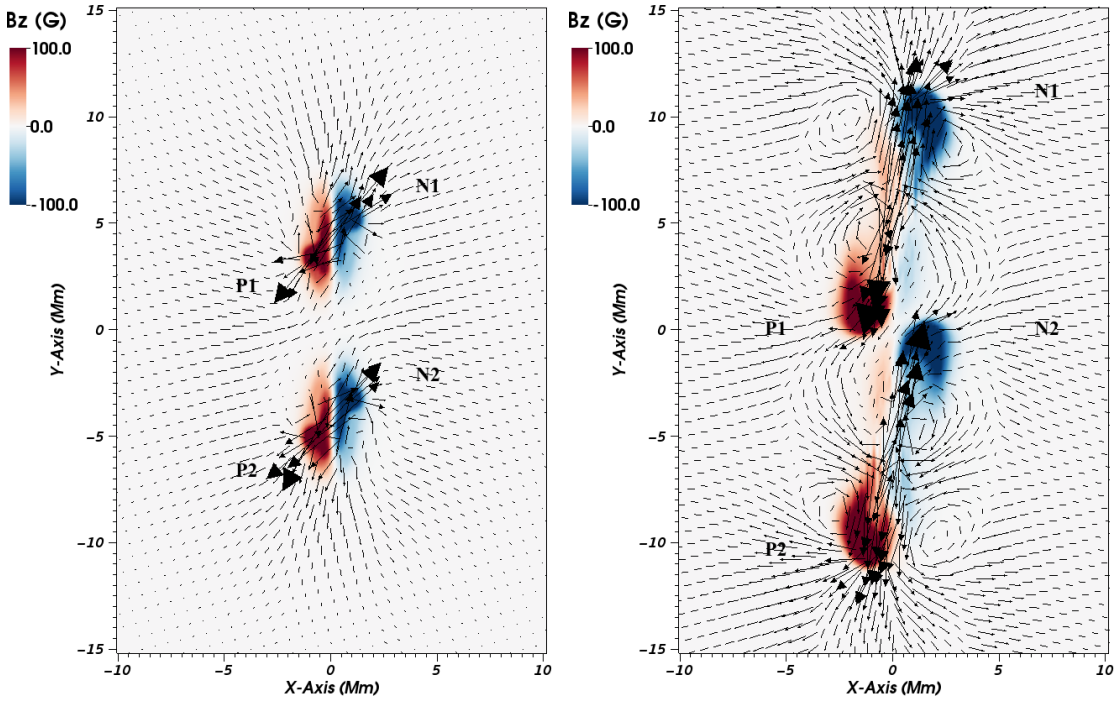

(a) $t = 178.54$ min.

(b) $t = 314.23$ min.

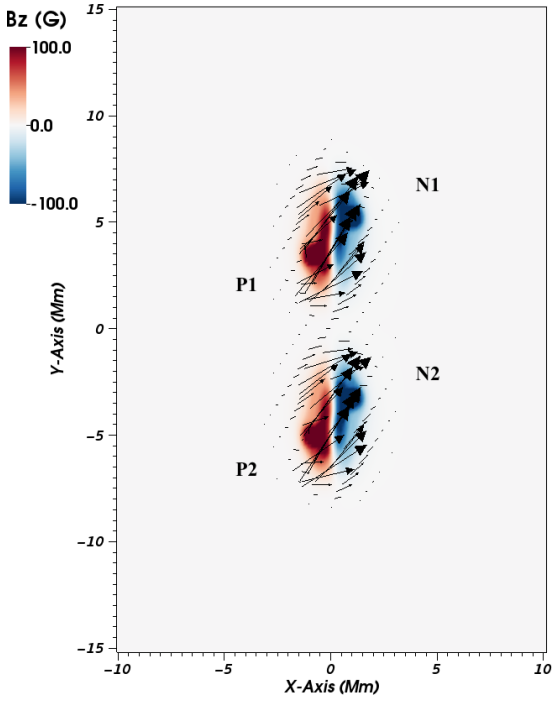

(c) $t = 178.54$ min.

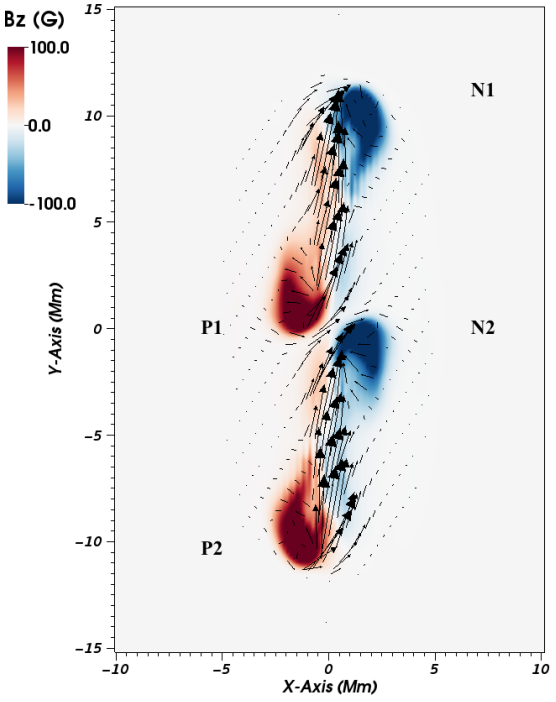

(d) $t = 314.23$ min.

Figure 4.2: The photospheric magnetogram at various times. The overplotted arrows are the horizontal velocity in (a,b), and the projected magnetic field vector in (c,d).

along the PIL of each bipole. In between the inner polarities, we also find shearing motions of lower magnitude.

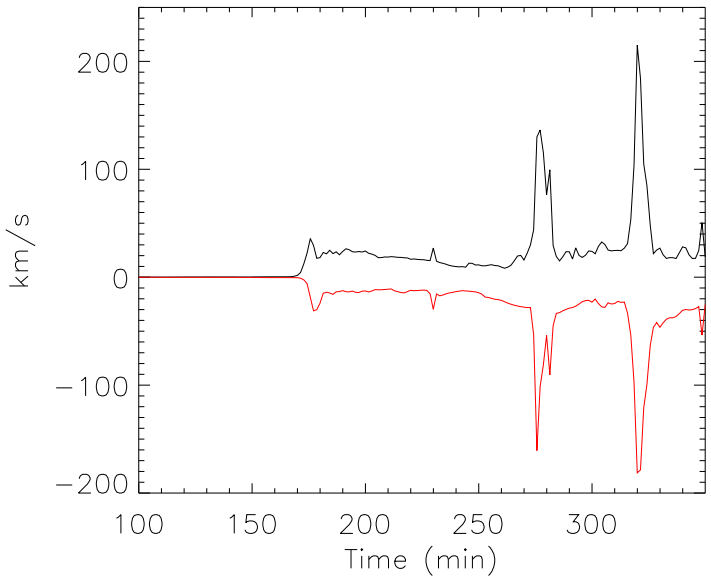

Figure 4.3: Temporal evolution of maximum (black) and minimum (red) v_z above the photosphere.

The interaction of the lobes leads to a series of plasma ejection, as indicated in Fig 4.3 by the maximum (black) and minimum (red) v_z. In general, there is a good temporal correlation between upflows and downflows. We find that these are pairs of bi-directional flows, which emanate from the same region due to reconnection (i.e. reconnection jets). In the same figure, we find some weak upflows with no corresponding downflows. Typically, these are pressure driven plasma ejections, which are emitted upwards when the plasma at the interface between the lobes is compressed.

The first upflow peaks at $t \sim 172\,\mathrm{min}$ is due to the emergence of the flux tube into the photosphere, and the downflow peaks at a slightly later time, showing the gravitational draining of the plasma along the sides of the emerging field. The second peak at $t \sim 230\,\mathrm{min}$ corresponds to the reconnection flow ejected when the two magnetic envelopes (i.e. the outermost field of the emerging lobes) merge together. The two prominent upflow/downflow peaks, which occur at $t \sim 276\,\mathrm{min}$ and $t \sim 320\,\mathrm{min}$, are related to bidirectional flows ejected out of a flare current sheet (i.e. a current sheet around which the temperature increases up to a few million Kelvin). These current sheets are typically located underneath eruptive flux ropes. The formation of these flux ropes will be described later on.

The integrated magnetic (black) and kinetic (red) energy in the corona (Fig 4.4), exhibits two maxima, at the times of the strong upflows. As one should expect, magnetic energy drops (or it shows slower increase rate) before the increase of the kinetic energy. We find that the increase of the kinetic energy occurs during the eruption of dense magnetized material from the low atmosphere, in the form of a twisted flux tube. In the next sections, we will discuss the

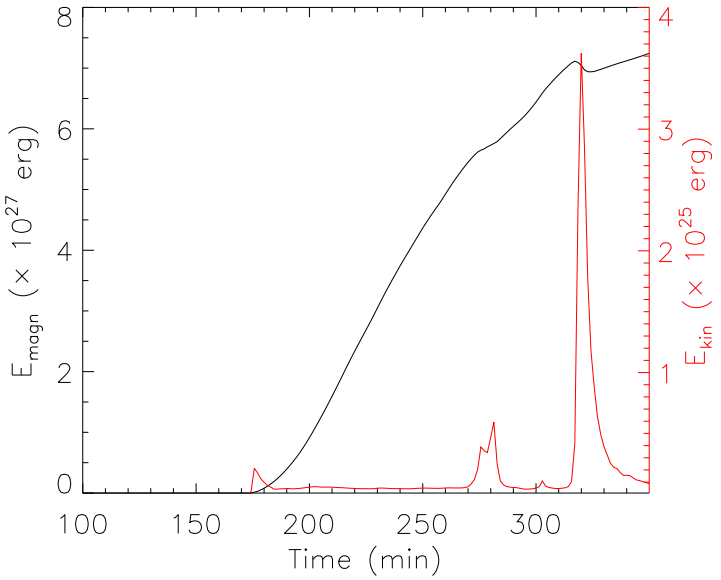

Figure 4.4: Temporal evolution of magnetic (black) and kinetic (red) energy above the corona.

dynamics of these eruptions in more detail. The kinetic energies of these eruptions are $0.6 - 3.6 \times 10^{25}$ erg, while the modulation of the magnetic energy during the eruptions is $1 - 4 \times 10^{26}$ erg. The first rise in kinetic energy ($t = 175$ min) corresponds to the initial emergence of the magnetic field into corona. The magnetic energy gradually increases throughout the simulation, as more magnetic energy is being brought into the atmosphere by the emergence of new magnetic flux.

4.2 First Confined Eruption

We now focus on the first eruption. In Fig 4.5 we show the magnetic field topology at $t = 274.24$ min. Left column shows the side and right column the top view of the field lines. The magnetic lobes come into contact early in the simulation (before $t = 214.25$ min, Fig 4.1c). The blue field lines in Fig 4.5a are the field lines, which have been traced from the apex of each emerging lobe. Therefore, these field lines could be considered as the envelope field lines of each bipole. Notice that viewed from the top (Fig 4.5b), the two sets of blue lines (connecting P1-N1 and P2-N2) have been compressed and adopted an orientation almost parallel to the PIL between P1-N2. A current sheet is formed along the interface between the two systems, marked as upper current sheet in Fig 4.5a. Reconnection between the two lobes of blue field lines form lines connecting the outer polarities (N1-P2, grey colour) and the inner polarities (P1-N2, green colour shown in Fig 4.10c as they are relevant to the second eruption).

For clarity, Fig 4.5c and Fig 4.5d show only the blue and the grey field lines. Notice that the grey lines located higher up have the shape of the blue lines at their flanks. These lines relax downwards and adopt a less-curved orientation (as they are projected onto the xy-plane). We will refer to the grey lines as the overlying field of the flux rope, which will be defined later.

Field lines of the magnetic lobes, which are located lower in height and they have emerged later in the simulation, are more sheared (pink lines connecting P1-N1 and P2-N2, Fig 4.5a and Fig 4.5b). The footpoints of these field lines near the outer polarities have adopted a J-like configuration, due to the rotation of these polarities (see velocity vectors inside the polarities, Fig 4.2b). This J-shape is less apparent near the inner polarities, as the two (pink) sets of field lines come very close together and they start to be deformed (e.g. due to compression of the material there and/or due to reconnection).

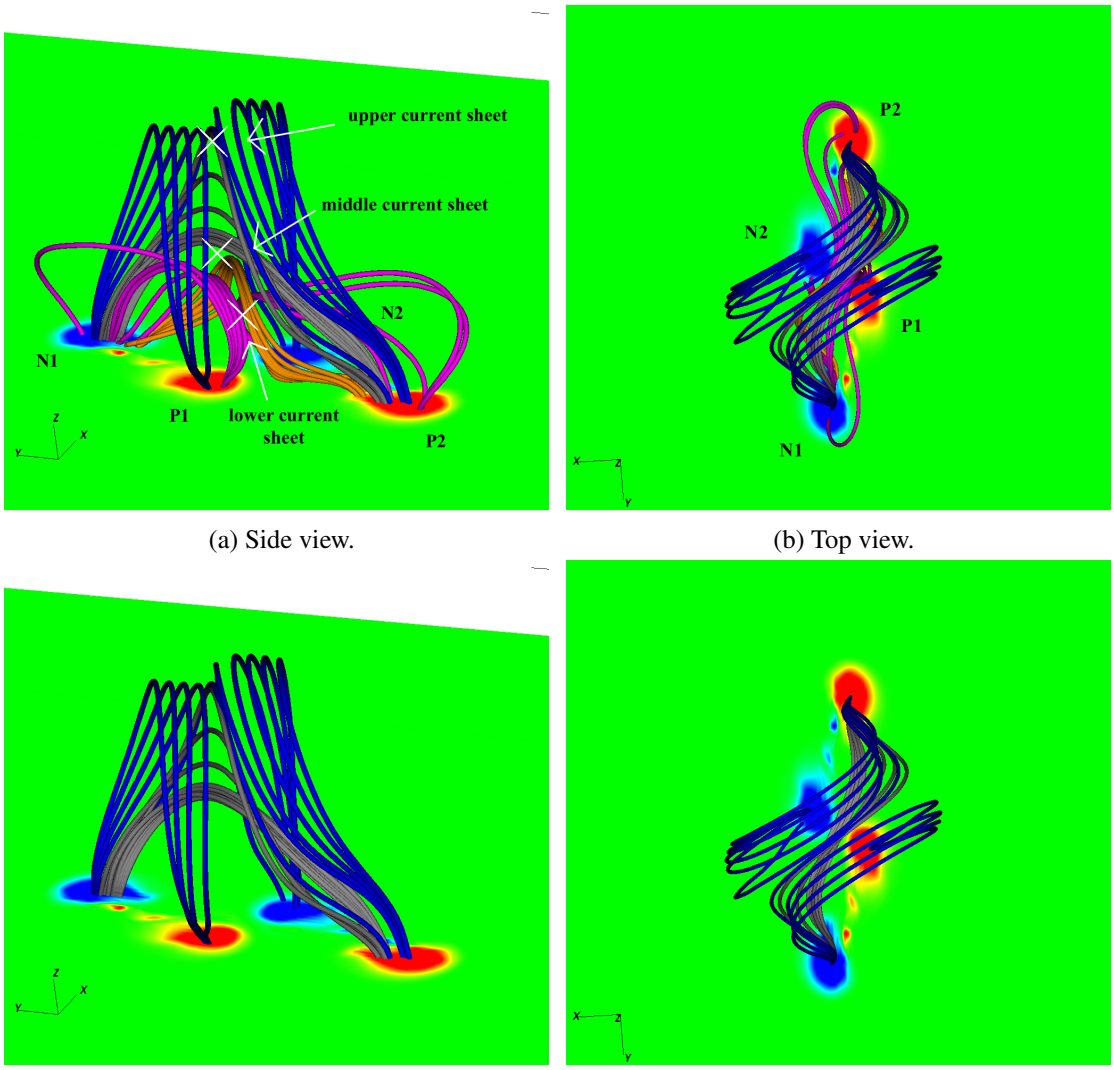

(a) Side view.

(b) Top view.

(c) Side view.

(d) Top view.

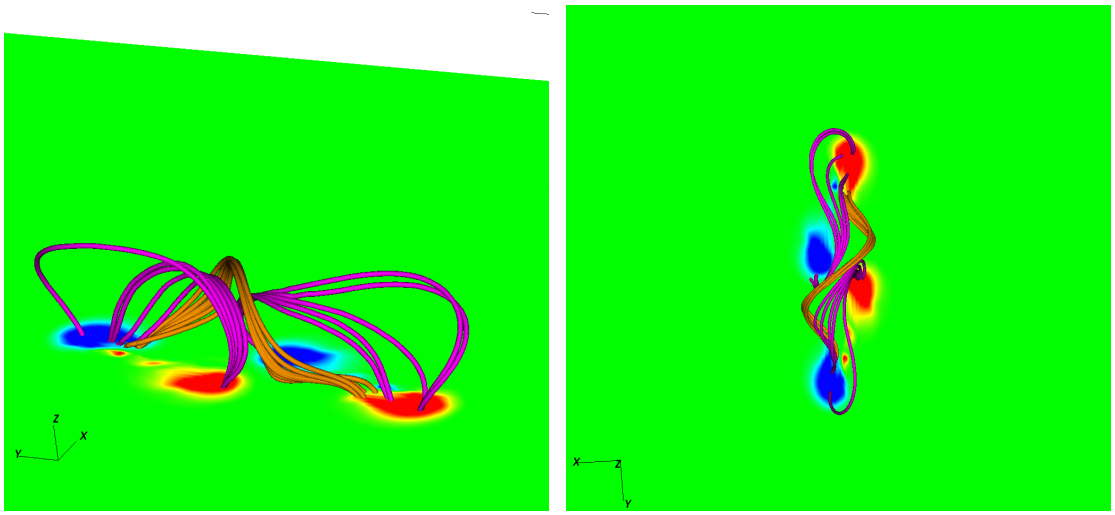

(e) Side view. (f) Top view.

Figure 4.5: The magnetic field line topology at just before the eruption at $t = 274.24\,\mathrm{min}$. The overall magnetic field line topology shown in side view (a) & top view (b). The white crosses indicate the locations where the current sheets are formed. Panels (c) and (d) show the top part of the magnetic field lines system. Blue field lines are part of the outermost magnetic field lobes and the grey field lines result from the reconnection between the two sets of blue field lines. Panels (e) and (f) show the bottom part of the magnetic field line system. Pink field lines are sheared and rotated field lines from each magnetic bipole found lower in height and orange field lines are the result of reconnection between the two sets of pink field lines.

As the pink field lines approach each other above the P1-N2 PIL, a current sheet is formed there, which we name as the lower current sheet. Through this lower current sheet, the (pink) field lines reconnect, forming field lines connecting the outer polarities (N1-P2, orange colour) and the inner polarities (P1-N2, arcade field lines, not shown here). Eventually the orange field lines, which have a mirror S shape, pass through the center of a newly developed flux rope. This system is isolated in Fig 4.5e and Fig 4.5f. Notice that the orange lines have a small amount of twist due to the sheared nature of the pink field lines and the reconnection happening in three dimensions. Also, another current sheet is formed (named as middle current sheet) in between the flux rope lines (orange) and the grey lines.

Now we trace the height-time profile of the flux rope by locating the maximum of the normal component of the magnetic field on a plane perpendicular to the P1-N2 PIL and plot it in Fig 4.6a (black). We have not traced the height before $t = 271.38\,\mathrm{min}$, because we could not spot the center of the flux rope. We find that the flux rope is already on non-linear ascent from $t = 271.38\,\mathrm{min}$ until $t = 275.67\,\mathrm{min}$. The rising motion slows down during the time period $t = 275.67 - 278.53\,\mathrm{min}$. Then we find the rapid rise eruptive phase, which is followed by gradual saturation after $t = 283\,\mathrm{min}$.

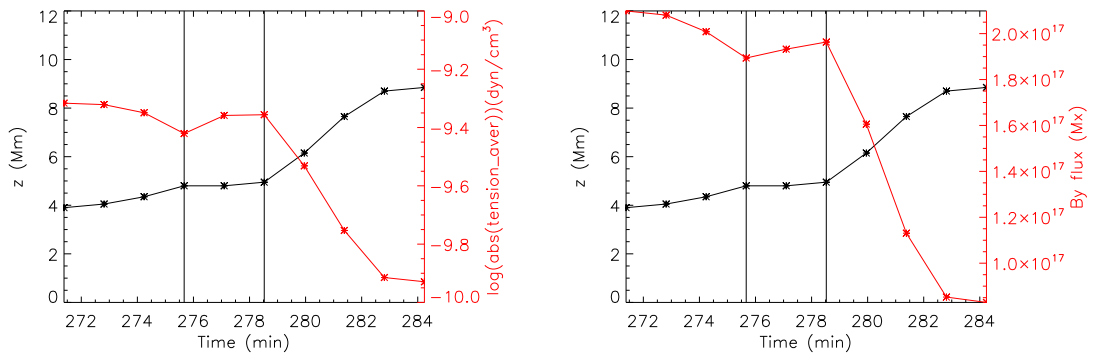

(a) (b)

Figure 4.6: Black line: height-time profile of the first flux rope. (a) Red line: temporal evolution of the average absolute magnetic tension in a cross-sectional cut area above the flux rope. (b) Red line: temporal evolution of the average azimuthal magnetic flux in the same area above the flux rope.

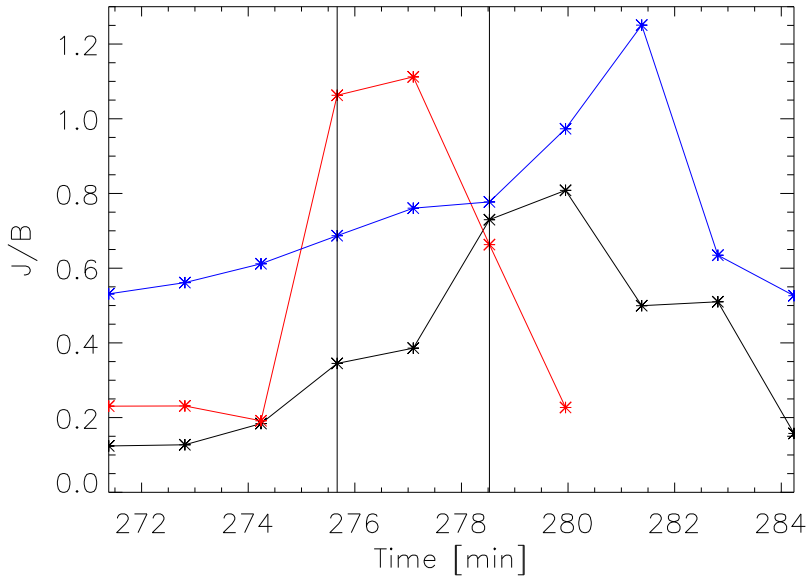

Figure 4.7: Maximum J/B as a function of time for the lower (blue), middle (black) and upper (red) current sheet.

To understand the dynamics of the flux rope's motion, we follow the temporal evolution of the maximum J/B at the lower (blue), middle (black) and upper (red) current sheets in Fig 4.7. During the evolution of the eruption, the lower current sheet acts as the flare current sheet and the middle as the "breakout" current sheet, as we explain in the following.

During the rising phase of the flux rope at $t = 271.38 - 275.67\,\mathrm{min}$, we find that the current

in the lower current sheet increases before the increase in the middle current sheet. This suggests that the initial non-linear rise of the flux rope starts by the (flare) reconnection below the twisted structure. The outflow of this reconnection pushes the flux rope upwards, compressing the flux rope against the overlying field and thus increasing the current in the middle current sheet.

In Fig 4.6a we overplot the average tension above the flux rope (red). Notice that after $t = 272.81\,\mathrm{min}$, when J/B increases in the middle current sheet, the average tension above the flux rope drops, which assists the eruption. This is the result of reconnection of the flux rope (orange) field lines with the overlying (grey) lines of Fig 4.5. Also, this reconnection results in the decrease of the B_y flux in the same region (red, Fig 4.6b). The B_y flux there measures mostly the flux of the grey field lines.

During $t = 275.67 - 278.53\,\mathrm{min}$ the flux rope eruption slows down. As the flux rope is pushed upwards and reconnection occurs both at the lower and middle current sheet, the upper current sheet increases drastically (Fig 4.7, red). The long and thin upper current sheet becomes fragmented, forming two regions of increased current density and triggering fast reconnection flows. This fragmentation could be the result of a tearing instability triggered by the upward motion of the flux rope and the overlying field below the upper current sheet. The result of this increased reconnection is the formation of more overlying (grey) field lines above the flux rope. This is indicated by the increase of the tension above the flux rope (red line increase between vertical lines, Fig 4.6a) and the increase of the B_y flux (red, Fig 4.6b) measuring the flux of the grey field. Still, at the same time the lower and middle current sheet continue to increase (Fig 4.7) but the newly added flux above the flux rope suppresses momentarily the eruption.

Once this sudden increase of the upper current sheet starts to decrease (J/B drop, red line at $t = 278.53\,\mathrm{min}$, Fig 4.7), the flux rope continues the exponential rapid rise phase of the eruption (Fig 4.6, black line). After $t = 278.53\,\mathrm{min}$, both the tension above the flux rope (Fig 4.6a) and the B_y flux (Fig 4.6b) decreases, due to the reconnection of flux rope lines with the overlying field.

This reconnection between the two systems is illustrated in Fig 4.8a and 4.8b from a side and top view respectively. The purple isosurface shows the middle current sheet. The blue field lines are the result of this reconnection. Eventually, the suppressing force of the overlying field slows down the flux rope, and both the lower and middle current sheet magnitude decrease leading to a confined eruption. The confined flux rope at $t = 282.81\,\mathrm{min}$ is shown in Fig 4.9.

4.3 Second Confined Eruption

We now focus on the second eruption. In Fig 4.10a and Fig 4.10b we plot the magnetic field topology at $t = 314.23\,\mathrm{min}$. We find the same field line structures as in Fig 4.5a and 4.5b and thus

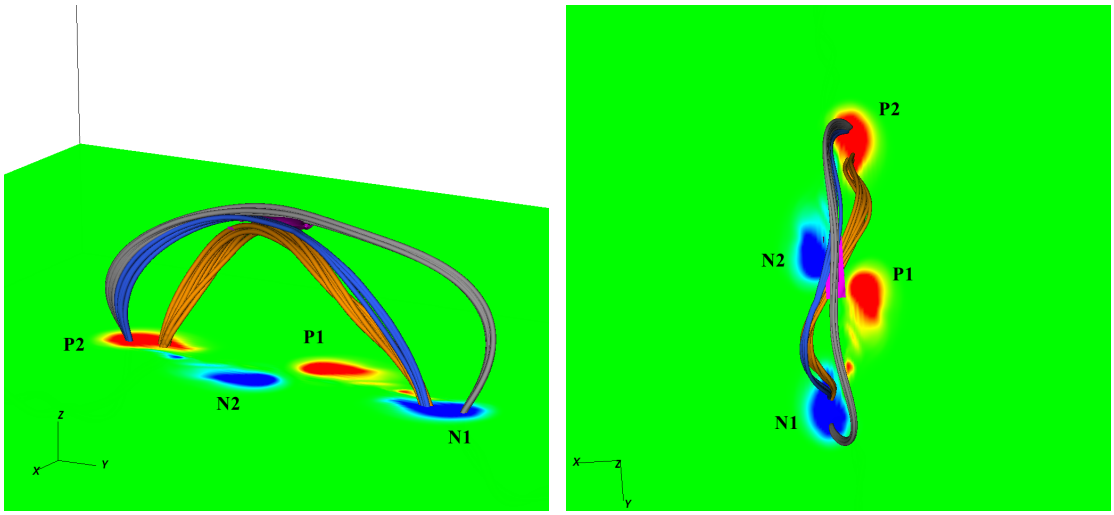

(a) Side view. (b) Top view.

Figure 4.8: Side (a) and top (b) view of the magnetic field line topology at $t = 281.38\,\mathrm{min}$, showing the reconnection of field lines between the flux rope and the overlying field. Purple isosurface is the middle current sheet.

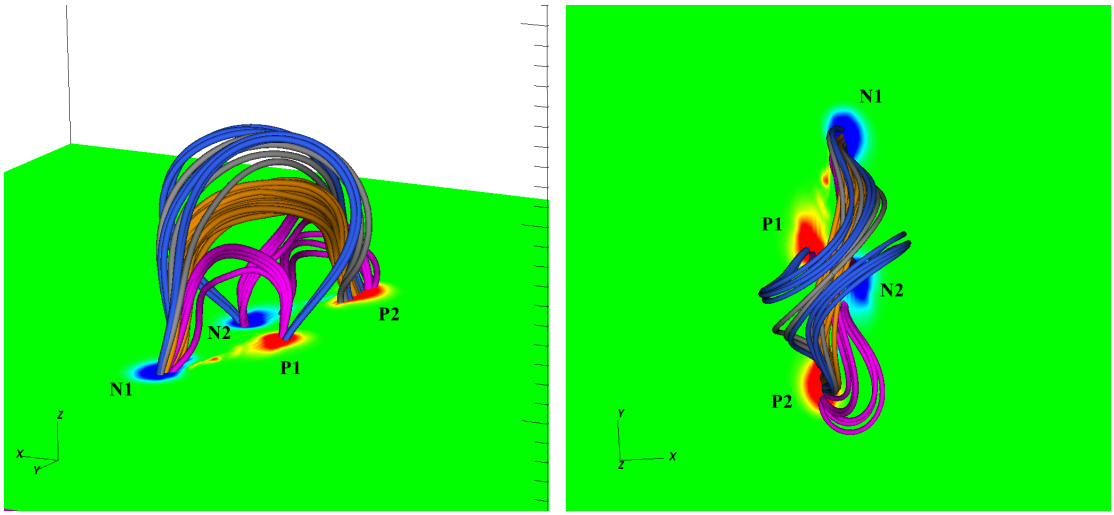

(a) Side view. (b) Top view.

Figure 4.9: Side (a) and top (b) view of the magnetic field line topology of the first eruption at $t = 282.81\,\mathrm{min}$.

we only plot the lower structures that are more important for the second eruption. We find again the lower lying, more sheared lobe lines connecting the two bipoles (P1-N1, P2-N2, pink). These lines reconnect forming a small twisted flux rope. Above the flux rope, we find again overlying field lines connecting the outer polarities (grey). These lines are located in the same manner as in the first eruption (reconnection from the higher lying lobes, blue in Fig 4.9a). Some of the grey lines are twisted, although we cannot find any structure associated with the first flux rope.

We trace the height time profile of the second flux rope in Fig 4.11 (black line) and over plot the average absolute magnetic tension force above the flux rope (red). Notice that the non-linear rise phase begins at $t = 312.81\,\mathrm{min}$ (first vertical line) and the rapid rise of the flux rope begins at $t = 317.09\,\mathrm{min}$ (second vertical line).

In Fig 4.12a we plot the v_z distribution along $(0, 0, z)$. From $t = 311.4\,\mathrm{min}$ (black line) to $t = 312.8\,\mathrm{min}$ (red line), we have the gradual development of a bidirectional flow (around $z = 3.1\,\mathrm{Mm}$) which is a proxy of increased reconnection at the current sheet below the flux rope. This reconnection outflow increases steadily (blue and green lines for $t = 314.2,\ 315.7\,\mathrm{min}$) and eventually becomes a strong reconnection jet ejected out of the flare current sheet during the rapid rise of the flux rope (blue, green lines, Fig 4.12b).

Notice that in Fig 4.12a, at $z = 6.5\,\mathrm{Mm}$, we find another small bidirectional flow. This is due

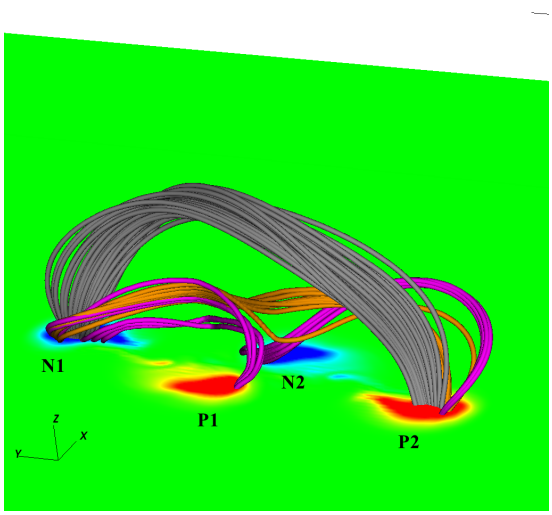

(a) Side view, at $t = 314.23\,\mathrm{min}$.

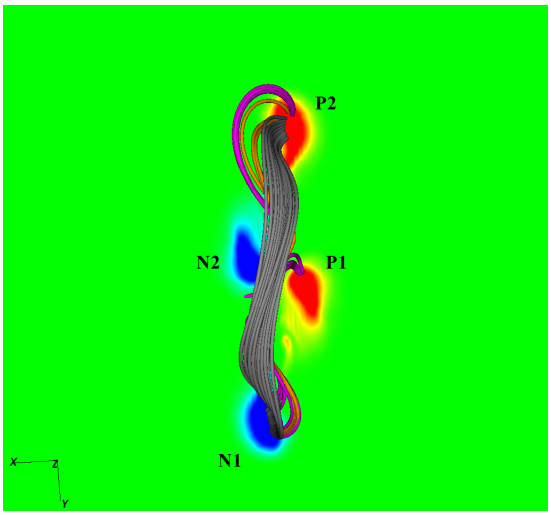

(b) Top view, at $t = 314.23\,\mathrm{min}$.

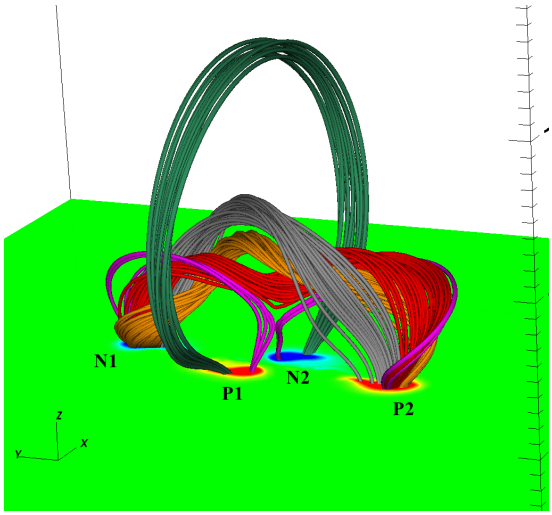

(c) Side view, at $t = 318.52\,\mathrm{min}$.

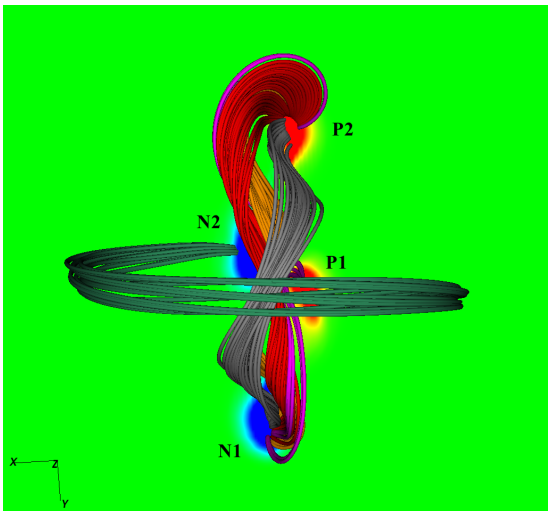

(d) Top view, at $t = 318.52\,\mathrm{min}$.

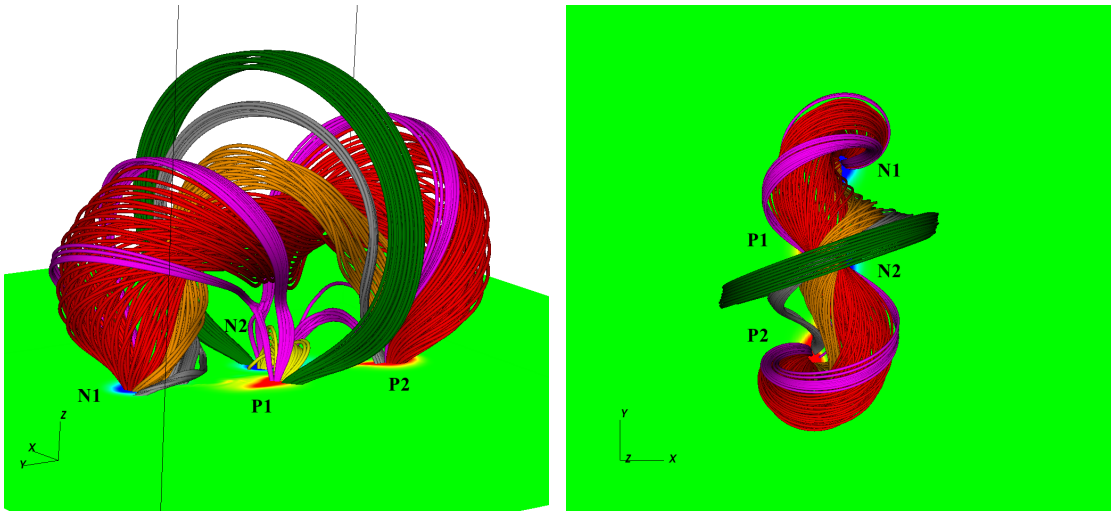

(e) Side view, at $t = 321.38\,\mathrm{min}$.

(f) Top view, at $t = 321.38\,\mathrm{min}$.

Figure 4.10: Side view (a) and top view (b) of the magnetic field line topology of the second flux rope at $t = 314.23\,\mathrm{min}$. The field lines have the same characteristic as in the previous eruption and are coloured as in Fig 4.9. Panels (c) and (d) show the flux rope during the eruption at $t = 318.52\,\mathrm{min}$. Green lines are reconnected field lines between the blue lines of the magnetic lobes of Fig 4.9 acting as a strapping field. Panels (e) and (f) show the magnetic field line topology at $t = 321.38\,\mathrm{min}$ when the erupting flux rope is confined. The yellow field lines connecting the inner polarities (P1-N2) are the post-reconnection arcade loops.

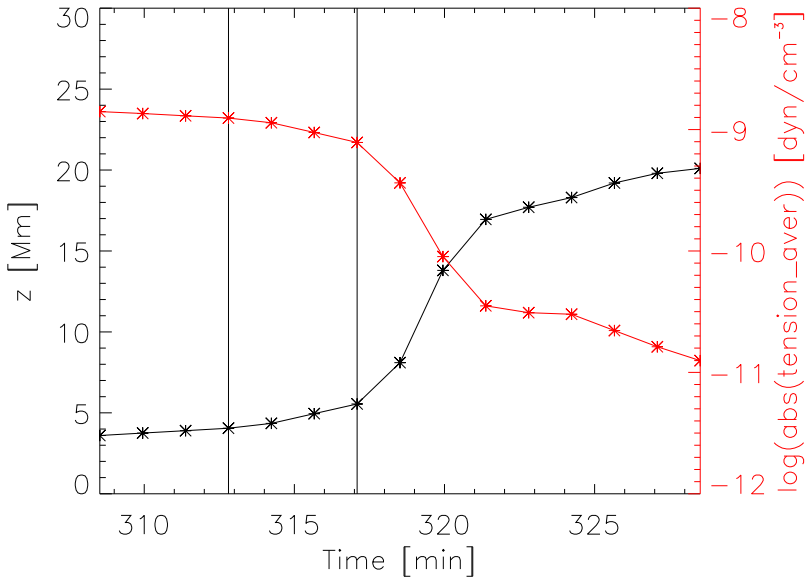

Figure 4.11: Black line: height-time profile of the second flux rope. Red line: temporal evolution of the average absolute magnetic tension above the flux rope.

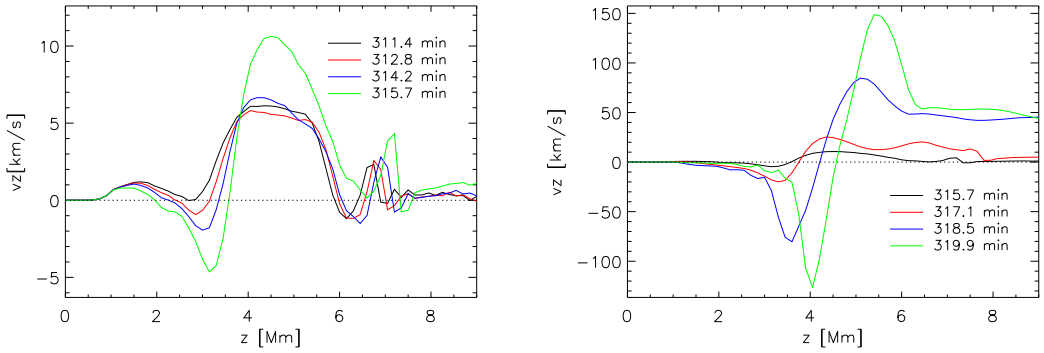

(a) $t = 311.4 - 315.7\,\mathrm{min}$. (b) $t = 315.7 - 319.9\,\mathrm{min}$.

Figure 4.12: The v_z distribution along $(0, 0, z)$ at different times (marked with different colours shown at the legends). Panel (a) continues to panel (b) and both show $t = 315.7\,\mathrm{min}$ as a reference.

to the presence of the current sheet above the flux rope (middle current sheet). This increases only by a small amount indicating that the middle current sheet does not have a major role at the initial phase of the second eruption. However, this small bidirectional flow is responsible for the small drop of the average tension above the flux rope between $t = 312.8\,\mathrm{min}$ and $t = 318.5\,\mathrm{min}$ (red line, Fig 4.11). As a result, the initial rise of the flux rope is mostly driven by the reconnection at the current sheet below the flux rope, similar to the first eruption.

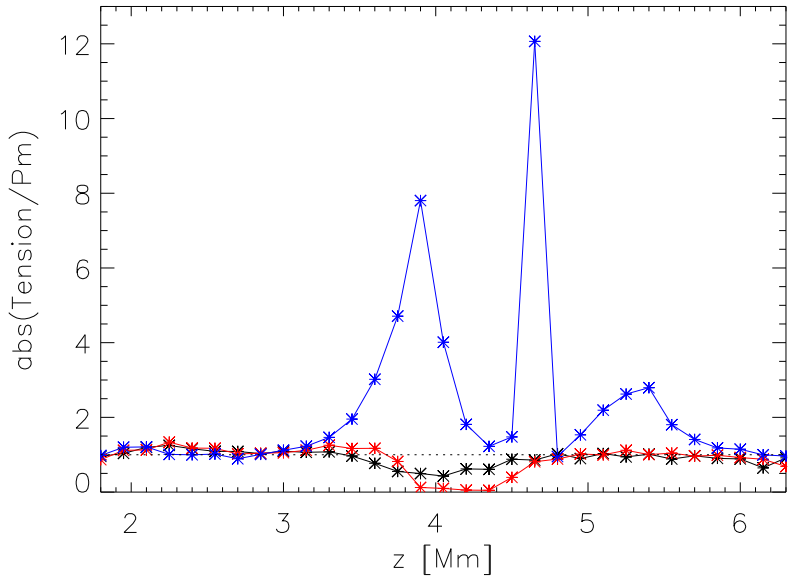

Figure 4.13: The ratio of the absolute value of the vertical component of the magnetic tension force over the magnetic pressure force along $(0, 0, z)$ before (black, red) and during (blue) the flux rope's rapid rise phase at time $t = 314.2, 315.7, 317.1\,\mathrm{min}$ respectively.

In Fig 4.13 we plot the absolute value of the ratio of vertical component of the magnetic tension force over the magnetic pressure force, along height at $(0, 0, z)$. Before $t = 317.1\,\mathrm{min}$ (second vertical line of Fig 4.11), the dominant force pushing the flux rope upwards is the magnetic pressure. During the rapid rise (after $= 317.1\,\mathrm{min}$), we find that the magnetic tension force becomes up to 12 times higher than the magnetic pressure force. So, the rapid rise phase of the flux rope eruption is driven upwards by the sudden increase of upwards tension below the flux rope. This release of tension occurs from the reconnection of low-lying sheared field lines (pink, Fig 4.10c, 4.10d). The orange field lines constitute the erupting core of the ejected material. The reconnection of the pink lines through the flare current sheet during the eruption forms the red flux rope lines, which wind about the orange field lines. The increased upward tension found in Fig 4.13 originates from the U shaped part of the red field lines above the P1-N2 region.

The sudden rising motion of the flux rope causes its upper part (orange lines) to be compressed against the overlying field (grey lines), increasing the intensity of the middle current sheet (above the flux rope). This enhances reconnection at that region, causing the decrease of tension after $= 317.1\,\mathrm{min}$ (red, Fig 4.11). In Fig 4.14 we plot the Joule heating term along the z-axis. The maxima marked with vertical lines correspond to the location of the middle current sheet. We see that the current becomes smaller after $t = 320\,\mathrm{min}$, resulting in a less steep decrease of tension. When the eruption becomes confined, this current sheet decreases further.

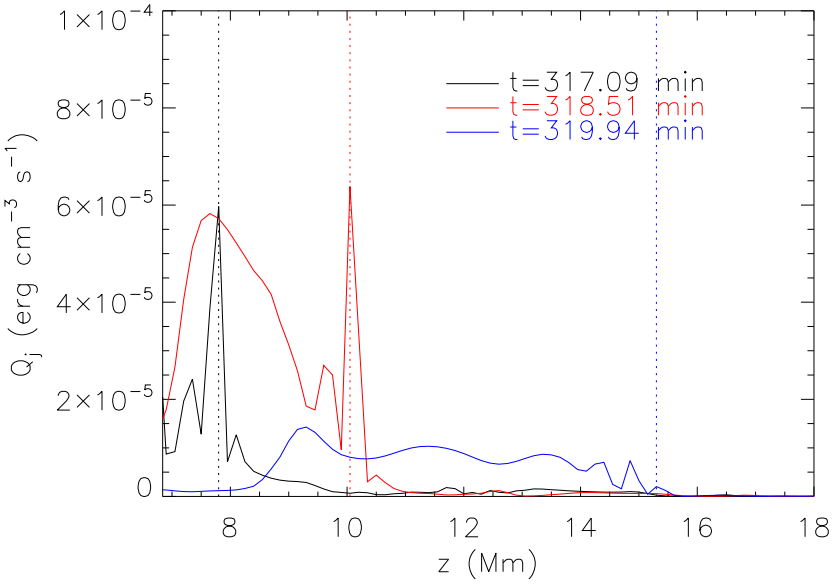

Figure 4.14: The joule heating (Q_j) term along $(0, 0, z)$ at different times. The vertical dashed lines indicate the location of the current sheet above the flux rope these times.

The flux rope becomes confined after $t = 321.5\,\mathrm{min}$. In Fig 4.10e and 4.10f, we show the field lines of the confined system. Both the green and grey overlying lines (which both are the result of

the reconnection of the blue lines of Fig 4.9a) suppress the eruption. The (low-lying) sheared field lines (pink) have been pushed upwards by the eruption and they envelope parts of the flux rope. As a result, the red lines (reconnected pink lines) eventually wrap around the flux rope core (orange). Between the inner polarities and below the erupting structure we find the post-reconnection (flare) arcade (in yellow), which has temperatures up to 4×10^6 K. We do not find that the upper current sheet plays any role during the second eruption.

The mechanism of how the second eruption is triggered is similar to the first. First we find the onset of the flare current sheet, which produces a fast reconnection jet and leads to strong upward tension. The upward motion of the flux rope enhances the current sheet above the flux rope. There, reconnection between the flux rope and the overlying field lines causes a drop of the overlying tension, assisting the eruptive process. Because this tension is not completely (and efficiently) removed, the eruption becomes confined by the overlying field.

The second eruption is faster and more energetic and eventually becomes bigger in both size and flux. There are various reasons for this. During the eruptions, the magnetic energy (Fig 4.4) and the photospheric unsigned flux still increase. The magnetic lobes and the overlying fields continue to expand as more energy and flux are injected into the atmosphere. As a result, the tension of the overlying field drops due to the expansion and, thus, the second flux rope has lower magnetic tension above it during the initial phase of the eruption (Fig 4.6a and Fig 4.11). Hence, the second flux rope needs less force to overcome the strapping fields above it.

Another important element is the fact that for the second eruption the flare reconnection lasts longer, produces faster jets and releases more tension. This accelerates more and adds more flux into the second flux rope. There are two possible reasons for that. Firstly, the inner polarities are closer together between them in the second eruption. This causes the field lines to reconnect having higher angles between them, leading to more efficient reconnection. Also, more shear will be induced into the system as the inner polarities come closer. Secondly, the polarities of each of the bipoles have rotated more, making the field lines become more curved and, thus, the angle of reconnection increases further (pink lines, Figs 4.5a and 4.10a). The combination of the above could lead to the onset of the more energetic second eruption.

4.4 Discussion

We performed numerical simulations of magnetic flux emergence into a null corona. We used a sub-photospheric magnetic flux tube with a density deficit along its axis, which led to the emergence of a quadrupolar region at the photosphere.

During the evolution of the system, the polarities from each bipole drift apart from each other.

Subsequently, the outer polarities (N1 & P2) move away from the center of the EFR, and the inner polarities (N2 & P1) moving closer to each other. This induces a magnetically-driven shearing motion along the PIL between the inner polarities and the formation of new magnetic flux ropes (at two different times during the experiment) through reconnection of sheared field lines. We find that the flux ropes erupt but not in a fully ejective manner. Namely, the flux ropes do not escape but they become confined by the overlying (envelope) field of the EFR. This is an important result, because it shows that eruptions do occur in quadrupolar EFRs. In fact, our results are different from recent similar studies by other groups. For instance, Toriumi et al. (2014) reported that they did not find eruptions (and the associated flaring underneath the erupting field) in their numerical simulations mainly because there was no formation of an erupting flux rope after the interaction between the emerging loops; Also, Fang and Fan (2015) reported that there was no formation of a coherent helical coronal flux rope in the EFR in their experiment. This could be due to large numerical diffusion because of the low resolution in the outer solar atmosphere in their numerical simulation. Thus, this study also did not show ejective eruption(s) of flux ropes, which could lead to blowout jets. Therefore, although our numerical experiment is similar to the aforementioned studies, our results are different mainly because we find that in quadrupolar regions, reconnection of sheared fields leads to recurrent ejective eruptions. Also our numerical results come into agreement with many observations, which show intense solar activity in such regions (including jets and flaring of plasma).

Finally, we investigated the nature of the eruptions during the emergence. We found that both eruptions are triggered by a similar mechanism, which is associated with reconnection at the flare current sheet and the release of tension of the field above the erupting flux rope. To reach this conclusion, we used 3D visualization of field lines and 1D plots of several quantities, such as current density, tension of field lines, etc. Although, the solar corona in our experiment is highly idealized (i.e. non-magnetized), the results strongly suggest that emerging quadrupolar regions can provide the energy to power (recurrent) eruptions of dense plasma in the solar atmosphere. Thus, one of the main aims in this experiment, was to investigate the dynamics of emergence and the associated activity, without considering the interaction between emerging and ambient magnetic fields. In the next section(s), we present results from experiments that include a more realistic corona (i.e. we add a magnetic field in the upper solar atmosphere).

Chapter 5

Emergence Into a Magnetized Corona: Jets and Eruptions

In this chapter we consider a more realistic approach for simulating the quadrupolar EFR. We study the emergence of a magnetic flux tube into a magnetized corona instead of an empty and non-magnetized (null) corona. The model is chosen to be the same as the previous simulation, apart from adding an ambient magnetic field in the corona.

5.1 Initial Conditions and Emergence to the Photosphere

A twisted magnetic flux tube is initially placed beneath the solar surface. The magnetic field distribution along the flux tube is defined as

$$B_y = B_0 \exp\left(-\frac{r^2}{R^2}\right), \tag{5.1}$$

$$B_\theta = \alpha r B_y, \tag{5.2}$$

where $B_0 = 2.4 \times 10^3$ G is the initial field strength of the flux tube. $R = 450\,\mathrm{km}$ is the radius of the flux tube, and $r = \sqrt{x^2 + (z - z_0)^2}$ is the radial distance from the axis of the tube. α is the twist of the tube, and is set to be $2.2\,\mathrm{km}^{-1}$, which makes the initial flux tube marginally stable to the kink instability. A density deficit is introduced along the flux tube's axis, and has the form of

$$\Delta\rho = \frac{p_t(r)}{p(z)}\rho(z) \exp\left(-\frac{y^2}{\lambda^2}\right) \sin^2\left(\frac{2\pi y}{\omega}\right), \tag{5.3}$$

such that when the flux tube emerges into the photosphere, it forms a quadrupolar region. p_t is the pressure within the flux tube, and λ is the buoyant part of the flux tube, which is set to be $3.6\,\mathrm{Mm}$. $\omega = 31.5\,\mathrm{Mm}$ is a parameter which is defined as half of the flux tube length.

The coronal magnetic field is defined as

$$B_c = B_c(z)(0, \cos\theta, \sin\theta), \tag{5.4}$$

where θ is the relative inclination angle between the ambient field and the y-axis. The coronal field strength has the following distribution function,

$$B_c(z) = bcor \cdot \left(\frac{\tanh(z-7)+1}{2}\right), \tag{5.5}$$

for $bcor$ the coronal field strength is set to be $bcor = 3\,\mathrm{G}$ in this case. The simulation is carried out in a 420^3 numerical grid box. This represents a numerical domain of $[-31.5, 31.5]\ \mathrm{Mm} \times [-31.5, 31.5]\ \mathrm{Mm} \times [-5.4, 57.6]\ \mathrm{Mm}$ in the direction perpendicular to the tube axis (x), along the tube axis (y), and the vertical (z) direction accordingly. The side boundaries (x, y boundaries) are set to be periodic, and an open boundary is implemented at the top of the numerical box, which allows plasma to flow out of the domain. The bottom boundary is set to be closed, which is a non-penetrating conducting wall.

Figure 5.1 here shows a rough sketch of the initial magnetic field line topology, where the red field line represent the overlying oblique coronal ambient field, and the blue field lines the twisted magnetic flux tube.

Initially, the magnetic flux tube is placed at $2.1\,\mathrm{Mm}$ beneath the photosphere. Thermal equilibrium is satisfied between the flux tube and the surrounding area:

$$T_t = T_{ext}, \tag{5.6}$$

where T_t is the temperature within the flux tube and T_{ext} the temperature of the surrounding area. The pressure between the flux tube and the surrounding area is in balance so that:

$$p_{tg} + p_{tmag} = p_{ext}, \tag{5.7}$$

where p_{tg} is the gas pressure within the flux tube, p_{tmag} is the magnetic pressure within the flux tube, and p_{ext} is the surrounding gas pressure. From equation 5.7, since $p_{tmag} > 0$, $p_{tg} < p_{ext}$. And from the ideal gas law

$$p = \rho R T, \tag{5.8}$$

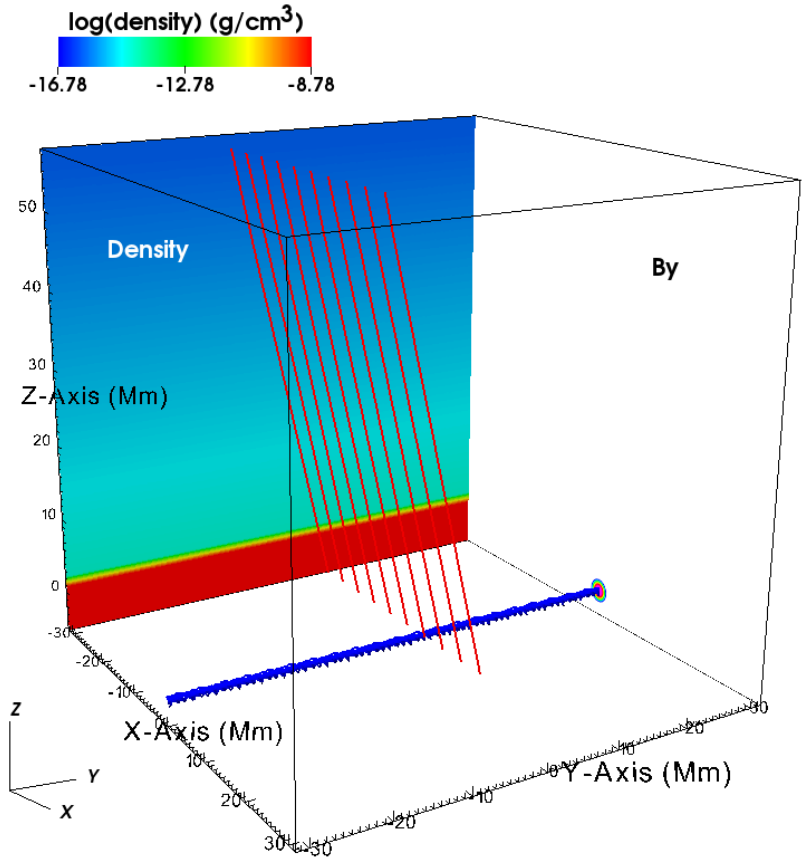

Figure 5.1: The red field lines are a group of selected coronal magnetic field lines. The blue magnetic field lines at the bottom of the box represent the twisted magnetic flux tube initially placed beneath the solar surface. The contoured $y - z$ plane shows the density distribution in the background atmosphere. The $x - z$ plane shows the B_y distribution.

we thus know that $\rho_t < \rho_{ext}$, where ρ_t is the density within the flux tube and ρ_{ext} the density surrounding the flux tube. This results in the density of the flux tube being less than the surrounding area, thus the flux tube becomes buoyant and it rises towards the photosphere. With the density deficit applied along the flux tube, the center part of the tube would rise faster due to a lower density comparing to the rest of the tube. The double Gaussian distribution of the density deficit would then form two bipolar regions, when the magnetic field emerges at the photosphere, as shown in Figure 5.2a.

Figure 5.2b shows the magnetogram at $t \approx 237.1\,\mathrm{min}$. The arrows show the projected full magnetic field vector onto the plane. The polarities of each bipolar region move away from each other along the y-direction. This relative motion induces a shearing along the polarity inversion line (PIL) between the involved polarities (P1 & N1; P2 & N2), which eventually leads to the formation of a flux rope (e.g. Section 3.2.1, Manchester et al. (2004); Archontis and Török (2008)).

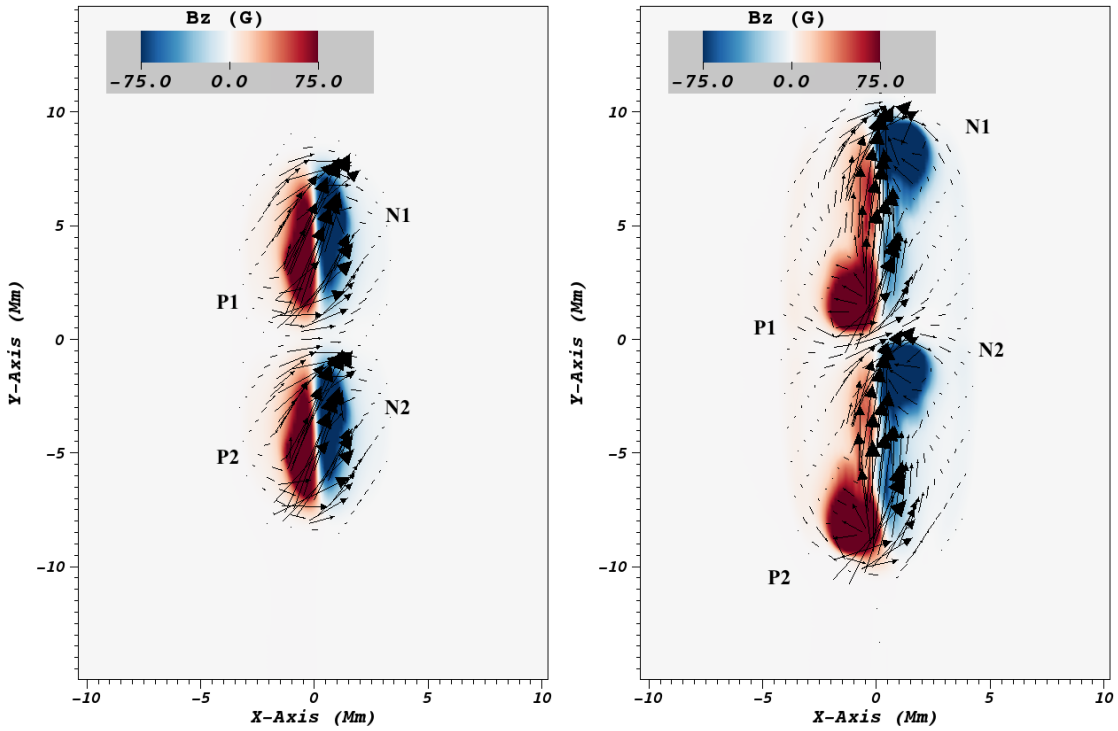

(a) $t \approx 165.7\,\mathrm{min}$ (b) $t \approx 237.1\,\mathrm{min}$

Figure 5.2: Magnetogram at the base of the photosphere ($z = 0$) at two times. Red contours show positive B_z and blue contour the negative B_z. The arrows represent the projected overlying magnetic field vector. (a) The formation of the quadrupolar region when the flux tube emerges into the photosphere. (b) The polarities from each bipole move away from each other along the y-direction. A movie of the temporal evolution of the magnetogram is included in the attached CD (movie1.mp4).

Moreover, as the inner polarities (P1 & N2) come closer to each other, shearing motions develop seen along the PIL between P1 and N2.

5.2 Reconnection Jets and Eruptions

Figure 5.3 shows the temperature (Figure 5.3a) and vertical velocity (Figure 5.3b) distribution along the flux tube at $x = 0$, during $t \approx 165.7\,\mathrm{min}$, same as in Figure 5.2a. As a result of the emergence into the photosphere, two magnetic 'hills' are formed. In 3D, each 'hill' correspond to a small bipolar region with a fan-like shape due to the expansion of its embedded field lines in the 3D volume. A reconnection jet is seen to be emitted from the top of each magnetic 'hill', due to the reconnection between the field lines of the emerging field and the coronal ambient field during the emergence process. The upward flow moves at a maximum velocity of $70\,\mathrm{km\,s^{-1}}$ with temperature up to $8 \times 10^5\,\mathrm{K}$ within the jet channel. The temperature at the reconnection site

reaches up to 1×10^6 K.

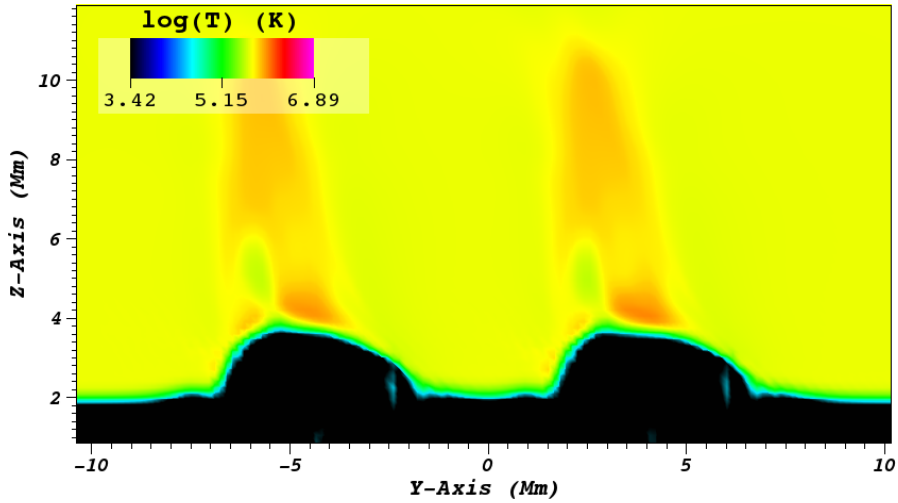

(a) The temperature distribution along the flux tube.

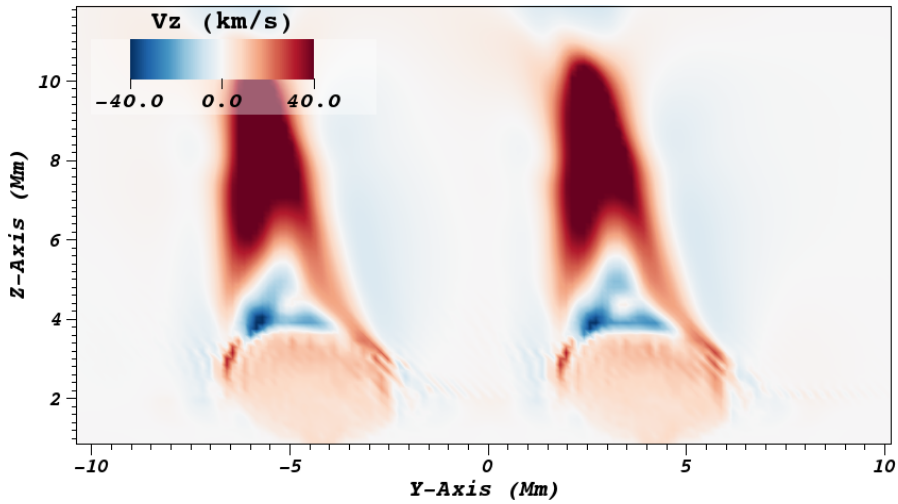

(b) The vertical velocity (v_z) distribution along the flux tube.

Figure 5.3: Taken at $t \approx 165.7\,\mathrm{min}$, when the flux tube emerges into the photosphere, showing the jet emitted as a result of the reconnection between the emerging magnetic field and the coronal ambient field.

Figure 5.4 shows the temporal evolution of the maximum (black) and minimum (red) vertical velocity (v_z) of the system above the photosphere. Overall, 6 main 'events' are found during which the local maximum and minimum v_z are in the range of $100 \sim 250\,\mathrm{km\,s^{-1}}$. Notice that in all 'events' there is a very good temporal correlation between the minimum and the maximum value of the vertical velocity. We have also found that there is a close spatial correlation between the local minima and maxima of v_z (although, not shown here). The first event (i.e. at $t \approx 165.7\,\mathrm{min}$) corresponds to the first reconnection jet, which follows the initial emergence and the interaction between the emerging and the ambient field. Similarly, in the following five events the local extrema of v_z correspond to bidirectional flows, which occur due to magnetic reconnection at

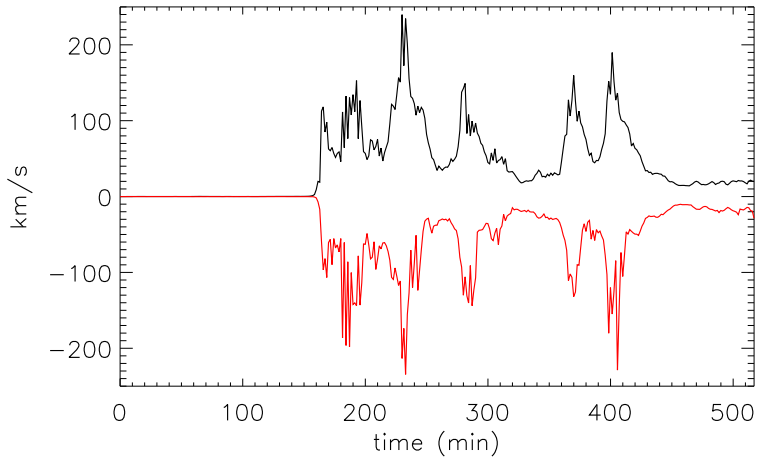

Figure 5.4: Temporal evolution of the maximum upflow (black) & downflow (red) velocity (v_z), above the photosphere.

various locations within the EFR.

The second main event, which occurs around $t \approx 185 \sim 210\,\mathrm{min}$ with max $v_z \sim 150\,\mathrm{km\,s^{-1}}$, corresponds to an eruption that originates from the PIL between P1 & N2. This eruption triggers an external reconnection jet as a result of the interaction between the erupting material and the pre-existing magnetic field. However, the magnetic pressure force of the erupting field is less than the downward tension of the magnetic field lines above it and, thus, the erupting field remains confined by the ambient magnetic field. In this case, the produced reconnection jet does not evolve into a "blowout" jet but it has the characteristics and physical properties of a standard reconnection jet. Since these standard reconnection jets are well studied in the literature (e.g. Archontis and Hood, 2013), in the following we focus more on the remaining four main 'events', which correspond to "blowout" jets.

Figure 5.5 shows the height-time profile of the running difference plot for the integrated plasma density $\int \rho^2\,\mathrm{d}x\mathrm{d}y$, with temperature greater than $8 \times 10^5\,\mathrm{K}$. Black contours indicate a positive difference (between the present time and the previous time at the same height), while white contours represent a negative difference. The steep vertical slope at the end of each black region suggests that most of the dense plasma is ejected upwards. The white region in each event gets broader at the lower height, indicating gravitational draining on part of the erupting plasma. Apart from the main events (i.e. the four large peaks shown in the figure), which actually correspond to "blowout" jets, there are times where the dense plasma seems to undergo an ejective phase but it does not reach the higher corona. These small spikes correspond to various events such as small-scale confined eruptions, reconnection jets, and short-lived pressure driven jets that emanate from various locations within the EFR. (e.g. $t \approx 190 \sim 210\,\mathrm{min}$, $t \approx 310 \sim 320\,\mathrm{min}$).

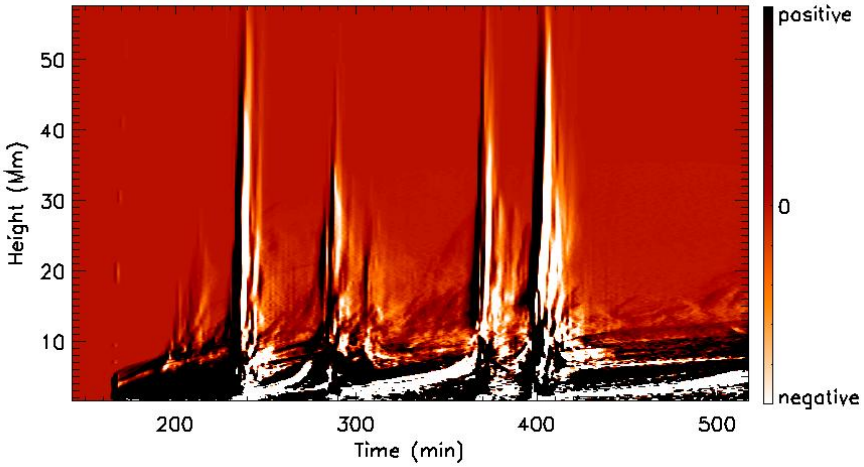

Figure 5.5: Height-time diagram of running difference plot for $\int \rho^2 \, \mathrm{d}x\mathrm{d}y$, where $T > 8 \times 10^5$ K.

Comparing the two figures (Figure 5.4 and Figure 5.5), we notice that there is a good temporal correlation between the bi-directional flows and the ejections of dense material.

5.3 "Blowout" Jets: Onset and Evolution

In the following, we show that these events are eruptions of cool material that trigger external reconnection and drive "blowout" jets. This is in agreement with the scenario suggested by Moore et al. (2010), in order to explain the nature of the "blowout" jets.

Figure 5.6 shows the temperature (Fig 5.6a) and density (Fig 5.6b) distribution respectively during the first eruptive event within the EFR. The vertical 2D-slice is taken at $y \approx -2\,\mathrm{Mm}$ (within BR2) and at $t \approx 230.0\,\mathrm{min}$. The cool material (in light/dark blue color, Figure 5.6a) that rises sideways forms the core of the erupting plasma. The eruption induces an inflow towards the interface, between the field that envelopes the erupting material (hereafter, envelope field) and the ambient field. The envelope field consists of field lines, which surround the erupting core and they do not belong to the eruptive structure. The inflow leads to more efficient external reconnection at the interface, causing the onset of hot and fast external reconnection jet(s). Due to reconnection, an external arcade is then formed underneath the reconnection site. The temperature at the reconnection site reaches up to 3.5×10^6 K, whereas the temperature of the external arcade reaches up to 5.5×10^6 K.

Figure 5.7 shows the temperature (Fig 5.7a) and density (Fig 5.7b) distribution when the erupting core is ejected along the reconnected field lines of the system (at $t \approx 232.8\,\mathrm{min}$). Following the eruption, dense material is emitted along the jet channel, as shown in Figure 5.7b. An internal

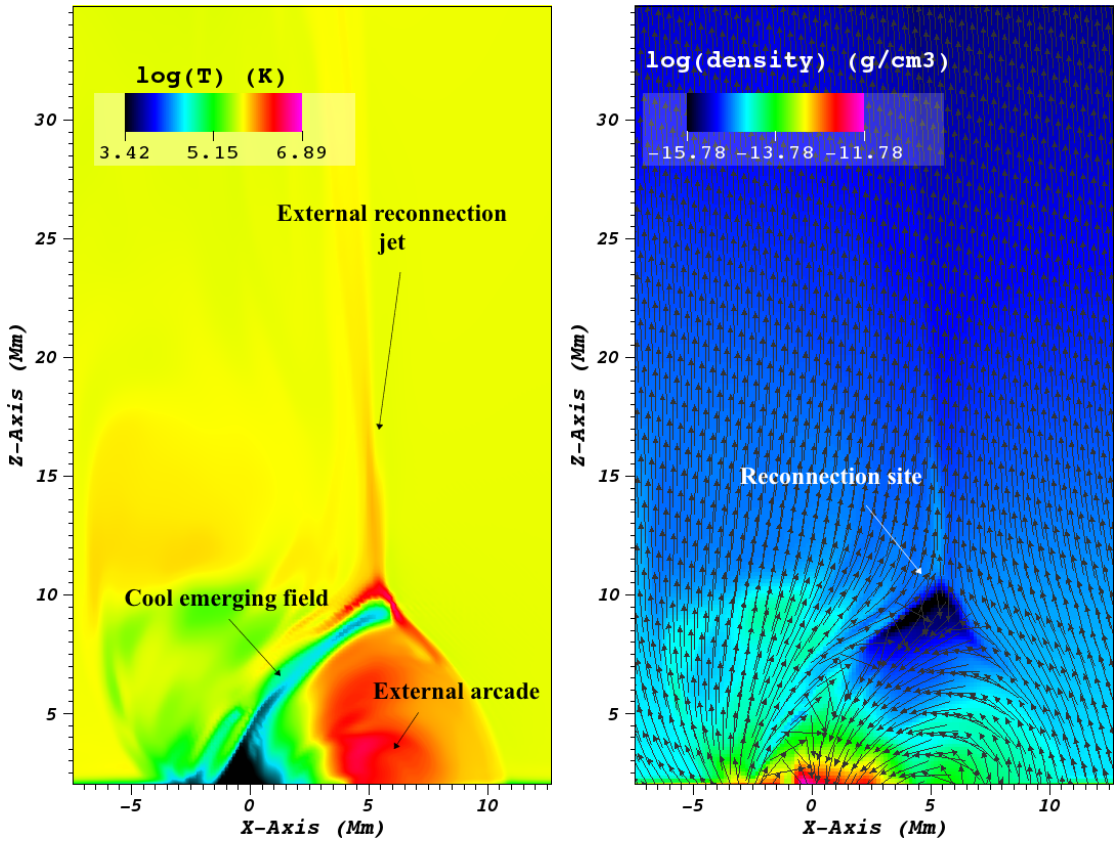

(a) Temperature distribution.

(b) Density distribution with the arrows corresponding to the projected magnetic field vectors.

Figure 5.6: Temperature and density distributions across the flux tube. The distribution is shown at $y \approx -2\,\mathrm{Mm}$ during the eruption, preceding the first "blowout" jet, at $t \approx 230.0\,\mathrm{min}$. Movies showing the temperature (movie2.mp4) and density (movie3.mp4) distribution in the $y - z$ direction are included in the attached CD.

post-eruption arcade is formed as a result of the internal reconnection underneath the erupting core, as shown in Figure 5.7a. The temperature within the internal arcade reaches up to 4×10^6 K. Along the jet channel, both hot and cool components are found, with temperatures around 1×10^6 K and 5×10^5 K respectively. By comparing Figure 5.7 and Figure 5.6, the jet channel during the eruption phase is also much wider than the jet channel prior to the eruption. This is also in agreement with recent observations of "blowout" jets (e.g. Moore et al., 2010).

Figure 5.8 shows the distribution of temperature and density at a late stage of the "blowout" jet emission (at $t \approx 237.1\,\mathrm{min}$). Comparing to Figure 5.7a, the jet channel in Figure 5.8a is much wider and the cool/hot material reaches large heights within corona. From Figure 5.8b, we find that dense plasma is also ejected within the jet's channel and it rises into the upper corona. This dense plasma comes from: a) the erupting field and b) from the interface between the rising and the pre-existing field.

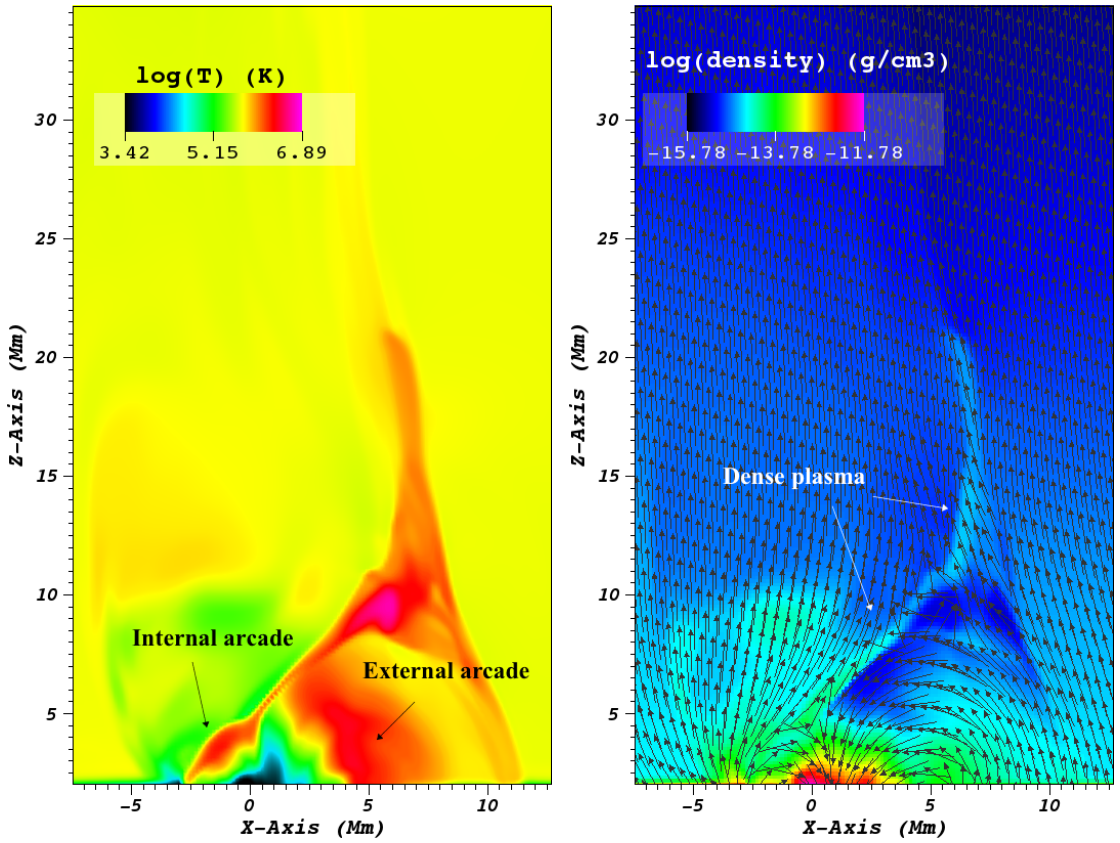

(a) Temperature distribution.

(b) Density distribution with the arrows corresponding to the projected magnetic field vectors.

Figure 5.7: Temperature and density distributions across the flux tube. The distribution is shown at $y \approx -2\,\mathrm{Mm}$ during the emission of the first “blowout” jet, at $t \approx 232.8\,\mathrm{min}$.

Figure 5.9 shows the magnetic field line topology during the emission of the eruption-driven “blowout” jet. Blue and red field lines are reconnected field lines, which join the emerging field with the ambient field. The white reconnected field lines form the post-eruption internal arcade. The yellow field lines have been traced from within the “blowout” jet. Both the erupting core and the “blowout” jet consist of twisted field lines. Initially, only the erupting field is twisted and the ambient field is non-twisted. The reconnection between the two fields leads to the relaxation of the twist. Eventually, the “blowout” jet experiences an untwisting motion due to this relaxation.

For a force-free non potential magnetic field, the twist, α, is derived from the following equation,

$$\nabla \times \mathbf{B} = \alpha \mathbf{B} \tag{5.9}$$

$$\alpha = \frac{\mathbf{j}}{\mathbf{B}}. \tag{5.10}$$

In this case, we consider the twist within the “blowout” jet to be $\alpha = |j_{\parallel}|/|\mathbf{B}|$, where $j_{\parallel}$ is the

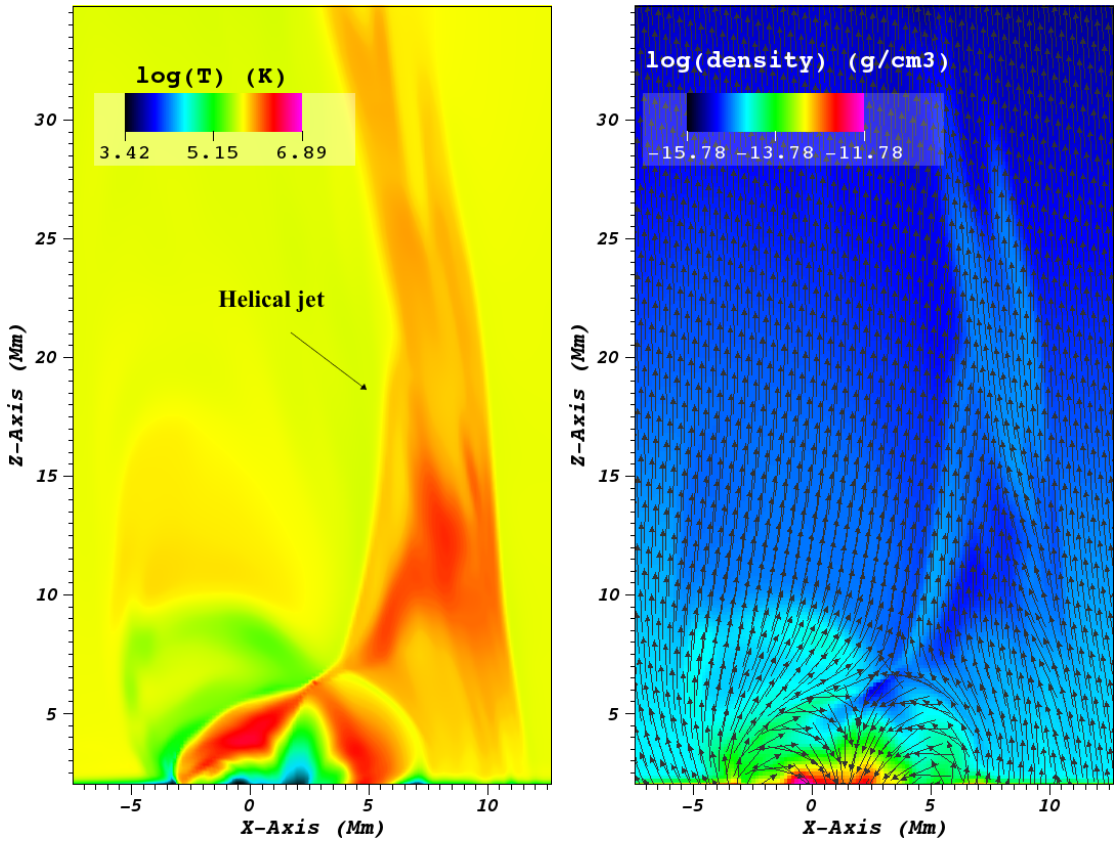

(a) Temperature distribution.

(b) Density distribution with the arrows corresponding to the projected magnetic field vectors.

Figure 5.8: Temperature and density distributions across the flux tube. The distribution is shown at $y \approx -2\,\mathrm{Mm}$ during the ending phase of the first "blowout" jet, at $t \approx 237.1\,\mathrm{min}$.

parallel component of the current along the reconnected field lines of the "blowout" jet. The temporal evolution of the average value of the twist along the jet channel (where $v_z > 0.0\,\mathrm{km\,s^{-1}}$ in a smaller domain chosen around the "blowout" jet) is then plotted in Figure 5.10a. This value is calculated at heights above $z \approx 9\,\mathrm{Mm}$, approximately where the interface between the envelope field and the "blowout" jet(s) is. We find that the average value of the twist increases over time until $t \approx 232.8\,\mathrm{min}$ due to the eruption of the twisted magnetic field. The decrease after $t \approx 232.8\,\mathrm{min}$ represents the untwisting motion of the "blowout" jet. Figure 5.10b shows the $|j_\parallel|/|\mathbf{B}|$ distribution at a time during the emission of the "blowout" jet ($x = 5.4\,\mathrm{Mm}$ and time $t \approx 233.4\,\mathrm{min}$). It is clear that the twist is high within the jet channel (i.e. $y \approx -12 \sim 0\,\mathrm{Mm}; z \approx 10 \sim 40\,\mathrm{Mm}$). High twist is also found underneath the jet, within the twisted emerging field that has a considerable transverse (B_x) component in its magnetic field (see also Figure 5.11b below).

Another way to show the untwisting motion of the jet is through plotting both the velocity and magnetic field transverse components. The transverse velocity, v_x, (Fig 5.11a) and transverse component of magnetic field, B_x, (Fig 5.11b) distribution at $x = 5.4\,\mathrm{Mm}$, $t \approx 233.4\,\mathrm{min}$ are

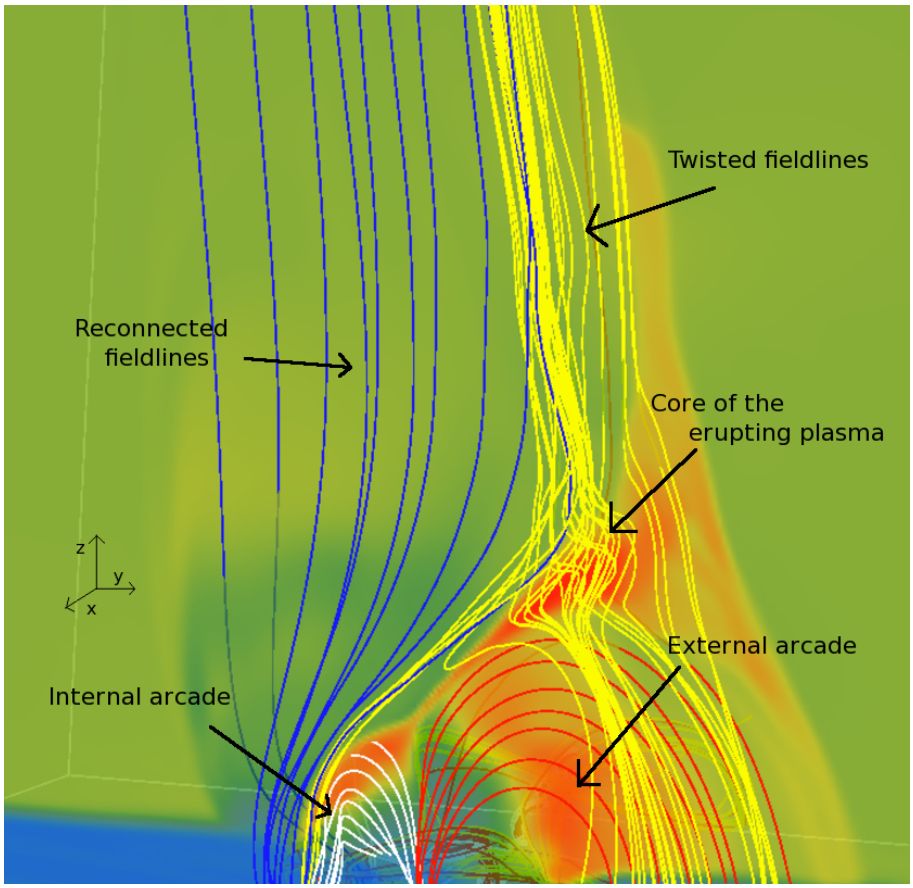

Figure 5.9: Visualization of the magnetic field lines at $t \approx 232.8\,\mathrm{min}$, during the emission of the first blowout jet. Magnetic field lines of the blowout jet (yellow), previously reconnected magnetic field lines with the ambient field (blue), internal arcade (white), and the external arcade (red).

plotted in Figure 5.11. The velocity component v_x is positive (pointing out of the plane) at the right-hand side of the jet, and negative (pointing into the plane) at the left-hand side of the jet. This implies that the flow is moving from right to left. However from Figure 5.11b, the transverse component of the magnetic field shows has a different (opposite) distribution: it is positive at the left-hand side of the jet and negative at the right-hand side. This reveals that the direction of the flow is opposite to the direction of the field lines, implying that the jet is moving perpendicular to the magnetic field.

In addition, we can show that the jet undergoes an untwisting motion by studying the current and vorticity distribution along the jet. The vorticity (ω) is defined as

$$\omega = \nabla \times \mathbf{v}. \tag{5.11}$$

Figure 5.12 shows the distribution of the product of $j_{\|}$ with the vorticity $\omega_{\|}$ at $x = 5.4\,\mathrm{Mm}$ and time $t \approx 233.4\,\mathrm{min}$. It is shown that within the jet channel, the product is mostly negative,

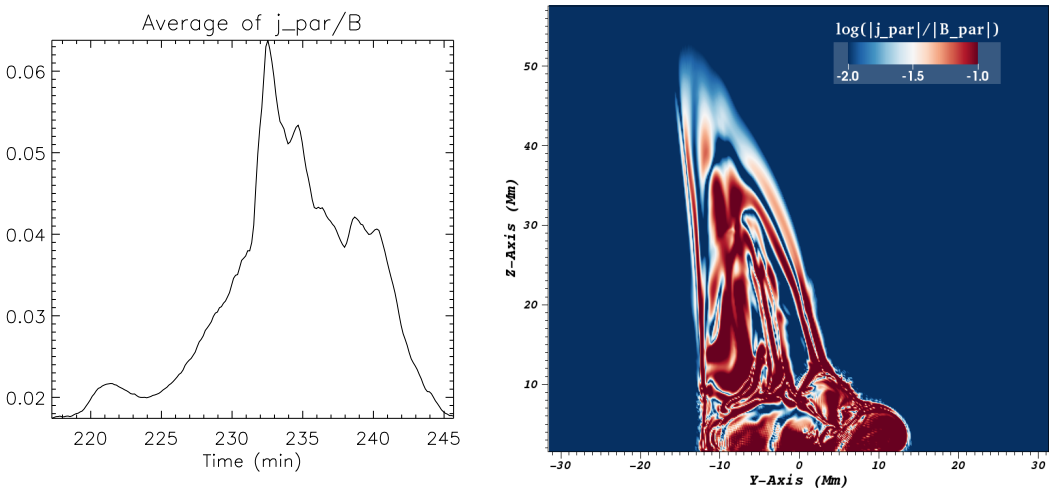

(a) (b)

Figure 5.10: (a) The temporal evolution of the average $|j_{\parallel}|/|\mathbf{B}|$ within the blowout jet. (b) The $|j_{\parallel}|/|\mathbf{B}|$ distribution at $x = 5.4\,\mathrm{Mm}$, $t \approx 233.4\,\mathrm{min}$.

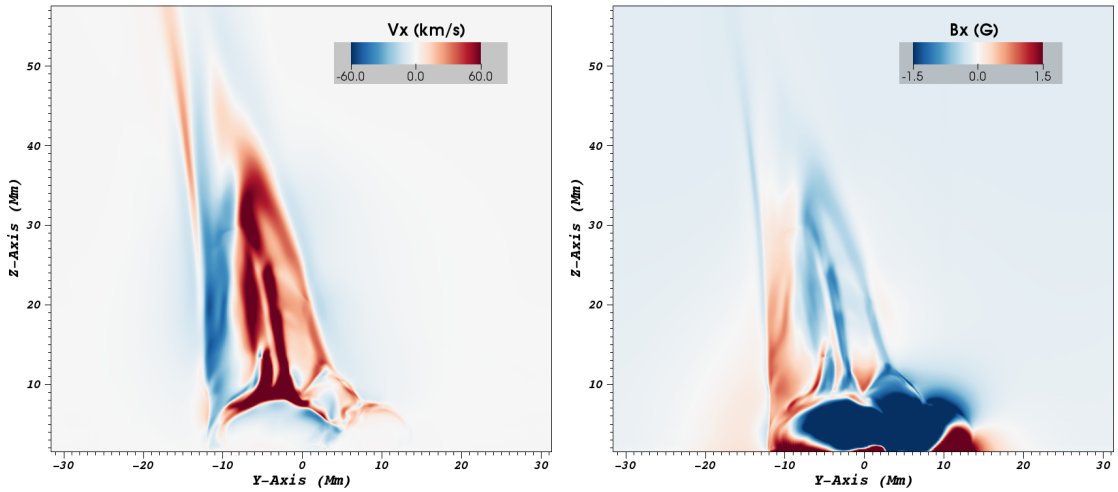

(a) v_x distribution. (b) B_x distribution.

Figure 5.11: v_x & B_x distribution along the jet at $x = 5.4\,\mathrm{Mm}$, $t \approx 233.4\,\mathrm{min}$.

implying that the current and vorticity are anti-parallel to each other, which is also a sign of untwisting motion.

It is obvious that in this simulation, the stored twist from the twisted erupting core is transported to the open reconnected field lines. Also, the direction of the untwisting motion is the same as the relative orientation between the erupting field and the open ambient field which reconnects. This suggests that the untwisting motion is more likely to be related to the propagation of twist along the reconnected field lines, not the twist itself. This is similar to the sweeping-magnetic-twist mechanism for the acceleration of solar jets proposed by Shibata and Uchida (1985).

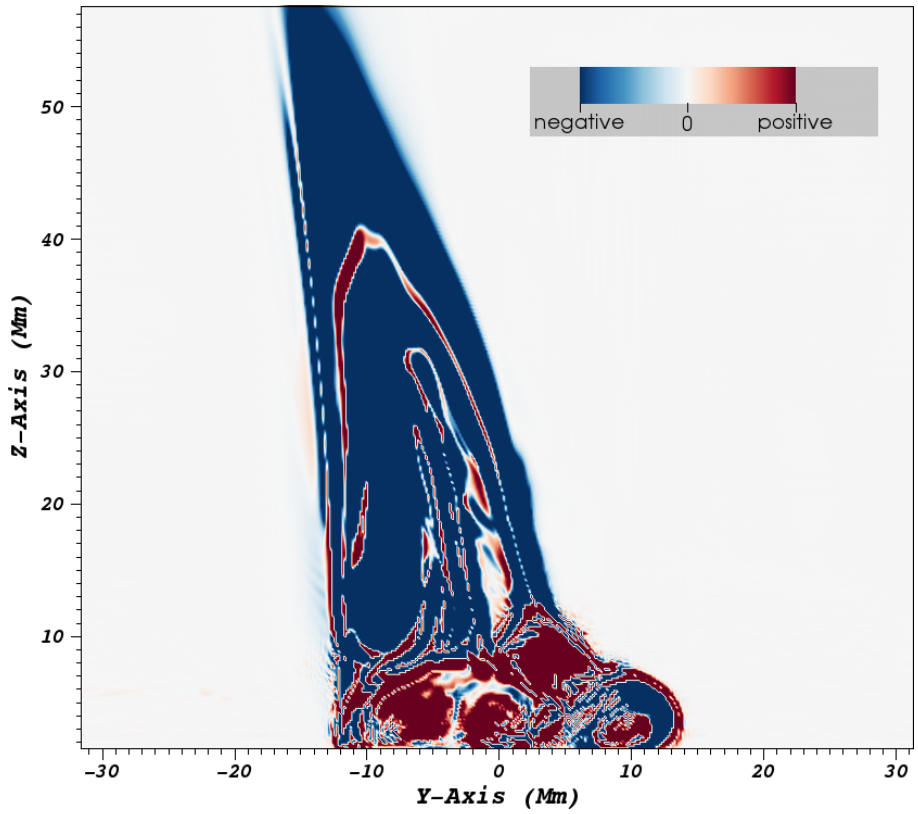

Figure 5.12: $j_{\parallel} \cdot \omega_{\parallel}$ distribution at $x = 5.4\,\mathrm{Mm}$, $t \approx 233.4\,\mathrm{min}$, where $j_{\parallel}$ and $\omega_{\parallel}$ is the current and vorticity components parallel to the reconnected field lines respectively.

5.4 Plasma Motion and Wave Propagation

To study the plasma motion of the jet, we calculate the quantity I_1 at various heights, given by

$$I_1 = \int \rho^2 \, \mathrm{d}y, \tag{5.12}$$

with a temperature range of $6.0 \times 10^5\,\mathrm{K} < T < 1.2 \times 10^6\,\mathrm{K}$. The quantity is calculated along height from $z \approx 12\,\mathrm{Mm}$ to $z \approx 27.5\,\mathrm{Mm}$ in every $150\,\mathrm{km}$, and along time. Figure 5.13a-c then shows the distance-time diagram of I_1 at three different selected heights, at $z = 17\,\mathrm{Mm}$, $z = 21.5\,\mathrm{Mm}$, and $z = 25\,\mathrm{Mm}$. Looking at the distance-time diagram along height, we find that there is a general movement of the plasma jet firstly moving towards the positive x direction, then to the negative x direction at later time, and then back towards the positive x direction again. This behaviour is found throughout all heights above the reconnection site, and hence indicates that the jet undergoes an oscillatory motion during its emission, and this oscillatory motion propagates from lower to higher heights. Similar results in the context of observations of helical jets, have been reported by Liu et al. (2009) and Schmieder et al. (2013). The transverse oscillation velocity amplitude of the jet in this case is found to be $\approx 7\,\mathrm{km\,s^{-1}}$.

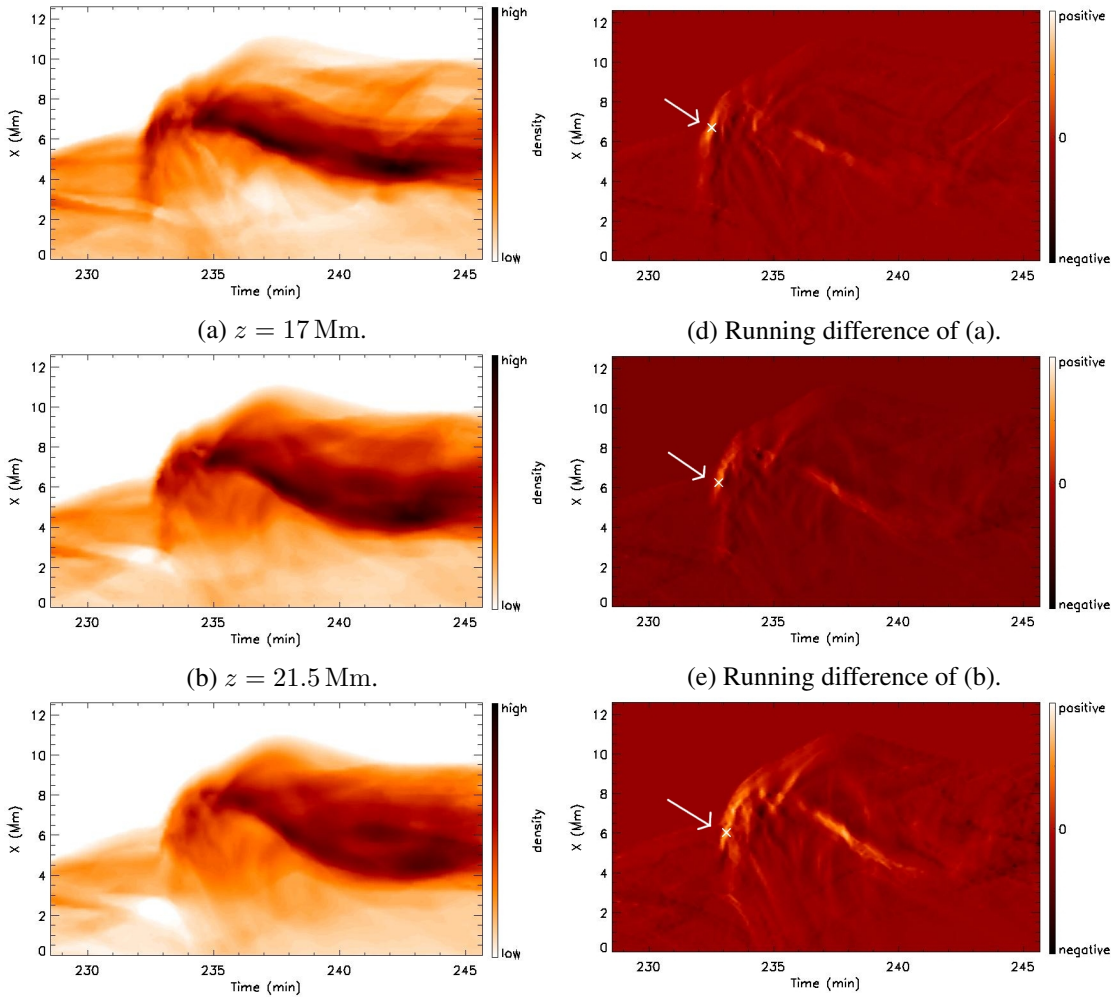

(a) $z = 17\,\mathrm{Mm}$.

(d) Running difference of (a).

(b) $z = 21.5\,\mathrm{Mm}$.

(e) Running difference of (b).

(c) $z = 25\,\mathrm{Mm}$.

(f) Running difference of (c).

Figure 5.13: (a-c): Distance-time diagram of $\int \rho^2 \, \mathrm{d}y$, for $6 \times 10^5\,\mathrm{K} < T < 1.2 \times 10^6\,\mathrm{K}$ across the jet at various height. (d-f): Running differences plot of (a-c).

In order to measure the velocity of the propagation, we plot the running difference diagrams for the distance-time diagram of I_1. Figure 5.13d-f shows the same heights as shown in Figure 5.13a-c. Then, we find the first (i.e. along time) local maximum in each running-difference plot along height. This would correspond to the first profound increment of the plasma density at that height, and this point is very likely to be located at the leading edge of the heavy plasma distribution along the jet.

By tracing this point along height, we obtain the height-time profile of the leading edge of the jet. The height-time profile is plotted in Figure 5.14a, and the propagation velocity is obtained by taking the first order differentiation of the height-time profile. The propagation velocity is plotted as the solid line in Figure 5.14b, whereas the dashed line is the local Alfvén speed in the close vicinity of the front of the propagating plasma. Since the method, which we use to obtain

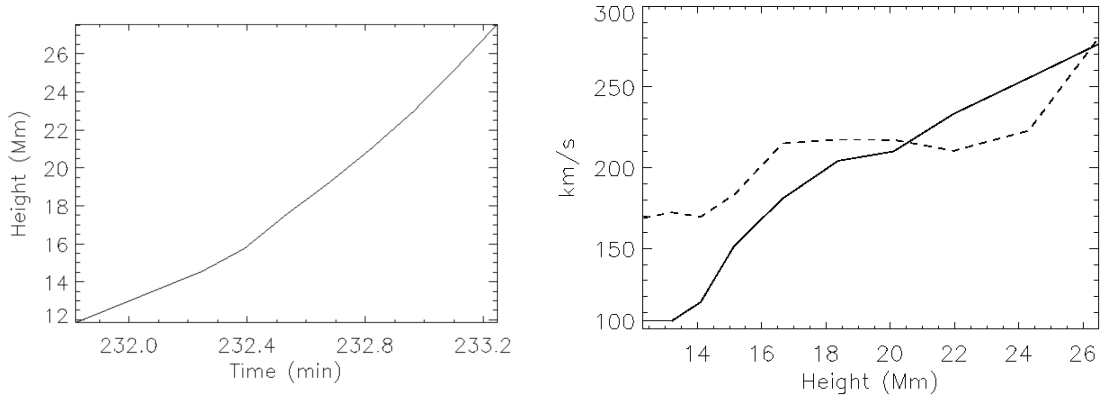

(a) (b)

Figure 5.14: (a) Height-time profile of the jet's upfront. (b) (Solid): Velocity of the feature's propagation speed. (Dashed): local Alfvén speed in the close vicinity of the front of the wave.

the height-time profile, is not as accurate as e.g. a Lagrangian tracer routine that can provide the position of the *same* plasma element over time, it is likely that we introduce an error in both lines in Figure 5.14b. However, we believe that this error is small and, thus, the results do not change dramatically. As such, Figure 5.14b shows that the propagation velocity is comparable to the local Alfvén speed. This together with the fact that the "blowout" jet undergoes an untwisting motion suggest that we are witnessing the propagation of a torsional Alfvén wave during the untwisting motion of the "blowout" jet.

5.5 Discussion

In this chapter, we presented results from a numerical simulation of magnetic flux emergence into a magnetized corona. We used the same magnetic flux tube configuration as in the simulation in Chapter 4. In both experiments, a quadrupolar region is formed at the photosphere following the emergence of the sub-photospheric magnetic flux tube. The activity (e.g. in the form of eruptions and jets) in a quadrupolar region has not been studied (and more importantly, it has not been shown) in detail, in previous simulations with similar initial conditions. Our aim was to show whether and how a quadrupolar region, which is formed naturally after the emergence of magnetic flux, can lead to intense magnetic activity.

In our experiment, we have confirmed that in the presence of the pre-existing magnetic field in the corona, the emerging field reconnects with the pre-existing field, which leads to the emission of EUV/X-Ray jets. Moreover, the reconnection between the emerging and ambient field releases the downward tension of the overlying (envelope) field, causing eruptions of sheared field lines into the solar corona. These eruptions drive the onset of ejective "blowout" jets. To some extent, this

result is similar to what has been reported in other simulations (e.g. Archontis and Hood, 2013; Moreno-Insertis and Galsgaard, 2013, etc.). However, there is an important difference between the experiments presented here and the existing simulations in the literature. The eruptions in our simulations originate mainly from the PIL along the inner polarity (P1 & N2) of the quadrupolar region, not from the PIL along P1 & N1 or P2 & N2. This indicates that the shearing and reconnection between approaching opposite polarities that belong to different bipoles can indeed lead to ejective eruptions (and flaring of the plasma underneath the erupting fields). Also, we find that in the quadrupolar region, the eruptions can also be triggered within each separate bipolar field (from the PIL along P1 & N1 and P2 & N2). Therefore, our numerical simulations reveal that more eruptions are likely to occur in quadrupolar regions (compared to simple / single bipolar regions). In both cases (quadrupolar and bipolar fields), recurrent eruptions have been reported to occur. The exact reason for the recurrence of ejective eruptions has not been studied in detail yet. It is likely that the repeated emission of plasma is closely associated with the continuous shearing and reconnection of the field along strong polarity inversion lines. In both cases, the continuous process of shearing and reconnection is basically driven by flux emergence. If the emergence stops, then the formation of flux ropes (that will eventually erupt) is very likely to stop too.

The coronal response to the ejective eruptions of the sheared fields has been mainly studied by examining the transfer of energy and flux into the solar atmosphere. We have found that this transfer happens along the channel of "blowout" jets. These jets are found to undergo an untwisting motion due to the relaxation of the twist through the reconnection between the twisted field lines of the erupting core and the non-twisted pre-existing field. We also showed in more detail compared to previous simulations that the "blowout" jets undergo an oscillatory motion at different heights across the solar atmosphere during their emission. It seems that this oscillatory motion propagates from lower to larger heights. The propagation velocity is found to be comparable to the local Alfvén speed. This suggests that there is a propagation of a torsional Alfvén wave during the untwisting motion of the "blowout" jet. The propagation of such waves along the emission of "blowout" jets, in the context of magnetic flux emergence that form a quadrupolar region, has not been shown in detail before.

Chapter 6

Parametric Study: The Effect of Ambient Field Strength on Jets

In this chapter, we examine how an ambient coronal magnetic field affects the dynamics of the simulated EFR and the onset of jets. We use the same numerical setup as in the previous chapter(s) but we vary the amplitude of the coronal field strength. We have performed three experiments where the coronal field strength $bcor$ is varied such as: (a) $bcor = 3\,\mathrm{G}$, (b) $bcor = 6\,\mathrm{G}$, (c) $bcor = 10\,\mathrm{G}$. We also use an anomalous resistivity (instead of uniform) above the photosphere in these three simulations. The reason for using anomalous resistivity is twofold: firstly we wanted to compare (as much as we could) the results of the two experiments (uniform versus anomalous resistivity experiments) and secondly, because we wanted to use a more realistic resistivity profile since one should not expect that the resistivity in the Sun is uniform within fields with steep gradients (e.g. current layers). In our simulations, the resistivity (η) above the photosphere varies according to the local current, and has the following form,

$$\eta = \begin{cases} \eta_{bg} + \eta_0 \left(\dfrac{|\mathbf{j}|}{j_{\mathrm{crit}}} - 1 \right), & \text{if } |\mathbf{j}| \geq j_{\mathrm{crit}}; \\ \eta_{bg}, & \text{if } |\mathbf{j}| \leq j_{\mathrm{crit}}. \end{cases} \tag{6.1}$$

where $\eta_{bg} = 0.01$ is the background uniform resistivity coefficient, $\eta_0 = 0.05$ is the anomalous resistivity coefficient, and $j_{\mathrm{crit}} = 0.015$ is the critical value of the local current density. To choose the value of j_{crit}, we first performed experiments with uniform resistivity (for all $bcor = 3,\ 6,\ 10\,\mathrm{G}$ cases) and we estimated the resistivity at the local maxima of the strong current sheets (around the region of the formation of the erupting field). The j_{crit} is a bit smaller than that value. Thus, we focused dissipation in regions with strong field gradients.

6.1 $3\,\mathrm{G}$ case

In this simulation, we obtain very similar results to the experiment with uniform resistivity, which was presented in Chapter 5. For instance, we still find recurrent eruptions to occur within the EFR, and most of these eruptions originate from the PIL between the inner polarities. We do find some differences between the two cases, by looking at the temporal evolution of the velocity of the jets (see Fig 5.4 and Fig 6.1). One difference is that the eruptions in the anomalous resistivity case generally occur at a slightly earlier time (e.g. the first eruption in the uniform resistivity simulation occurs at $t \sim 232.82\,\mathrm{min}$ where in the anomalous resistivity case occurs at $t \sim 230.0\,\mathrm{min}$). However, in both cases, the jets travel at roughly the same speed and bring a similar amount of density and flux into the outer solar atmosphere.

The initial evolution of the system is similar in both cases. The emerging field reaches the photosphere at $t = 160.0\,\mathrm{min}$, forming two bipolar regions at the base of the photosphere. Eventually, the emerging field becomes strong enough to rise above the photosphere, forming two magnetic lobes that are anchored at the photospheric bipolar regions.

6.1.1 Flows and Eruptions

The emergence of the field and its interaction (e.g. reconnection) with the ambient magnetized atmosphere leads to the onset of jets. Figure 6.1 shows the temporal evolution of the maximum up-flow (black) & down-flow (red) velocities above the photosphere. Note that at $t = 160\,\mathrm{min}$, an up-flow of $v_z \approx 20\,\mathrm{km\,s^{-1}}$ is first seen, without any significant down-flow. This corresponds to the emergence of the flux tube into the photosphere. Just after the emergence, at around $t = 164\,\mathrm{min}$, the envelope magnetic field lines from each emerging lobe start to reconnect with the pre-existing field, resulting in bidirectional reconnection jets, which are emitted from the apex of the emerging lobes. The maximum upward velocity of the first jets reaches values up to $120\,\mathrm{km\,s^{-1}}$, and maximum temperature around $1 \times 10^6\,\mathrm{K}$.

Figure 6.1 shows that the emission of jets is recurrent. As we discussed in the previous chapter, the reconnection between the emerging and ambient fields triggers a series of bidirectional flows, which is illustrated by the good correlation between the maximum and minimum values of the vertical velocity above the solar surface. In the present case, we find that there are at least 6 major "events", during which the vertical velocity increases/decreases episodically to reach a maximum/minimum and then drops again to minimal values (around zero). For instance, the first "event" starts at around $t = 164\,\mathrm{min}$ and ends at around $t = 175\,\mathrm{min}$, the second "event" starts at around $t = 178\,\mathrm{min}$ and ends at around $t = 200\,\mathrm{min}$, etc.. Overall, 6 major "events" are found. The first two are the result of "standard" reconnection jets, and the following four are the result of eruption driven ("blowout") jets.

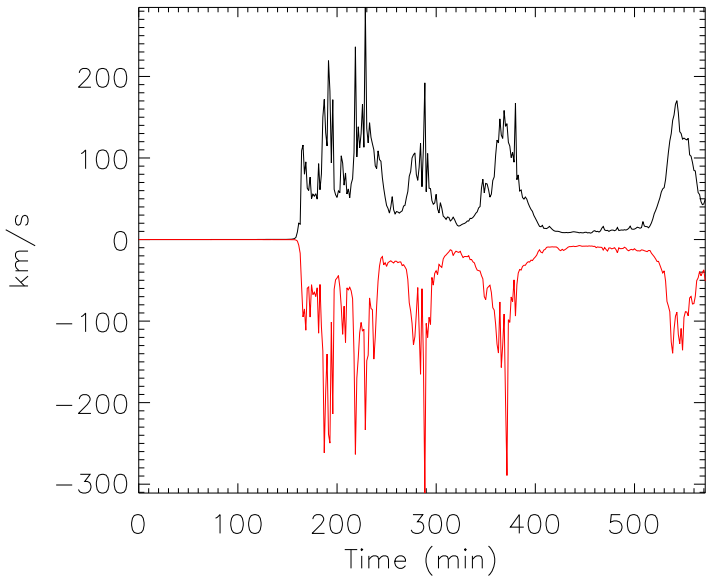

Figure 6.1: Temporal evolution of maximum (black) & minimum (red) vertical velocity above the photosphere in the simulated EFR.

In a similar manner to the previous chapter (see Fig 5.5), Figure 6.2 shows the running difference of the variable $\int \rho^2 \, \mathrm{d}x \, \mathrm{d}y$, which represents the integrated plasma density with temperature greater than 8×10^5 K. This would give us information of significant dense & heated plasma being transported into the higher corona. Different colours in the figure represent an increase (white) or decrease (black) of plasma compared to the previous time step. Combining Fig 6.1 & Fig 6.2, we find whether the upward jets transport dense plasma to large heights. We find three profound peaks in Figure 6.2 and one that is not so marked (at time between $280\,\mathrm{min}$ and $290\,\mathrm{min}$). These events happen at the same time with the events that correspond to "blowout" jets in Figure 6.1. This suggest that eruption-driven jets can transport very heavy plasma from the low atmosphere (chromosphere/transition region) into the corona.

The second event seen in Fig 6.1 at $t \sim 186\,\mathrm{min}$ represents a reconnection jet which is ejected from the left bipole. This jet is triggered by reconnection between the magnetic field lines at the middle of the two lobes and the ambient field. Then the plasma is pushed along the field lines of the left bipole and ejected upwards. Another reconnection jet is ejected from the same area at $t \sim 205\,\mathrm{min}$ by the same mechanism. These jets are not shown in Fig 6.2, suggesting that they do not carry very dense plasma into the outer atmosphere.

As we showed in Chapter 4, this quadrupolar region is capable of producing magnetic flux ropes that can erupt. Indeed, we find that there are four eruptions of magnetic flux ropes, which lead to the onset of "blowout" jets. In Figure 6.2, the four eruptions are indicated by the four

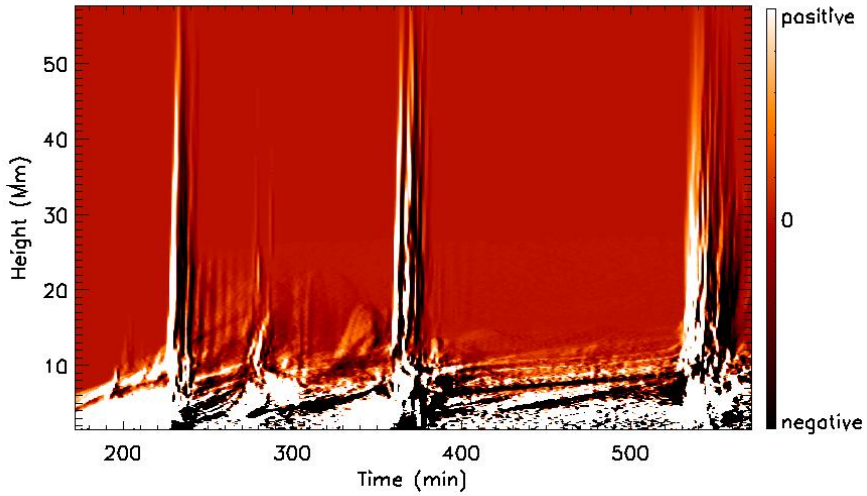

Figure 6.2: Height-time diagram of running difference plot for $\int \rho^2 \, \mathrm{d}x\mathrm{d}y$, where $T > 8 \times 10^5$ K.

peaks at the height-time diagram of the running difference plot for density. They occur at times: $t \sim 217\,\mathrm{min}$, $t \sim 274\,\mathrm{min}$, $t \sim 357\,\mathrm{min}$ and $t \sim 571\,\mathrm{min}$. The second eruption is a 'failed' eruption and that is why the positive difference in the plot (coloured by white) does not reach large heights. The other three eruptions are fully ejective (i.e. they leave the domain).

6.1.2 Location of Eruptions and Jets

One interesting question to answer is: where do these eruptions come from? Figure 6.3 shows the magnetogram at the base of the photosphere during the four eruptions. The local maximum of the upflow around the origin of the erupting material is marked by the red asterisk symbol, whereas the local maximum of the downflow is marked by the yellow asterisk symbol. This is to trace the origin of the eruption (i.e. where the flux rope is initially formed). Indeed, the local extrema of the vertical velocity occur in the current sheet, underneath the erupting field and, thus, they indicate an approximate area of where the eruptions take off. Figure 6.3a-c shows that the first three eruptions originate from the PIL between the two bipoles, most likely due to the shearing motion between P1 & N2 and the internal reconnection of the sheared field lines. The fourth eruption, shown in Figure 6.3d, is ejected from within the bipolar region BR1. This is due to the shearing and reconnection along the PIL of the BR1, a process that has been repeatedly found to occur in many similar experiments (e.g. Manchester et al., 2004; Archontis and Török, 2008; Archontis and Hood, 2010).

We can also use the large (positive and negative) values of v_z to get a proxy of where the jets are triggered and how the fast outflows move in space. The positions of the extrema of v_z during

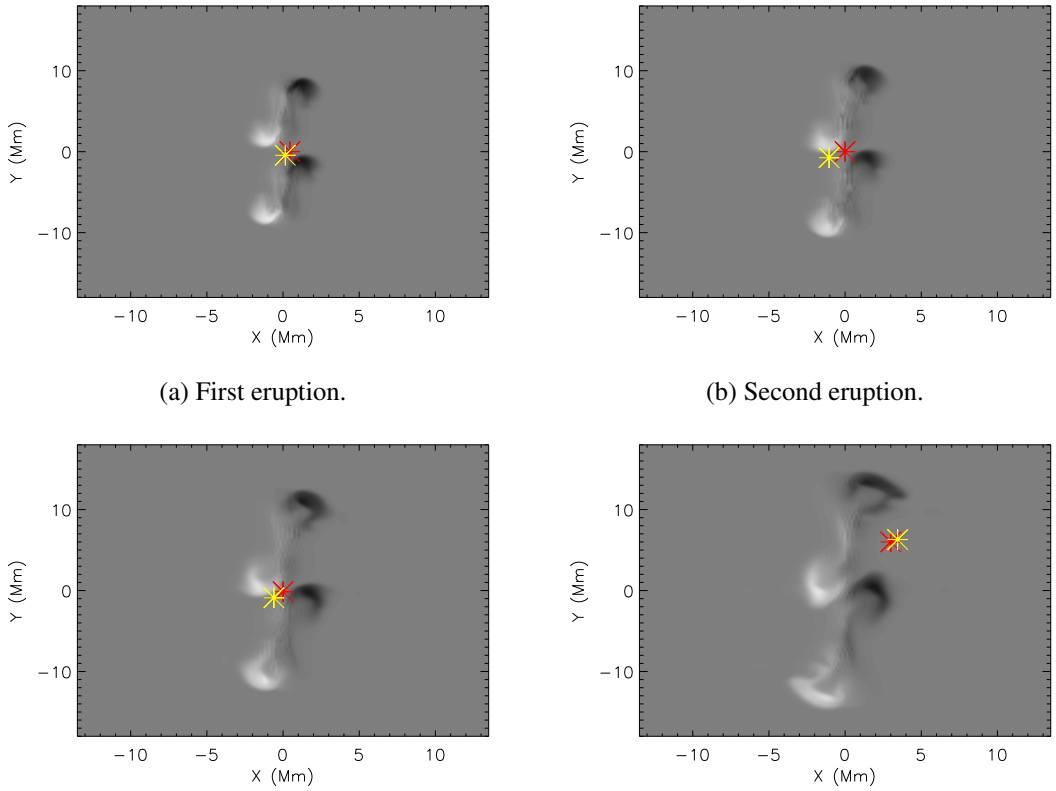

(a) First eruption.

(b) Second eruption.

(c) Third eruption.

(d) Fourth eruption.

Figure 6.3: The magnetogram plotted at the base of photosphere during the onset of the four eruptions. The red (yellow) asterisk symbol denotes the position of the local maximum (minimum) v_z around the origin of the eruption at each time.

the four eruptions are traced and plotted in Figure 6.4. Figure 6.4a & 6.4c show the location of the maximum v_z in the domain, and Figure 6.4b & 6.4d show the location of the minimum v_z. Different colours in the plot corresponds to different eruptions. The black symbols correspond to the first eruption, red to the second eruption, green to the third eruption and blue to the fourth eruption. Flows with $|v_z| \geq 70\,\mathrm{km\,s^{-1}}$ are marked as a '$*$' sign, and $|v_z| \geq 150\,\mathrm{km\,s^{-1}}$ are marked as a '$+$' sign. This shows that most of the maximum upflows and downflows occur at a height of $z \approx 8.1\,\mathrm{Mm}$. This is the reconnection site, at the top of the emerging magnetic fields, where a current sheet is built up after the emerging and ambient field come into contact. The upflows show a wider distribution. This is because when a "blowout" jet is ejected, the twisting erupting core triggers reconnection with the pre-existing magnetic fields at successively larger heights. Thus, we find that large values of v_z exist at many heights within the solar atmosphere. The only exception is the second eruption, which is a 'failed' eruption, which triggers a standard reconnection jet at small heights. That is the reason that we do not find red symbols at large heights in Figure 6.4.

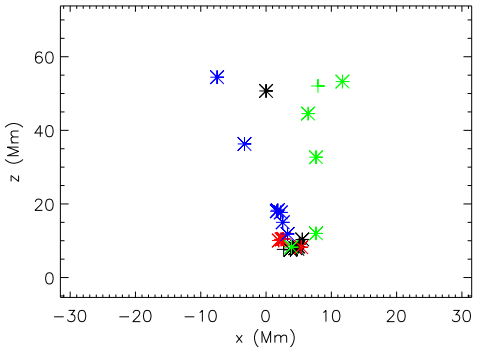

(a) Locations of Maximum v_z in xz plane.

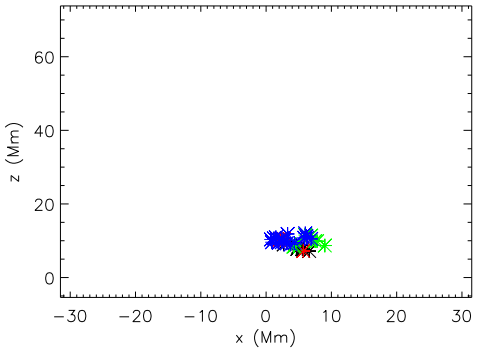

(b) Locations of Minimum v_z in xz plane.

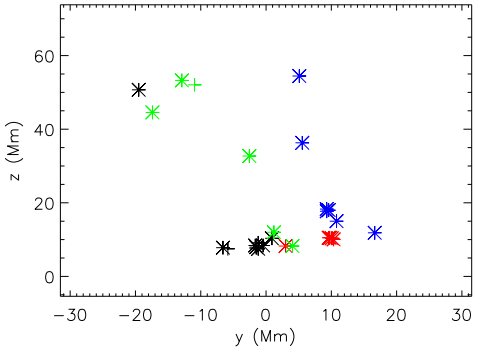

(c) Locations of Maximum v_z in yz plane.

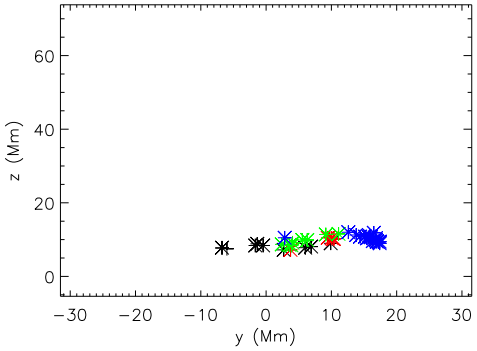

(d) Locations of Minimum v_z in yz plane.

Figure 6.4: Location of maximum v_z (a,c); minimum v_z (b,d) during the four eruptions in the $x-z$ (a,b) and $y-z$ (c,d) plane. '+' indicates $|v_z| \geq 150\,\mathrm{km\,s^{-1}}$. '$*$' indicates $|v_z| \geq 70\,\mathrm{km\,s^{-1}}$. The different colours correspond to different eruptions. black - first eruption, red - second eruption, green - third eruption, blue - fourth eruption.

6.1.3 Energy, Helicity and Poynting Flux

Figure 6.5 shows the temporal evolution of the magnetic (black) & kinetic (red) energy in the corona. The kinetic energy increases whenever a jet is emitted into the corona. The first small peak at $t = 161\,\mathrm{min}$ corresponds to the emergence of the flux tube and the emission of the first reconnection jet(s). During the evolution, the overall increase of the magnetic energy in the corona is due to: (i) flux emergence and (ii) jets being transported into the outer solar atmosphere. The figure shows good correlation between the drop of magnetic energy and the increase of kinetic energy during the eruptions. The difference in the loss-gain relation between the magnetic & kinetic energy indicates that most of the magnetic energy is converted into heat via Joule dissipation due to reconnection.

The temporal evolution of the helicity of the whole system in the solar atmosphere is shown in Figure 6.6, where the solid line represents the total helicity, dashed line the mutual helicity and

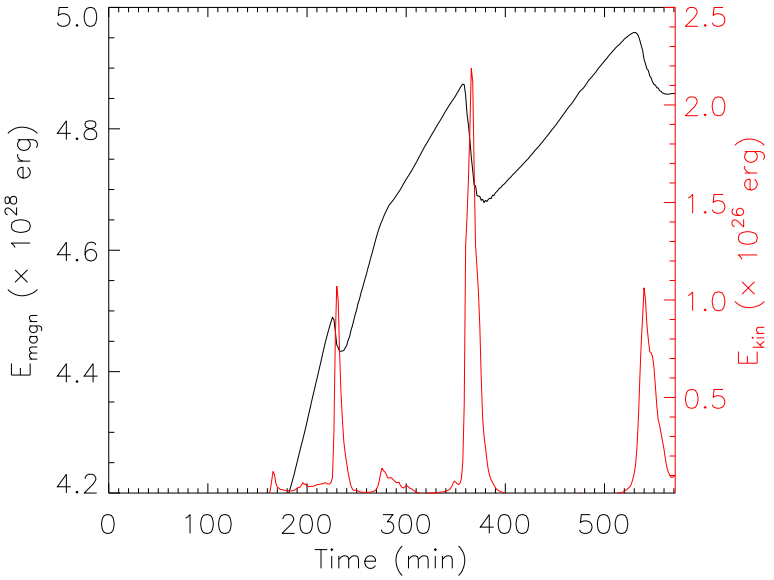

Figure 6.5: Temporal evolution of magnetic energy (black) & kinetic energy (red) above corona in $B_{amb} = 3\,\mathrm{G}$ case.

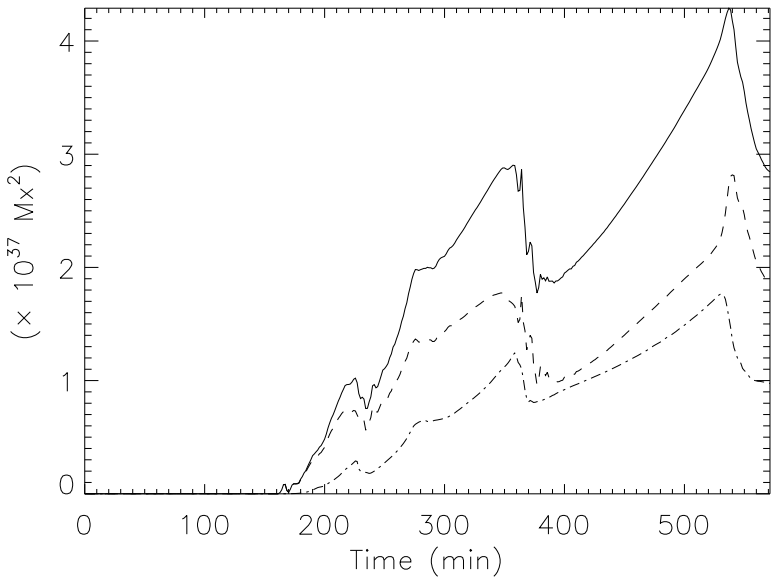

Figure 6.6: Temporal evolution of total helicity (solid line), mutual helicity (dashed line), and self helicity (dot-dashed line). The increase in the helicity matches the time where we have eruption, and the decrease in the helicity corresponds to the jets leaving the numerical domain.

dot-dashed line the self helicity. The self helicity is measured as the helicity of the ambient field, and mutual helicity is the interaction between the emerging flux tube and the ambient field. The

total helicity here is simply the sum of both the self & mutual helicity.

The self helicity is given by

$$H_{\mathrm{self}} = \int_V (\mathbf{A} - \mathbf{A}_p) \cdot (\mathbf{B} - \mathbf{B}_p)\,\mathrm{d}V, \tag{6.2}$$

and the mutual helicity is given by

$$H_{\mathrm{mutual}} = 2\int_V \mathbf{A}_p \cdot (\mathbf{B} - \mathbf{B}_p)\,\mathrm{d}V. \tag{6.3}$$

In both Eq 6.2 and Eq 6.3, V represents the integration volume, $\mathbf{B}$ is the magnetic field, and $\mathbf{B}_p$ the potential field. $\mathbf{A}$ and $\mathbf{A}_p$ are the generating vector potentials of the magnetic fields $\mathbf{B}$ and $\mathbf{B}_p$.

The calculation methods that we are using are the same methods used by Moraitis et al. (2014). We find that there is a good temporal correlation between the increase of helicity and the eruption timing, which indicates that the ambient field gains twist from the erupting field through magnetic reconnection. The helicity then decreases while the jet leaves the numerical domain.

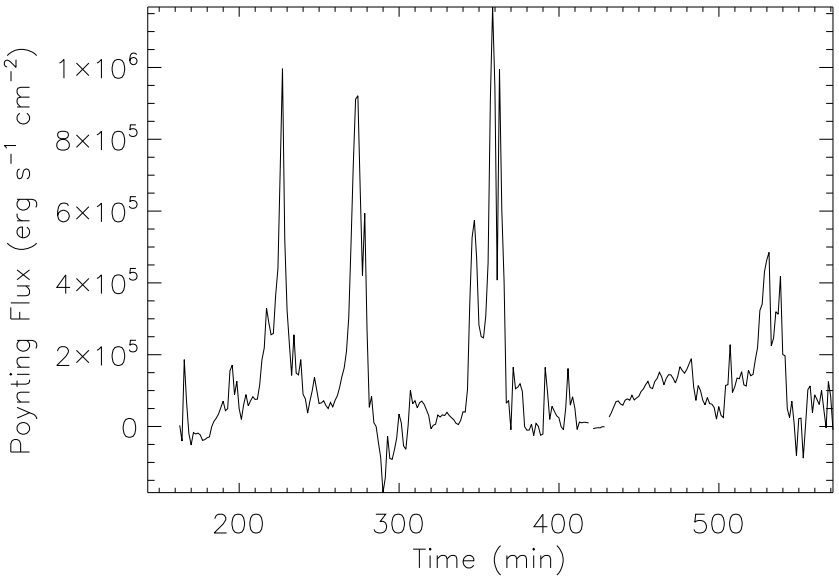

Figure 6.7: Temporal evolution of Poynting flux at a horizontal cut above the magnetic lobes.

Figure 6.7 shows the temporal evolution of the Poynting flux along the jet channels, which are typically formed above the magnetic lobe(s). We measure the flux that crosses the horizontal cut at $z = 8.1\,\mathrm{Mm}$. The Poynting flux is calculated as

$$\frac{c}{4\pi}\int_{z=90} \mathbf{E} \times \mathbf{B}\,\mathrm{d}x\mathrm{d}y, \qquad \text{for} \quad |v_z| > 5.0\,\mathrm{km\,s^{-1}}, \tag{6.4}$$

where c, $\mathbf{E}$ and $\mathbf{B}$ are the speed of light, electric field and magnetic field respectively. This corresponds to the Poynting flux carried by the jets. The Poynting flux increases significantly during the eruptions, reaching up to $1 \times 10^6\,\mathrm{erg\,cm^{-2}\,s^{-1}}$. This indicates that the amount of Poynting flux, which is transported into the corona during the "blowout" jet ejections, can contribute to the driving of the solar wind.

6.1.4 Detailed Study of an Eruption Driven "Blowout" Jet

In the following, we study the onset and evolution of one of the ejective eruptions in more detail.

Onset and Evolution: 2D Analysis

In Figure 6.8, Figure 6.9 and Figure 6.10 we show the temperature, density, and vertical velocity v_z distribution across the flux tube at various times during the third eruption. The overplotted arrows in Fig 6.9 represent the projected (full) magnetic field vector onto the plane. Fig 6.8a & Fig 6.9a show the distribution at time $t = 357.08\,\mathrm{min}$, just after the onset of the eruption. The core of the erupting material (flux rope) consists of cool chromospheric/transition region material (in dark blue/green colour). The erupting core moves towards the right side of the system (from $x = 0$ to $x = 10\,\mathrm{Mm}$) as it rises. The hot (red) loop-like structure that is located between $x = 3$ and $x = 12\,\mathrm{Mm}$ is the external flare arcade, which is formed due to reconnection between the emerging and the ambient field. The erupting core reaches the top of the external arcade and it pushes the ambient field towards the x-direction. This motion forms a current sheet at the interface between the erupting material and the pre-existing field. Reconnection occurs at the current sheet, which powers the ejection of the hot (max $T \sim 1.5 \times 10^6\,\mathrm{K}$) & fast (max $v_z \sim 40\,\mathrm{km\,s^{-1}}$) external reconnection jet seen in Fig 6.10a. Following the external reconnection between the envelope field and the ambient field, some of the heated plasma is ejected downwards following the reconnected field lines.This leads to an apparent expansion of the external hot arcade (max $T \sim 4.8 \times 10^6\,\mathrm{K}$). As the erupting core continues to rise, it forces more reconnection at the current sheet and causes the emission of another (faster) jet (max $v_z \sim 70\,\mathrm{km\,s^{-1}}$).

The twisted field continues to erupt and at time $t = 359.54\,\mathrm{min}$ it starts to be ejected along the reconnected ambient field lines (Fig 6.8c & Fig 6.9c). The velocity of the outflow increases and it reaches a maximum velocity of $v_z \sim 105\,\mathrm{km\,s^{-1}}$. As seen in Fig 6.10c, the jet channel is widened after the eruption of the flux rope. Also, after the eruption, at time $t = 361.37\,\mathrm{min}$, as the erupting core reaches larger heights, the twisted field lines underneath the erupting field start to come together and reconnect in a tether-cutting manner. This is described as 'internal' reconnection, as opposed to the 'external' reconnection between the envelope field and the ambient field. The internal reconnection results in the formation of a hot arcade near the origin of the eruption. The

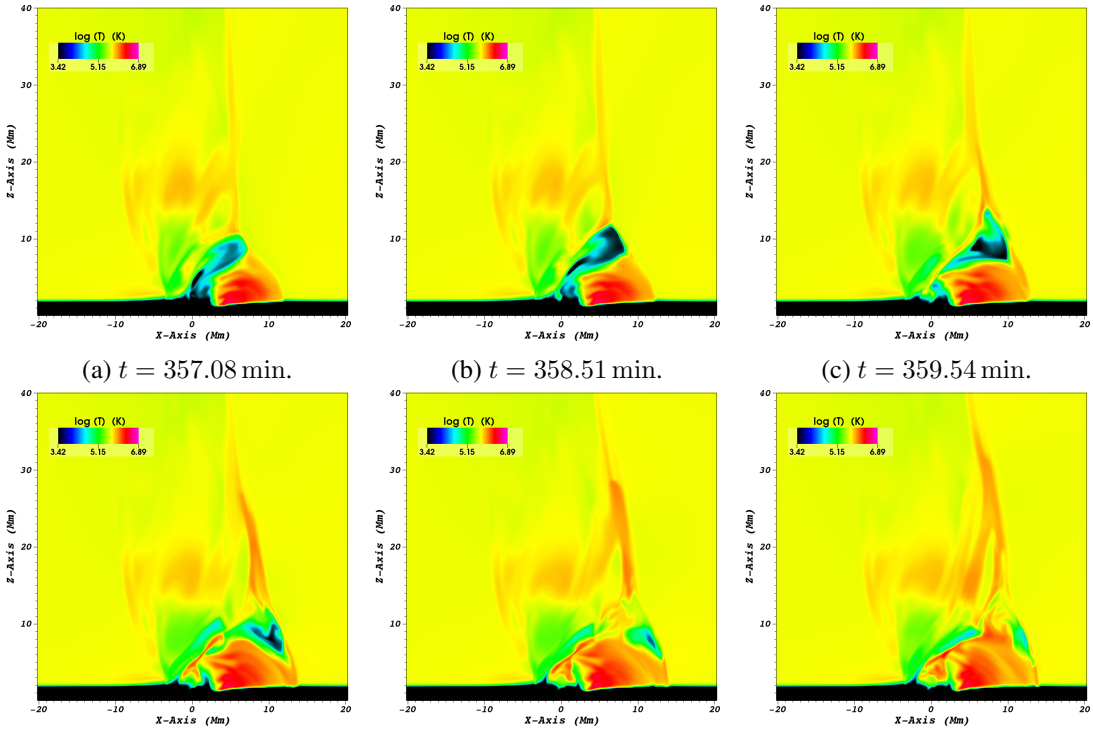

(a) $t = 357.08\,\mathrm{min}$. (b) $t = 358.51\,\mathrm{min}$. (c) $t = 359.54\,\mathrm{min}$.

(d) $t = 361.37\,\mathrm{min}$. (e) $t = 362.80\,\mathrm{min}$. (f) $t = 364.23\,\mathrm{min}$.

Figure 6.8: Temperature distribution during the third eruption across the flux tube, at $y = -4.5\,\mathrm{Mm}$. The animated version of this figure is included in the attached CD (movie4.mp4).

top of the post-eruption arcade is visible at $x = 0\,\mathrm{Mm}$ and $z = 4\,\mathrm{Mm}$ (Fig 6.8d). Above the arcade, there is hot material which is ejected sideways and it pushes the erupting core towards the ambient corona. This hot material is the upward-released jet that is triggered due to internal reconnection.

Figure 6.9d shows that the external reconnection leads to the emission of hot material that is also dense. This dense material is ejected along the channel of the jet, towards the outer solar atmosphere. Fig 6.8e and 6.8f show the temperature distribution at a later stage, revealing that the upward jet (after the eruption) is multi-thermal. It consists of cool and hot plasma. The cool component comes from the core of the erupting flux rope and the hot component of the external reconnection. Thus, the thermal distribution of the resulting "blowout" jet is more complex than in a standard reconnection jet. Also the evolution of the temperature distribution shows that some of the cool erupting plasma is not ejected along the jet channel but it moves downwards, along the side of the external arcade. The temporal/spatial evolution of density (Fig 6.9e & 6.9f) shows that a considerable amount of heavy plasma is transported to the outer atmosphere by the "blowout" jet.

During the eruption of the flux rope, the twisted field lines from the flux tube reconnect with the untwisted ambient field lines, which then relaxes the twist (Chapter 5). This leads to the

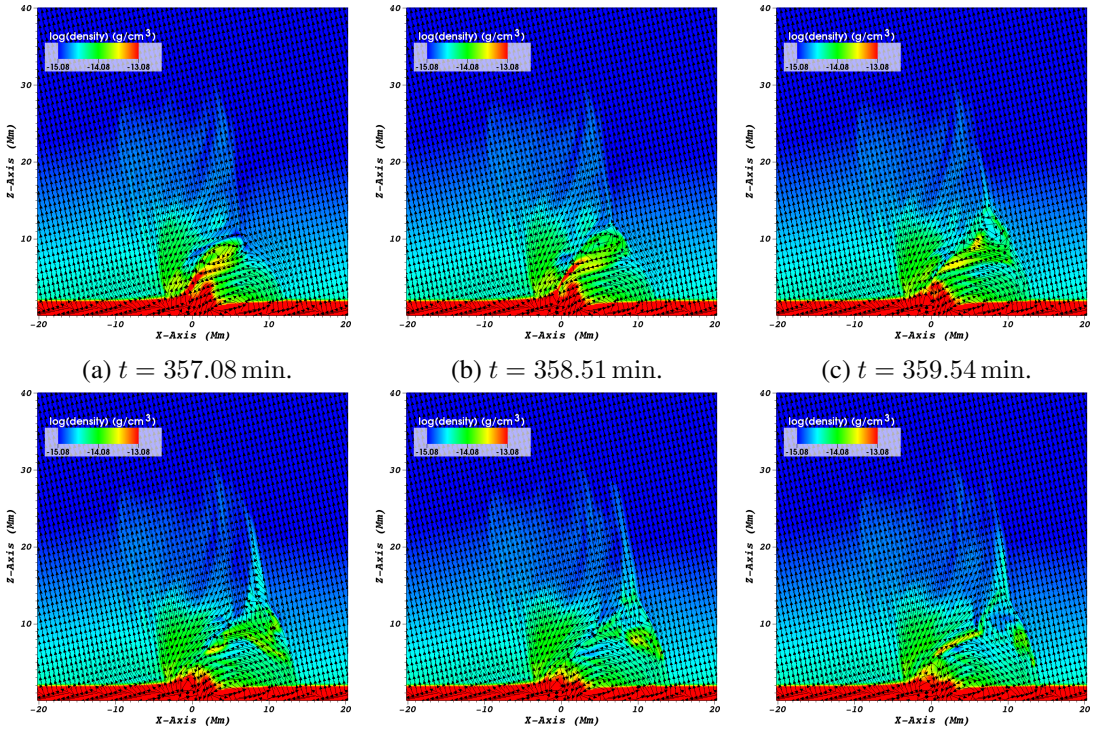

(a) $t = 357.08\,\mathrm{min}$. (b) $t = 358.51\,\mathrm{min}$. (c) $t = 359.54\,\mathrm{min}$.

(d) $t = 361.37\,\mathrm{min}$. (e) $t = 362.80\,\mathrm{min}$. (f) $t = 364.23\,\mathrm{min}$.

Figure 6.9: Density distribution during the third eruption across the flux tube, at $y = -4.5\,\mathrm{Mm}$. The overplotted arrows are the projected magnetic field vectors. The animated version of this figure is included in the attached CD (movie5.mp4).

untwisting motion of the jet while the jet is being emitted, which then results in the "blowout" jet being a helical jet instead of a straight jet. All these characteristics (the helical shape of the jet, the formation of two (internal and external) hot arcades, hot & cool material ejected along jet, broader jet channel) compare very well with the theoretical assumptions and recent observations of "blowout" jets (Moore et al., 2010).

In a similar manner to the previous chapter (Chapter 5), we study the untwisting motion of the jet by comparing the transverse velocity field v_x (Fig 6.11a) with the transverse magnetic field B_x distribution (Fig 6.11b). Figure 6.11 is taken during the eruption, when the erupting core is ejected along the jet channel, at time $t = 361.37\,\mathrm{min}$. Both panels are taken at $x = 7.2\,\mathrm{Mm}$, across the jet. It is found that the direction of the flow is opposite to the direction of the magnetic field lines, and hence the flow is moving oppositely to the field. This indicates that the jet undergoes an untwisting motion.

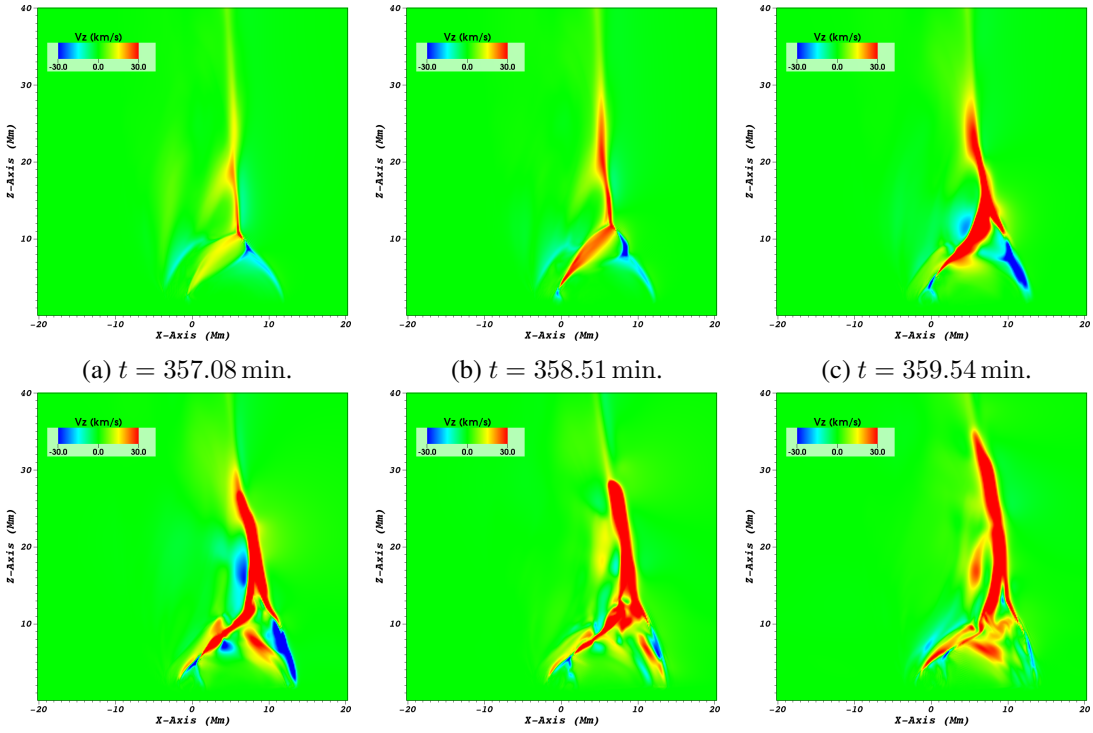

(a) $t = 357.08\,\mathrm{min}$. (b) $t = 358.51\,\mathrm{min}$. (c) $t = 359.54\,\mathrm{min}$.

(d) $t = 361.37\,\mathrm{min}$. (e) $t = 362.80\,\mathrm{min}$. (f) $t = 364.23\,\mathrm{min}$.

Figure 6.10: v_z distribution during the third eruption across the flux tube, at $y = -4.5\,\mathrm{Mm}$. The animated version of this figure is included in the attached CD (movie6.mp4).

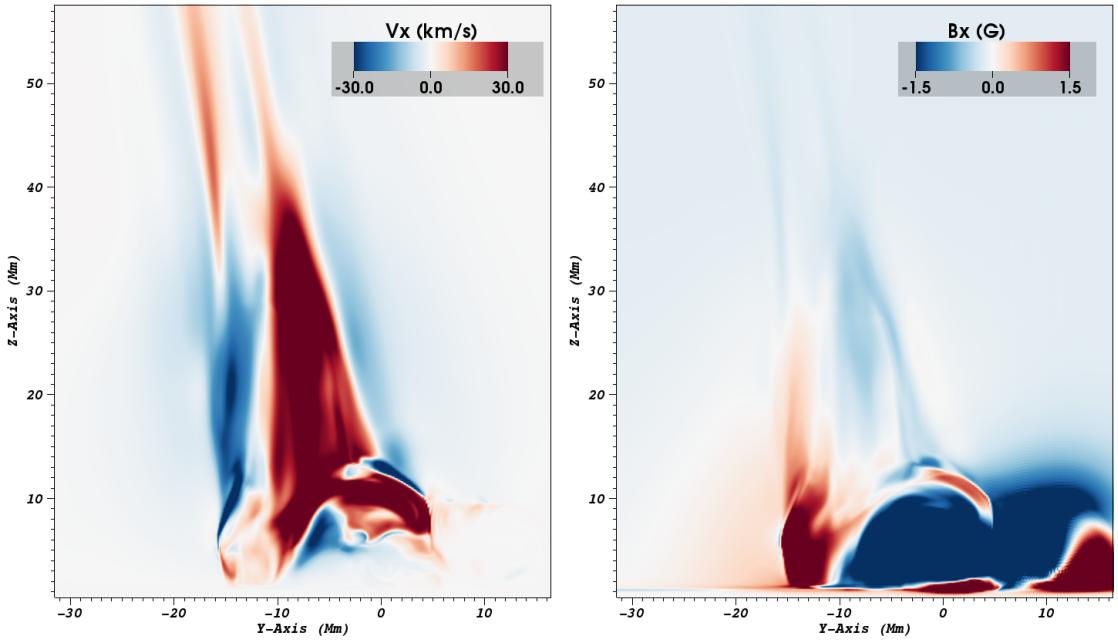

(a) v_x distribution. (b) B_x distribution.

Figure 6.11: Taken at $x = 7.2\,\mathrm{Mm}$ at time $t = 361.37\,\mathrm{min}$.

Onset and Evolution: 3D Analysis

To show the 3D shape of the jet during the eruption we plot the isosurface of the strong up- and down-flows around the erupting field (see left panels in Fig 6.12). Also, we trace field lines around the same region, to understand better the physical connection between the flows and the magnetic field. Notice that the snapshots in these figures have been taken at the same time as the snapshots in Fig 6.8, 6.9 & 6.10.

The left panels in Fig 6.12 show: (i) the external reconnection jet that is formed due to reconnection between the field lines, which are just above the erupting core, and the ambient field (Fig 6.12a and Fig 6.12b) and (ii) the initiation of the "blowout" jet. The (green) isosurfaces show that the external reconnection jet has a thin sheet-like shape (Fig 6.12c) while the "blowout" jet becomes much wider and it extends more towards the x-direction at its base (Fig 6.12e). The

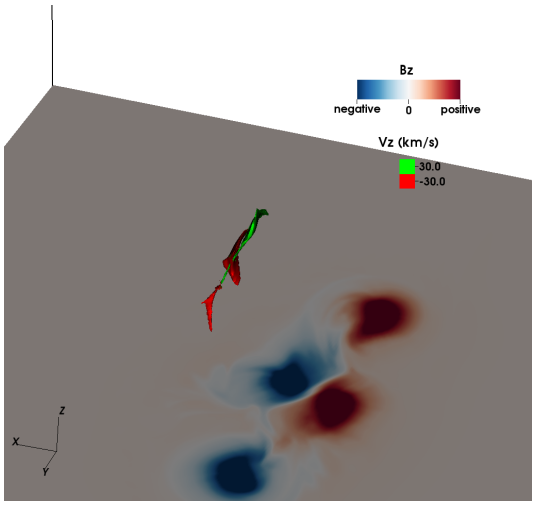

(a) $t = 357.08$ min.

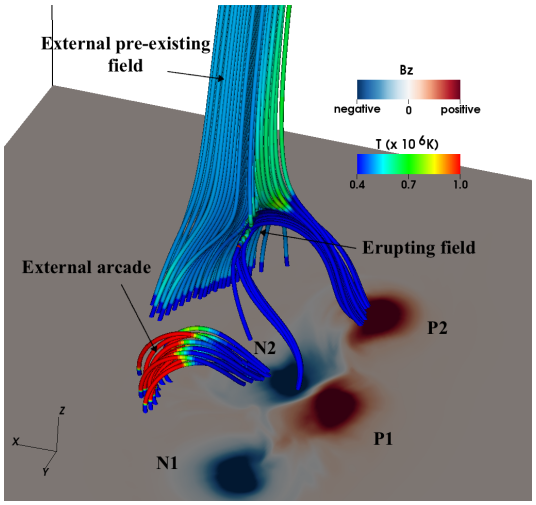

(b) $t = 357.08$ min.

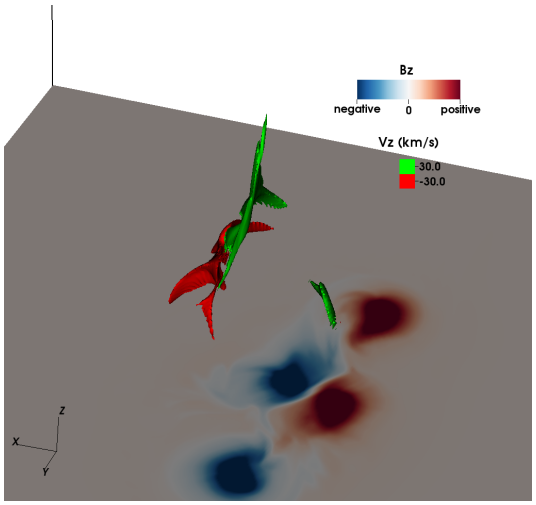

(c) $t = 358.51$ min.

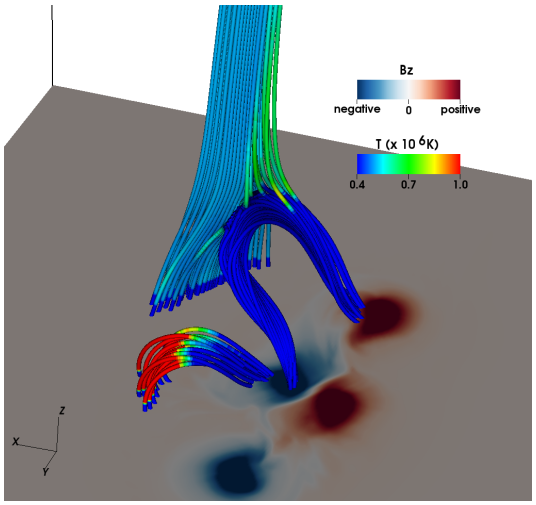

(d) $t = 358.51$ min.

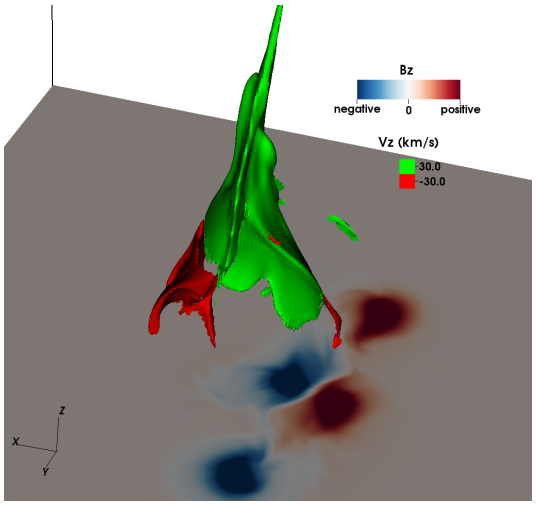

(e) $t = 359.94$ min.

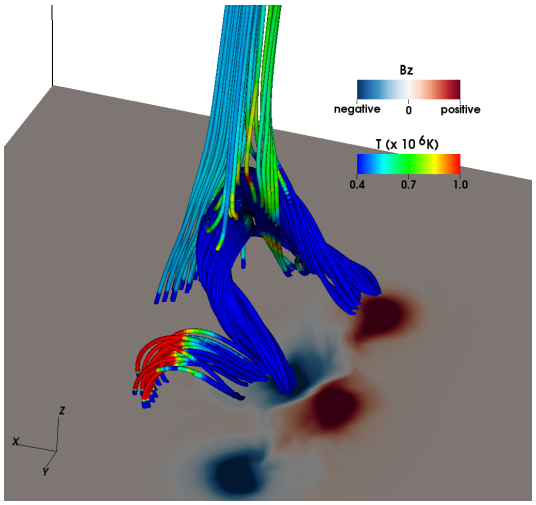

(f) $t = 359.94$ min.

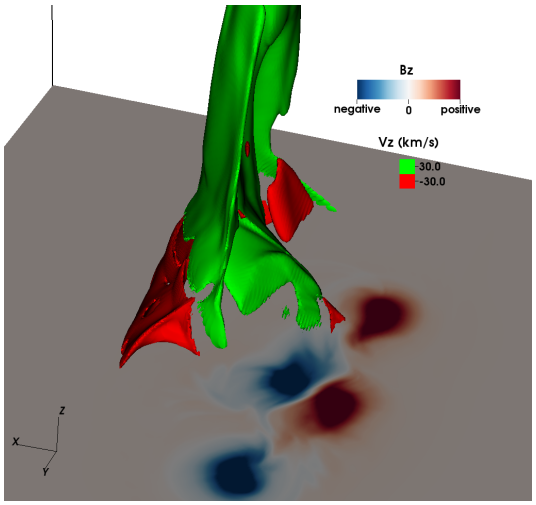

(g) $t = 361.37$ min.

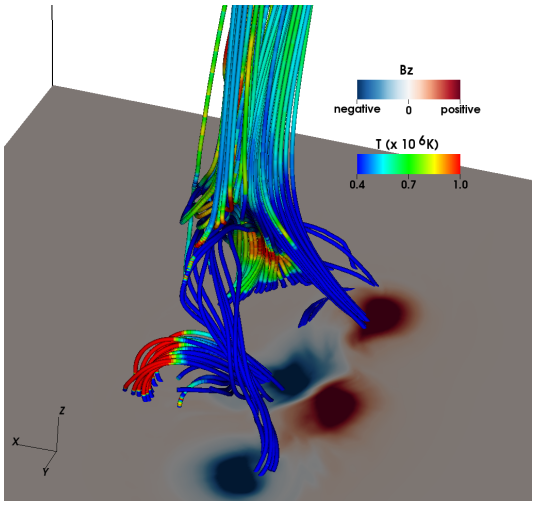

(h) $t = 361.37$ min.

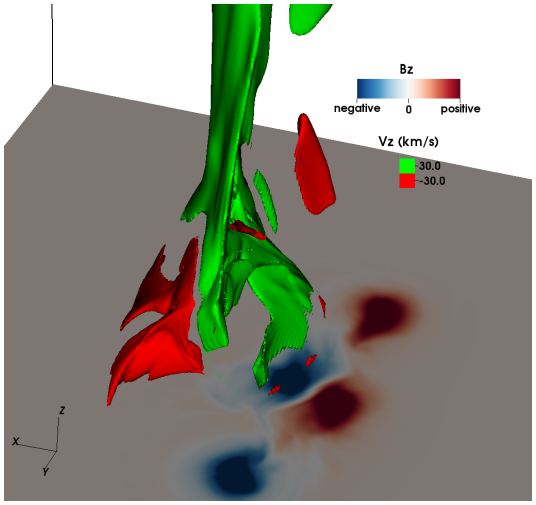

(i) $t = 362.80$ min.

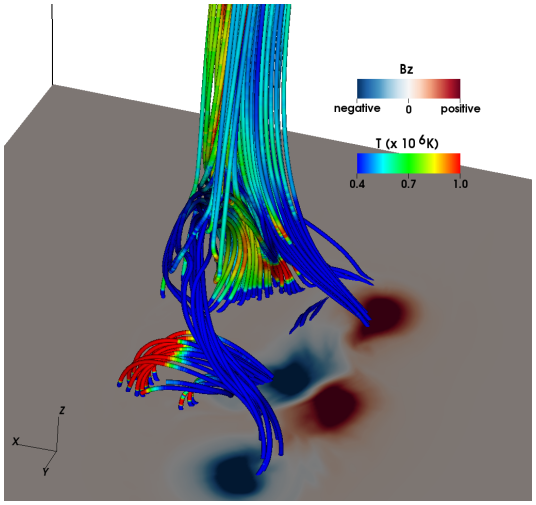

(j) $t = 362.80$ min.

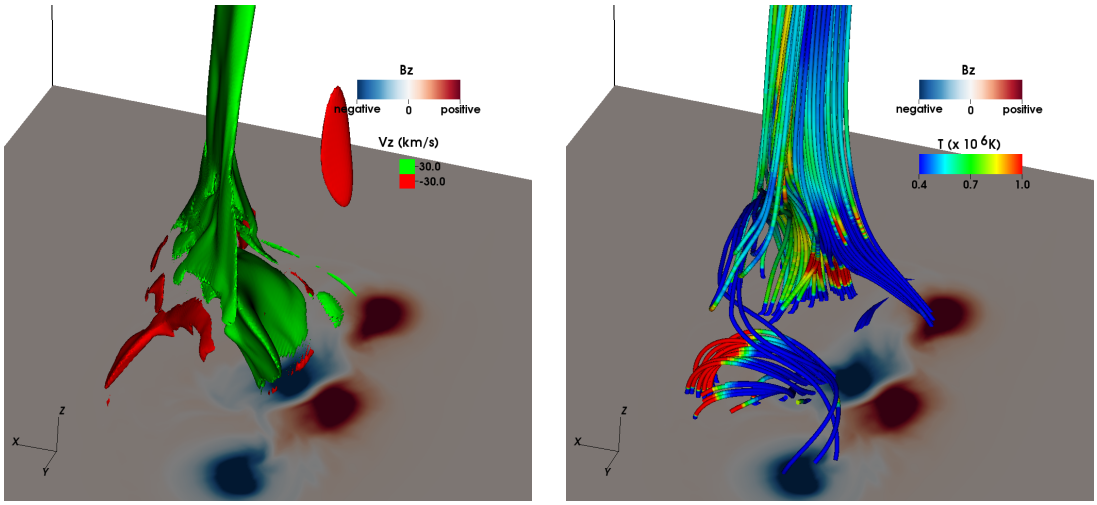

(k) $t = 364.23\,\mathrm{min}$. (l) $t = 364.23\,\mathrm{min}$.

Figure 6.12: (Left column, all panels) The 3D isosurface of v_z at different times during the third eruption, with green representing upflow and red representing downflow. The horizontal slice shows the magnetogram at the photosphere. (Right column, all panels) The topology of the magnetic field lines around the erupting field and the jet. They are coloured according to the value of the temperature.

widening of the 3D sheet-like structure is due to the ejection of the erupting core into the jet's channel. Towards the center of the quadrupolar region, there is a small (red) velocity filament (Fig 6.12e), which is the downward reconnection jet from the internal reconnection site. Towards the positive x-axis, the (red) isosurfaces show that the downflows occupy more space (as time goes on) and that they develop a loop-like structure under the jet. To understand better the shape of the velocity field we study the topology of the field lines around the same area.

In the right panels, we trace field lines from the external (pre-existing field), the erupting field and the external arcade. Initially (Fig 6.12b), the uppermost envelope field lines of the erupting field start to reconnect with the pre-existing ambient field. The up/down-flows (Fig 6.12a) are located around the reconnection site. The temperature along the reconnected field lines is higher (e.g. green colour) than the temperature of the erupting field lines (blue), which have not been reconnected yet. Due to external reconnection, the reconnected field lines that are released downward form the external arcade, where the temperature increases. The loop-like shape of the downflows (Fig 6.12e) correlates very well with the external arcade of the reconnected field lines. The downflows run along the sides of the external arcade.

The field lines of the erupting loop (e.g. in Fig 6.12d) reveal the twisted nature of its magnetic field (while the ambient field lines are non-twisted). As the field erupts and pushes the ambient field, reconnection occurs at many locations over the length of the rising loop (Fig 6.12f), which makes the "blowout" jet much broader over time (Fig 6.12e). Now the "blowout" jet consists of

field lines, which are more helical than before (Fig 6.12f), due to reconnection between the twisted (blue) erupting field and non-twisted (light blue) ambient field.

Figure 6.12g - Fig 6.12k (left panels) show that, eventually, the "blowout" jet becomes wider also at larger heights. This is due to the propagation of the erupting material along the jet's channel. The main upward spire of the jet retains its curved sheet-like shape, which extends all the way up into the corona. Together with the upflows at lower heights (due to the eruption and internal reconnection) and the downflows at the external arcade, the overall 3D velocity field structure adopts an inverted Y-shape configuration.

The visualization of the field lines (right panels in the same figure) shows that the field lines of the erupting plasma are gradually peeled off (almost all of them) due to external reconnection with the ambient field. This means that the erupting material has escaped (at least partially) into the ambient atmosphere along the reconnected field lines. This is indeed revealed by the colour of the reconnected field lines along the spire of the jet. The dark blue colour indicates that cool plasma (from the erupting core) has been ejected along the field lines of the "blowout" jet. It is now clear that the "blowout" jet has both cool and dense plasma along its channel. Using the 3D velocity field visualization and the coloured field lines we find that cool and hot plasma is practically confined within the 3D volume of the high speed upflow of the jet. The field line visualization shows also that during the formation of the "blowout" jet, more reconnected field lines are added to the external arcade.

Plasma Motion and Wave Propagation

To study the plasma motion of the "blowout" jet during the untwisting motion, we carry out the same study as in Chapter 5. We follow the evolution of $I_1 = \int \rho^2 \, \mathrm{d}y$ with plasma within a temperature range of $6 \times 10^5\,\mathrm{K} < T < 1.2 \times 10^6\,\mathrm{K}$ along height. Figure 6.13a-c show the distance-time contour plot of I_1 at three different heights, (a) $z = 18.0\,\mathrm{Mm}$, (b) $z = 27.0\,\mathrm{Mm}$, and (c) $z = 36.0\,\mathrm{Mm}$. The dark contours represent the transverse (x) movement of the jet, which is seemed to be oscillating along time. The basic characteristics of the transverse motion in this plot (e.g. the approximate height of the local extrema, the general shape that consists of two distinctive peaks, etc.) do not seem to change at different heights (i.e. from (a)-(c)) dramatically. This suggests that, apart from the transverse motion, there is propagation of the dense plasma along height. This could be considered as evidence of a jet emitting a transverse wave which propagates upwards in the solar atmosphere.

The running difference plot (Fig 6.13d-f) is used to better illustrate the propagation of the wave-like feature over time. Also, we use this plot to estimate the propagating speed of the plasma. To do this, we track the apex of the first peak. This is marked by a white cross, at each

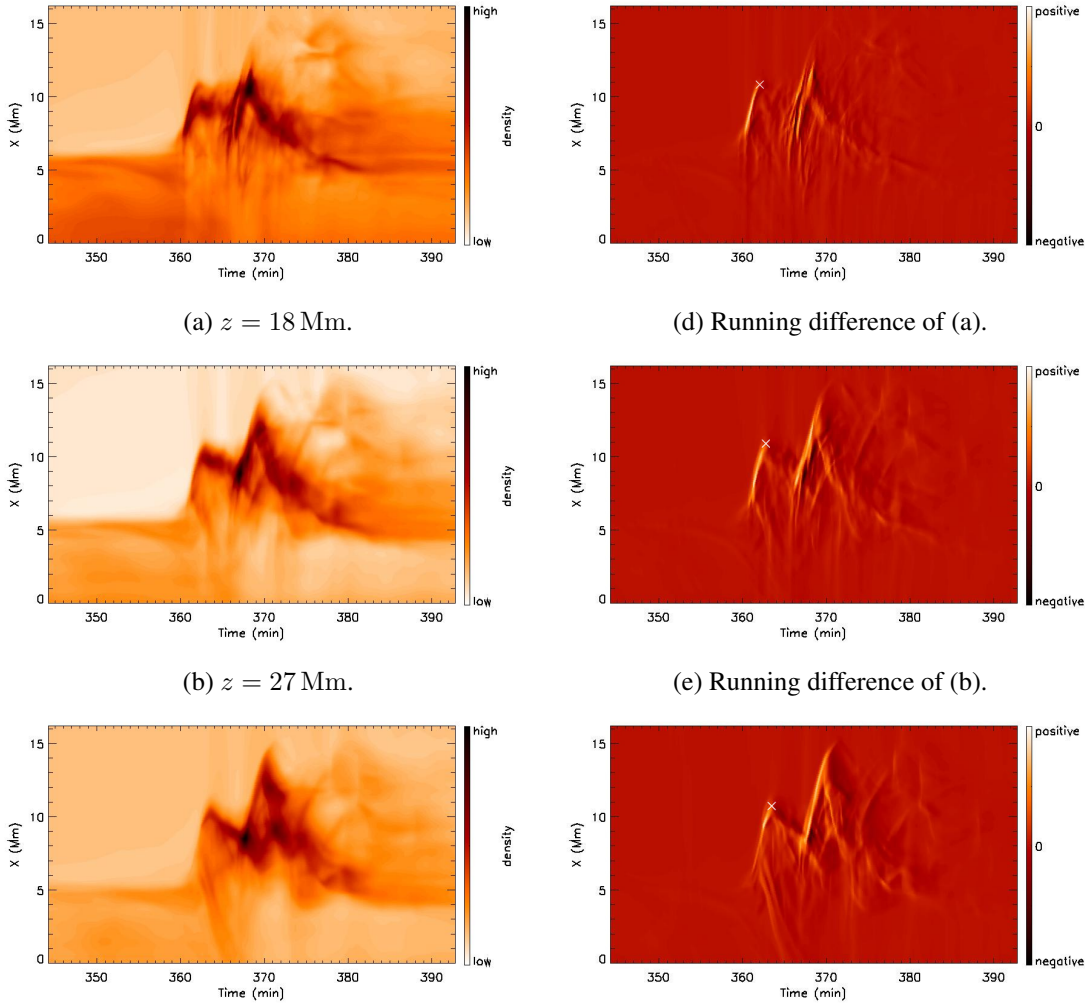

(a) $z = 18\,\mathrm{Mm}$.

(d) Running difference of (a).

(b) $z = 27\,\mathrm{Mm}$.

(e) Running difference of (b).

(c) $z = 36\,\mathrm{Mm}$.

(f) Running difference of (c).

Figure 6.13: (a-c): Distance-time diagram of $\int \rho^2 \, \mathrm{d}y$, for $6 \times 10^5\,\mathrm{K} < T < 1.2 \times 10^6\,\mathrm{K}$ across the jet at various height. (d-f): Running differences plot of (a-c).

height. We then obtain a height-time profile of the tracking point, as shown in Figure 6.14a. By simply calculating the first derivative of the height-time relationship, we obtain the propagation speed of the wave-like feature (Fig 6.14b). The solid line represents its velocity and the dashed line represents the local Alfvén speed at the tracking point. The graph reveals that the propagation speed is comparable to the local Alfvén speed, which implies that the propagating wave-like feature might be interpreted as an Alfvén wave. Thus, the above results show that the untwisting motion of the "blowout" jet may lead to the propagation of a torsional Alfvén wave in the solar corona. This is in agreement with the results of our previous experiment (see Chapter 5).

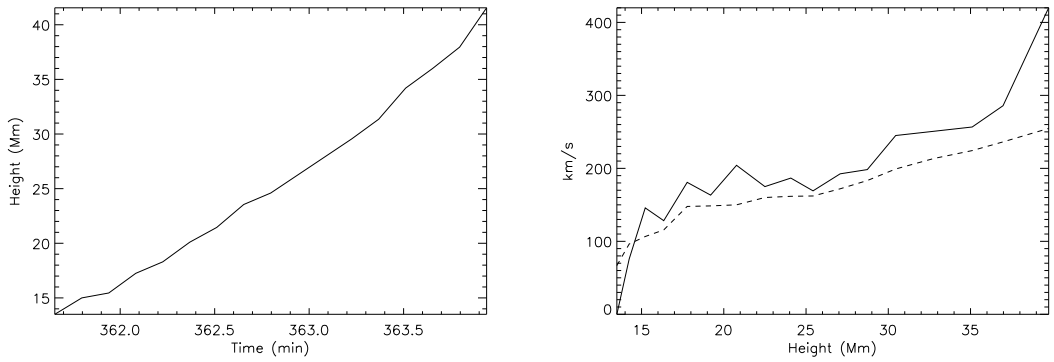

(a) (b)

Figure 6.14: (a) Height-time profile of the apex of the propagating plasma. (b) (Solid): Propagation speed of the plasma. (Dashed): local Alfvén speed at the tracking point.

6.2 6 G case

We performed another experiment, by increasing the field strength of the coronal ambient field to 6 G. The values of the other parameters of the system remained unchanged. Our aim is to examine how a stronger ambient field affects the dynamics of the jets.

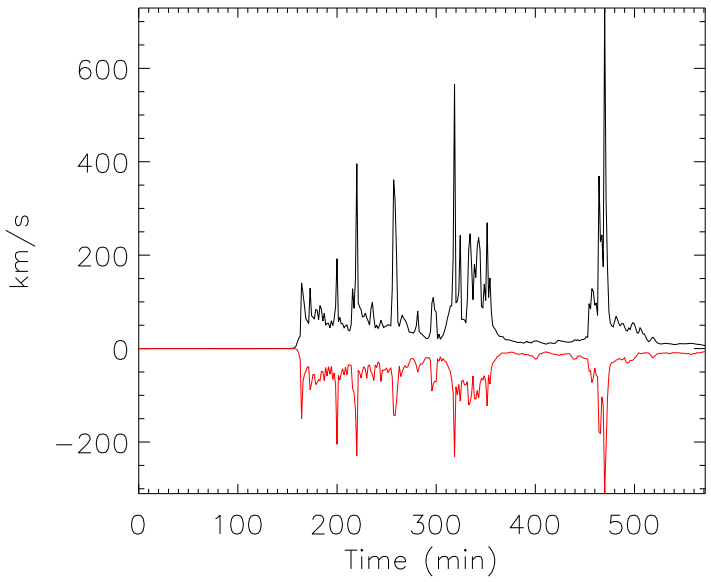

Figure 6.15: The temporal evolution of the maximum (black) & minimum (red) vertical velocity.

The temporal evolution of the maximum velocity of the upflow (black) & downflow (red) above the photosphere is shown in Figure 6.15. The flux tube emerges at the photosphere at $t = 160.0\,\mathrm{min}$, at the same time as in the 3 G case (Section 6.1). However, due to the stronger

coronal ambient field, the background Alfvén velocity $v_A = \mathbf{B}/\sqrt{\rho}$ is higher. Higher Alfvén speed leads to faster reconnection outflows, which explains why the strongest bi-directional flows run with higher speeds (e.g. between 200 and $700\,\mathrm{km\,s^{-1}}$) in this case. Figure 6.15 also shows that there are many other jets that run with relatively smaller velocities (in the range $50-100\,\mathrm{km\,s^{-1}}$), between the strongest events. These are also reconnection jets, which are emitted mainly due to interaction between the emerging and the ambient magnetic fields. Since the ambient field strength has increased, the emerging field cannot push it aside as easily as in the $3\,\mathrm{G}$ case. Instead, it reconnects with it at more locations where magnetic stresses build up to form current sheets. This process is even more prominent for stronger ambient fields (see the $10\,\mathrm{G}$ case below). Overall, the temporal evolution in Figure 6.15 shows a more episodic behaviour compared to the $3\,\mathrm{G}$ case.

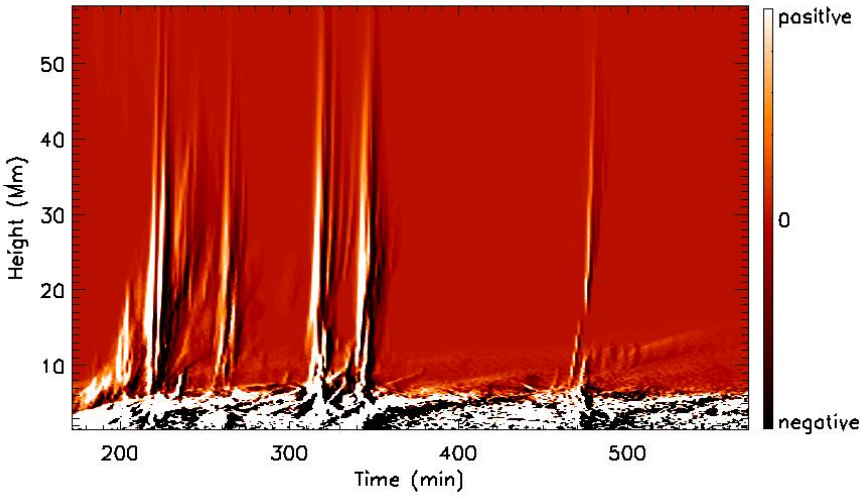

Figure 6.16: Height-time diagram of running difference plot for $\int \rho^2\,\mathrm{d}x\mathrm{d}y$, where $T > 8\times10^5\,\mathrm{K}$.

In a similar manner to Figure 6.2, Figure 6.16 shows the running difference of the variable $\int \rho^2\,\mathrm{d}x\,\mathrm{d}y$ for $T > 8\times10^5\,\mathrm{K}$. Several small reconnection jets are emitted in the time period between $t = 165\,\mathrm{min}$ and $t = 200\,\mathrm{min}$. These jets reach low heights within the solar atmosphere. The dense plasma, which is ejected along their channels, is transported up to $z = 10-20\,\mathrm{Mm}$. Later on, five profound events are found throughout the simulation, at $t \approx 220$, 260, 320, 340 and $470\,\mathrm{min}$. These events correspond to the emission of "blowout" jets driven by eruptions of cool and dense material.

Now we carry out the same analysis as before, in order to study transverse motions of the plasma during the emission of the jet(s) and the possible existence of upward propagating waves during the untwisting motion of the jets. We show the results of our study for one of the emitted "blowout" jets: the jet that occurs at $t \approx 320.0\,\mathrm{min}$. As in previous sections, we calculate the quantity $I_1 = \int \rho^2\,\mathrm{d}y$ within the temperature range of $6\times10^5\,\mathrm{K} < T < 1.2\times10^6\,\mathrm{K}$ along height. We show the distance-time plot in Figure 6.17a-c at three different heights, (a) $z = 18.0\,\mathrm{Mm}$, (b)

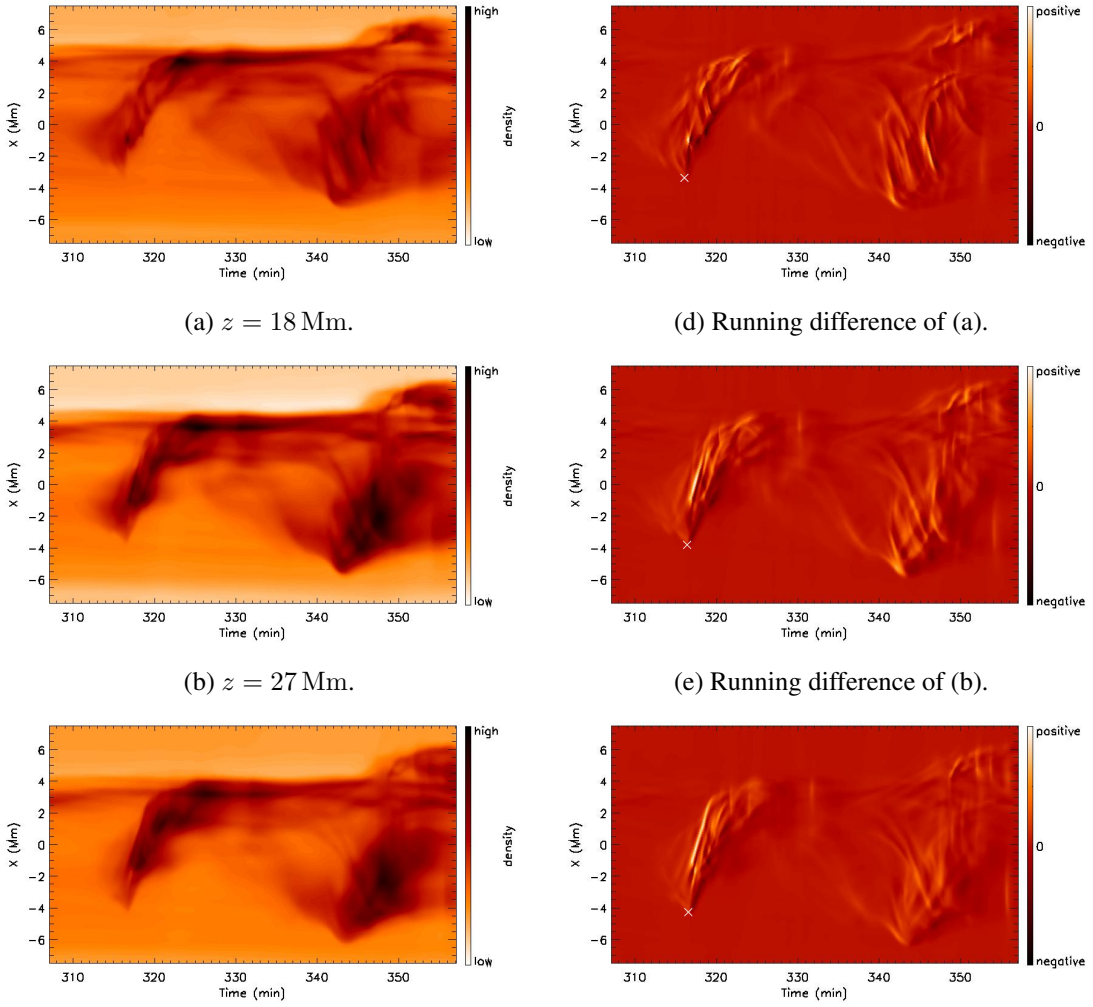

(a) $z = 18\,\mathrm{Mm}$.

(d) Running difference of (a).

(b) $z = 27\,\mathrm{Mm}$.

(e) Running difference of (b).

(c) $z = 36\,\mathrm{Mm}$.

(f) Running difference of (c).

Figure 6.17: (a-c): Distance-time diagram of $\int \rho^2\,\mathrm{d}y$, for $6 \times 10^5\,\mathrm{K} < T < 1.2 \times 10^6\,\mathrm{K}$ across the jet at various height. (d-f): Running differences plot of (a-c).

$z = 27.0\,\mathrm{Mm}$, and (c) $z = 36.0\,\mathrm{Mm}$.

From the distance-time diagram, we find that indeed the plasma is moving in the transverse direction. It starts from the negative x-direction (close to $x = -4\,\mathrm{Mm}$) and it moves towards the positive x-direction (up to $x = 4\,\mathrm{Mm}$). After running this distance, the plasma does not show to move backwards (towards the negative x-direction) again. In fact, it stays close to the $x = 4\,\mathrm{Mm}$, where it undergoes very weak oscillations. However, this is difficult to be seen from Figure 6.17. The dark contours at times after $340\,\mathrm{min}$ and $x \sim -5\,\mathrm{Mm}$ correspond to another jet.

Looking at Fig 6.17, we also find that a very similar plasma motion occurs at larger heights. This implies propagation of the plasma along height. We use the running difference plot in

Fig 6.17d-f to follow this propagation. We mark the position from where this transverse motion starts (it is marked by a white cross) and we do this for every height. In this way, we obtain the height-time profile of the "front" of the propagation, as plotted in Figure 6.18a.

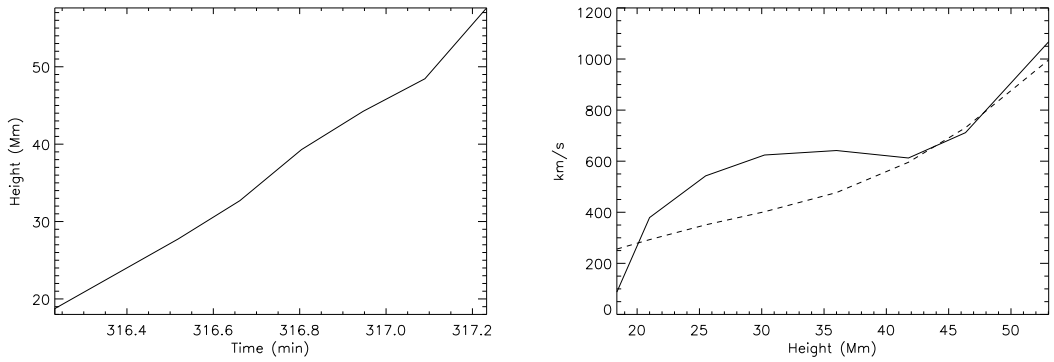

(a) (b)

Figure 6.18: (a) Height-time profile of the apex of the propagating feature. (b) (Solid): Propagation speed of the plasma. (Dashed): local Alfvén speed at the "front" of the propagation.

The propagation speed of the plasma during this transverse motion is estimated by taking the derivative of the height-time profile (Figure 6.18b). Similar to Figure 6.14b, the solid line represents the propagation speed of the plasma, and the dashed line the local Alfvén speed. As before, we find that the two speeds are comparable. This result indicates that the untwisting motion of the "blowout" jet leads to the propagation of a torsional wave-like feature, which runs with the Alfvén speed.

6.3 $10\,\mathrm{G}$ case

In this section we study the evolution of the system when *bcor* increases to $10\,\mathrm{G}$, while the other parameters keep their original values.

Figure 6.19 shows the temporal evolution of the maximum velocity of the upflow & downflow. The flux tube emerges into the photosphere at the same time as in the previous two cases, at around $t = 160.0\,\mathrm{min}$. As mentioned before, we expected the temporal evolution to be even more episodic due to a larger number of reconnection jets. This is indeed revealed in Figure 6.19. For instance, there is a series of reconnection jets that are emitted just after the emergence of the field at the photosphere, with speeds between 100 and $200\,\mathrm{km\,s^{-1}}$. Similar jets are emitted at times between $t = 350.0\,\mathrm{min}$ and $t = 450.0\,\mathrm{min}$. Obviously, Figure 6.19 does not show the emission of many other reconnection jets with smaller speeds. The addition of all these jets in this plot, would make the temporal evolution of v_z extremely intermittent. As in the previous cases, the

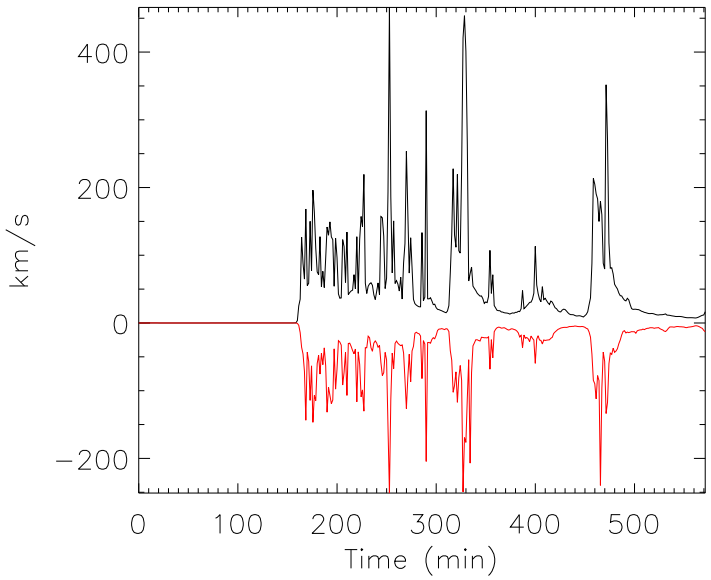

Figure 6.19: The temporal evolution of the maximum (black) & minimum (red) vertical velocity.

bi-directional flows with very high speeds (e.g. the flows at $t \sim 250.0\,\mathrm{min}$) occur during the onset/emission of a "blowout" jet.

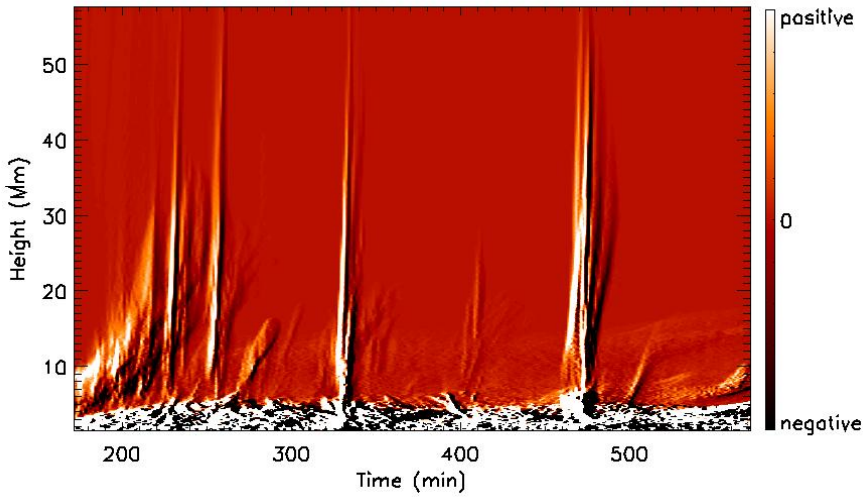

Figure 6.20: Height-time diagram of running difference plot for $\int \rho^2 \,\mathrm{d}x\mathrm{d}y$, where $T > 8 \times 10^5\,\mathrm{K}$.

Figure 6.20 shows the contour plot of the same quantity as in Fig 6.2 & Fig 6.16. We find that four profound "blowout" jets are emitted after the initial emergence (i.e. at approximate times of $t = 230.0\,\mathrm{min}$, $t = 255.0\,\mathrm{min}$, $t = 330.0\,\mathrm{min}$ and $t = 470.0\,\mathrm{min}$). The ejection of dense material into the solar atmosphere, which we find to occur at other times (e.g. between $t = 160.0\,\mathrm{min}$ and

$t = 220.0\,\mathrm{min}$), corresponds to reconnection jets due to the interaction between the emerging and ambient fields. In general, the running difference plot reveals that there is more activity (e.g. in the form of reconnection jets) when the ambient field is stronger and that this activity brings (more) dense plasma in the solar corona.

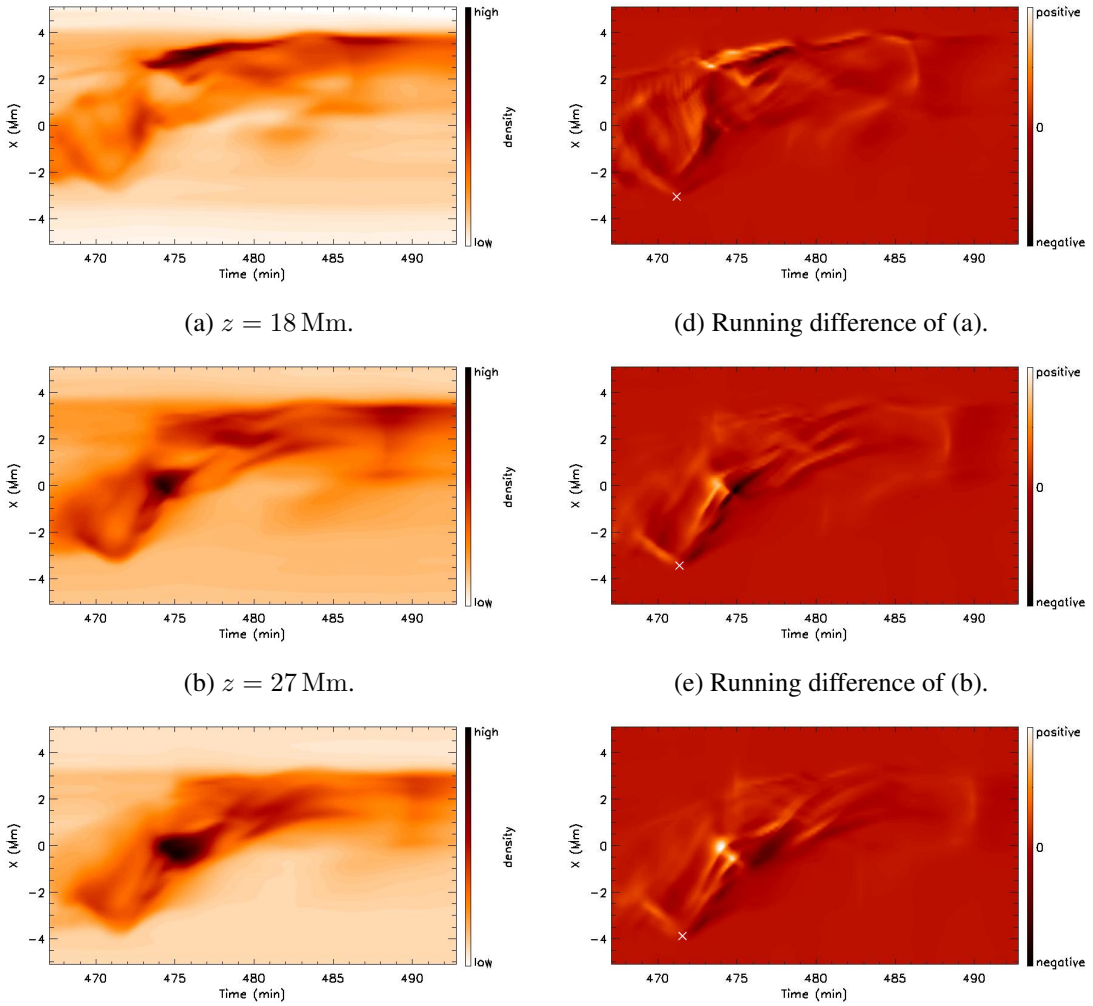

(a) $z = 18\,\mathrm{Mm}$.

(d) Running difference of (a).

(b) $z = 27\,\mathrm{Mm}$.

(e) Running difference of (b).

(c) $z = 36\,\mathrm{Mm}$.

(f) Running difference of (c).

Figure 6.21: (a-c): Distance-time diagram of $\int \rho^2\,\mathrm{d}y$, for $6 \times 10^5\,\mathrm{K} < T < 1.2 \times 10^6\,\mathrm{K}$ across the jet at various height. (d-f): Running differences plot of (a-c).

For the detection of waves during the emission of the "blowout" jets, we carry out the same analysis as in the previous sections. We apply our method to the "blowout" jet, which occurs at $t = 464.2\,\mathrm{min}$. We plot the quantity $I_1 = \int \rho^2\,\mathrm{d}y$ within the same temperature range of $6 \times 10^5\,\mathrm{K} < T < 1.2 \times 10^6\,\mathrm{K}$. Figure 6.21a-c shows the results at three different heights: (a) $z = 18.0\,\mathrm{Mm}$, (b) $z = 27.0\,\mathrm{Mm}$, and (c) $z = 36.0\,\mathrm{Mm}$.

We find that dense plasma is moving transverse to the magnetic field (Fig 6.21a-c). Firstly,

it is moving from $x \sim -2.5\,\mathrm{Mm}$ to $x \sim -4\,\mathrm{Mm}$ and then towards the positive x-direction until $x \sim 0\,\mathrm{Mm}$. After that time, the heavy material undergoes weak oscillations, (mainly) within the positive x-direction. Similar plasma motions are found at the three chosen heights, which indicates propagation of plasma along height.

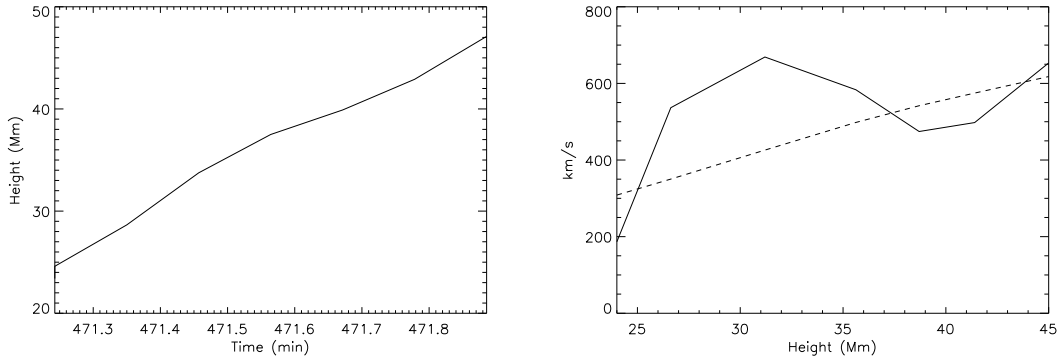

(a) (b)

Figure 6.22: (a) Height-time profile of the propagating plasma. (b) (Solid): Propagation speed of the plasma. (Dashed): local Alfvén speed at the tracking point.

The running difference is plotted in Figure 6.21d-f. To find the propagation speed of the plasma, we obtain the height-time profile (Figure 6.22a) of the 'lower' position of the plasma during its transverse motion (i.e. the far point in the negative x-axis). This position is marked by a white cross in Figure 6.21d-f. The propagation speed is then shown at Figure 6.22b by taking the derivative of the height-time profile. Then, we compare the propagation speed with the local Alfvén speed, and we find that they are comparable. This is an indication that this might be interpreted as a torsional Alfvén wave, which propagates along the jet, during the untwisting motion of the "blowout" jet.

6.4 Pseudo-synthetic Images

Our simulations do not include heat conduction and radiative transfer. Therefore, we cannot produce synthetic images to compare directly with observations. However, for visualization reasons, we can produce pseudo-synthetic images that can help us to follow the temporal and spatial evolution of the jets at different temperatures (in a 3d-like manner). More precisely, we can produce pseudo-synthetic (*SDO/AIA*) images of the "blowout" jets. To make these images, we calculate the intensity I_i at each grid point, where I_i is defined as

$$I_i = G(T_i) n_{\mathrm{e},i}^2. \tag{6.5}$$

Here $G(T_i)$ is the response function of the *SDO/AIA* filters interpolated at the grid points, T_i is the temperature, and $n_{\mathrm{e},i}$ is the electron density. The images are then produced by integrating I_i along the line of sight direction.

The response functions ($G(T_i)$) are calculated using the instrumental routines provided by SolarSoft, based on the chianti atomic database CHIANTI v7.1 (Dere et al., 2009; Landi et al., 2013).

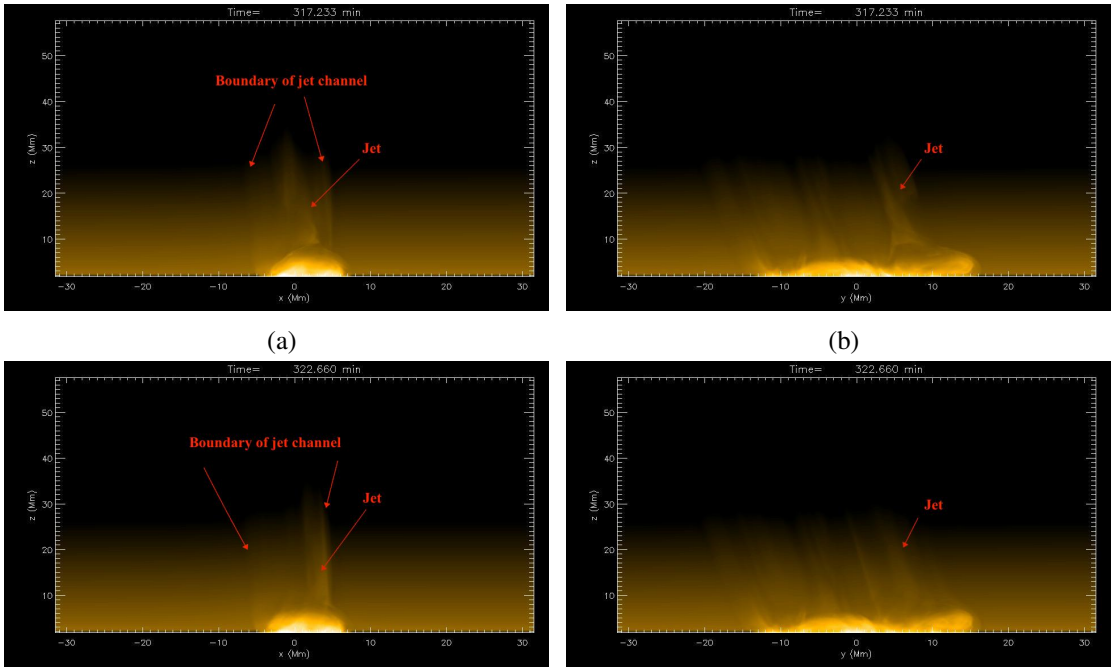

Figure 6.23: Pseudo-synthetic images of the "blowout" jet in the $bcor = 6\,\mathrm{G}$ case, which we have shown in Fig 6.18a at times: (a,b) $t = 317.23\,\mathrm{min}$; (c,d) $t = 322.66\,\mathrm{min}$. The left panels show the jet in the $x - z$ plane, and the right panels in the $y - z$ plane. Movies of the pseudo-synthetic images showing the temporal evolution of the "blowout" jet are included in the attached CD. (movie7.mp4 for the $x - z$ direction; movie8.mp4 for the $y - z$ direction)

Fig 6.23 shows the pseudo-synthetic images of the "blowout" jet, which we have presented in Fig 6.18a, and it is visualized using the *SDO/AIA* 171Å filter. Panel (a) shows the bright (semi-circular) base of the jet, the boundaries of the wide channel of the jet and the core (main part) of the jet. At this time, the jet has been already triggered and it is emitted along the reconnected field lines, towards the outer solar atmosphere. The emerging field and the field lines, which suffer from shearing and reconnection, lie within the bright base of the jet. The two boundaries indicate how wide the channel of the jet is. In other words, they show the area of the ambient field, which has been opened due to external reconnection and the eruption of the field. The core of the jet facilitates the dense material of the erupting flux rope, which is emitted from the low atmosphere towards the corona. Panel (b) shows the inverted Y-shape of the jet and reveals that

this jet originates from the right bipolar region. In the same panel, one can notice that there are many places within the quadrupolar region where dense plasma is emitted along the direction of the pre-existing field. These are thin (not so profound) jets, which are emitted either due to external reconnection or due to small-scale eruptions of dense chromospheric material. Panels (c) and (d) show the evolution of the jet at a later time. These images reveal that the jet is moving towards the positive x-axis and the negative y-axis, namely towards the central PIL between the two bipolar regions. In panel (c), we note that the core of the jet is moving against the right boundary, where further reconnection occurs between the erupting core and the pre-existing field lines of the boundary. Eventually, some of the dense material of the erupting core will move downwards (towards the bright base) following the reconnected field lines, but most of it will be ejected upwards. These images can be used as a useful visualization tool, in order to understand the motion of the jet (also, in relation to the other parts of the overall system) and the dynamical evolution of the dense plasma during the emission of the jet (see also the attached movies).

6.5 Density and Flux Transport: Comparison Between the Three Cases

One of the interesting results in the previous sections is that when the ambient field is stronger there are more jets, which are emitted due to reconnection between the emerging and the ambient magnetic field. This has implications on the transport of flux and density in the solar atmosphere.

Also, the stronger ambient field halts the expansion of the magnetic envelope in the vertical direction, due to its larger magnetic pressure. Thus, we find that when we increase the strength of the ambient field, the emerging field expands up to progressively lower heights before it experiences efficient reconnection (leading to onset of jets) with the ambient field. For instance, in the $bcor = 3\,\mathrm{G}$ case, the envelope field is found to expand up to $z \approx 8.1\,\mathrm{Mm}$. In the $bcor = 6\,\mathrm{G}$ case, it expands up to $z \approx 6.6\,\mathrm{Mm}$, and in the $bcor = 10\,\mathrm{G}$ case, the envelope field is found to expand only up to $z \approx 5.1\,\mathrm{Mm}$.

To find how much heavy plasma is transferred into the solar atmosphere by the jets and eruptions, we plot the temporal evolution of the (normalized) maximum and average density (Fig 6.24a and Fig 6.24b, respectively) just above the envelope field of the emerging loops. We choose this height because the emission of the jets occurs mainly at the interface (where strong currents are build up) between the envelope field and the ambient field. Then, we calculate the density (maximum and average) from that height and above until the top of the numerical domain.

It is found that more mass is transferred into the solar atmosphere when the ambient field is stronger. This agrees with our results in previous sections, which indicated that more activity and

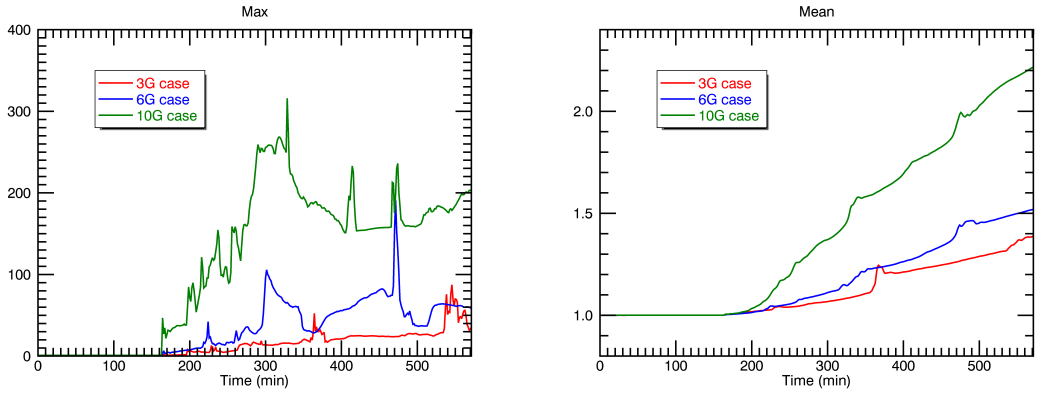

(a) (b)

Figure 6.24: Different colours in the graph represent different experiments: (red) $bcor = 3\,\mathrm{G}$ case, (blue) $bcor = 6\,\mathrm{G}$ case, (green) $bcor = 10\,\mathrm{G}$ case. (a) Temporal evolution of (max ρ)/(max $\rho_{t=0}$) above the magnetic envelope field. (b) Temporal evolution of (mean ρ)/(mean $\rho_{t=0}$) above the magnetic envelope field.

more jets are triggered when the fields that interact are stronger. Fig 6.24a shows that there is a very good correlation between the times when the density increases and the times of the onset of the reconnection ("standard" and "blowout") jets in each experiment. For instance, the overall episodic increase of density, in the case of $10\,\mathrm{G}$ for the period $t \approx 160\,\mathrm{min}$ - $t \approx 330\,\mathrm{min}$, compares very well with the activity found in Fig 6.20 for the same time period. After that period, the density increases when an eruption ejects dense plasma along the channel of a "blowout" jet. Similarly, Fig 6.24b shows that average density is much larger when the ambient field is stronger. For the $3\,\mathrm{G}$ and $6\,\mathrm{G}$ cases, the average density of the plasma is not very different. At the end of the experiments, the average plasma density in the solar atmosphere has increased by a factor of 2.2 for the $10\,\mathrm{G}$ case and by $1.4 - 1.5$ for the other two cases. Notice that in all experiments, the average density increases almost monotonically over time (although with a different rate), which shows the persistent transfer of mass by jets from the low atmosphere towards the outer atmosphere.

We have also calculated the total energy flux, which is transferred upwards, by the emission of the produced jets. For the calculation, we consider only upflows with speeds $v_z \geq 20\,\mathrm{km\,s^{-1}}$. These upflows are typically located within the channel of the jets. Also, we do the calculation for heights just above the envelope field of the emerging loops, at the reconnection site between the upcoming and the pre-existing magnetic fields. These heights are: $z \approx 8.1\,\mathrm{Mm}$ for the $3\,\mathrm{G}$ case, $z \approx 6.6\,\mathrm{Mm}$ for the $6\,\mathrm{G}$ case, and $z \approx 5.1\,\mathrm{Mm}$ for the $10\,\mathrm{G}$ case.

Taking into account the work by Paraschiv et al. (2015), we calculate the total energy flux as the sum of the kinetic flux F_{kin}, enthalpy flux F_{enth}, and the Alfvén wave flux F_A. The three

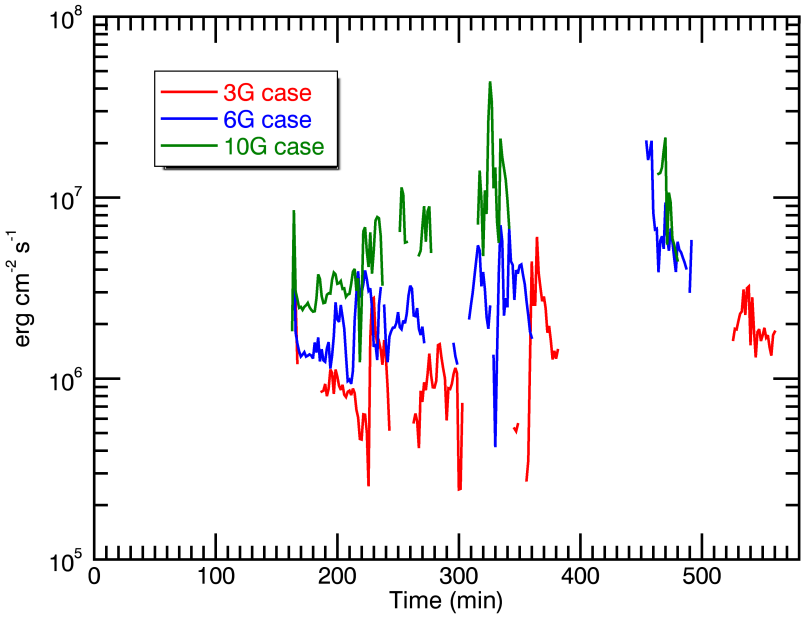

Figure 6.25: Total energy flux along the jet at a horizontal sheet near the reconnection site between the envelope field and the ambient field.

terms are expressed as:

$$F_{kin} = \frac{1}{2}\rho \cdot v_z^2 \cdot v_z \tag{6.6}$$

$$F_{enth} = \frac{\gamma}{\gamma - 1} \cdot p \cdot v_z \tag{6.7}$$

$$F_A = \rho \cdot v_{lat}^2 \cdot \frac{B}{\sqrt{4\pi\rho}}, \tag{6.8}$$

where ρ is the density along the jet, v_z is the upflow of the jet, $\gamma = 5/3$ is the specific heat ratio, p is the gas pressure, $v_{lat} = \sqrt{v_x^2 + v_y^2}$ is the lateral motion velocity, and B is the magnetic field strength. The kinetic flux represents the rate of change of the kinetic energy at that height, along the ejected jet, and the enthalpy flux represents the rate of change of the thermodynamic energy of the jet. The Alfvén wave flux represents the energy propagating outward with the jet, when the Alfvén waves are created due to the transverse motions of the jet.

Figure 6.25 shows the temporal evolution of the total energy flux. In all cases, the evolution is highly intermittent, which indicates the emission of numerous upflows (e.g. upward reconnection jets) during the emergence of a quadrupolar region into a magnetized solar atmosphere. As expected, in the 10 G case, the energy flux carried by jets is higher. Local maxima occur during the emission of "blowout" jets. We have also estimated that the dominant term of the total energy flux

(in all experiments) is the enthalpy flux, which is about $2-8$ times larger than the kinetic flux during the emission of jets. This is in agreement with the results by Paraschiv et al. (2015). Finally, Figure 6.25 shows that the average magnitude of the energy flux is between $\mathcal{O}(10^6)\mathrm{erg\,cm^{-2}\,s^{-1}}$ (for the $3\,\mathrm{G}$ and $6\,\mathrm{G}$ cases) and close to $\mathcal{O}(10^7)\mathrm{erg\,cm^{-2}\,s^{-1}}$ (for the $10\,\mathrm{G}$ case). These values indicate that the eruptions and jets in such emerging flux regions may contribute to the driving of the solar wind.

Chapter 7

Conclusions

In this thesis, we have investigated the onset and evolution of eruptions and jets in quadrupolar regions in the Sun. We have used 3D resistive MHD simulations to form a quadrupolar region via the emergence of magnetic flux from the solar interior. The initial magnetic field was a horizontal, twisted magnetic flux tube, which was placed a few Mm underneath the photosphere. The emergence of the flux tube was initiated by imposing a density deficit along the flux tube. The density deficit was maximum at two locations so that the tube developed two magnetic loops during its emergence within the convection zone. Thus, two bipolar regions appeared at the solar surface when the initial magnetic flux system reached the photosphere.

Our aim behind the setup of this initial condition was to study a magnetic field configuration, which has not been studied in detail before, although it has been repeatedly observed on the Sun and it has been shown that it can host intense activity (e.g. in the form of jets, flares and eruptions). This configuration is a quadrupolar region and it is different from the single bipolar emergence, which has been extensively studied in the past, especially by means of simulations. In the following, we briefly describe the main conclusions, which have been derived based on the results of our numerical experiments.

In Chapter 4, we studied the emergence into a highly idealized solar atmosphere, where there was no ambient coronal magnetic field. The reason for this initial configuration was that we wanted to study the emergence without any interaction with a pre-existing magnetic field. We wanted to explore whether the quadrupolar region can evolve dynamically (by itself) so that it can host explosive events and intense magnetic activity.

We found that eruptions of dense plasma originate from this region. These eruptions are initially driven by the interaction of the two bipolar regions. During the emergence, the outer polarities of the quadrupolar region move away from each other, while the inner polarities come

closer and induce a shearing between them (as they move in opposite directions and they do not merge). Using 3D magnetic field line and isosurface visualization, we found how an intricate reconnection of the sheared field lines leads to the formation of flux ropes (twisted magnetic flux tubes).

The flux ropes undergo an eruptive phase, which initially shows an ejective behaviour. However, we found that the eruptions do not manage to break out of the envelope magnetic field, which consists of field lines that join the outer polarities of the quadrupolar region. This envelope field has a downward tension that overwhelms the Lorentz force, which is the main force that drives the eruptions. The downward tension is not released (enough) by e.g. an external process such as reconnection and thus it stops the full escape of the eruptive flux ropes towards the outer atmosphere. Therefore, the eruptions are confined.

The eruption of the flux ropes brings heavy plasma from the chromosphere/transition region into the corona. This plasma is carried upwards by the twisted field lines of the eruptive field. Underneath the erupting field, there is a flare current sheet where tether-cutting reconnection is taking place. There, the plasma is heated to X-ray temperatures (a few million Kelvin), leading to flaring activity. We conjecture that this activity is recurrent; it happens everytime that a flux rope is formed at the PIL between the inner polarities and has the energy to erupt.

In Chapter 5, we used a more realistic solar atmosphere in our simulations. We included a weak magnetic field, with a field strength of about $3\,\mathrm{G}$ and an oblique orientation, which favours "external" reconnection between the emerging and the ambient field. Our aim was to study the manifestation of the magnetic activity in a quadrupolar region after the interaction between the emerging and the pre-existing magnetic field.

As expected, we found that external reconnection leads to the emission of EUV/X-ray jets, as it has been described by many other authors in the past. We call these jets "standard" jets, adopting the terminology used in the work by Moore et al. (2010). More interestingly, we found that the confined eruptions were evolved into ejective eruptions. The external reconnection removed the downward tension of the overlying field in a break-out manner and, thus, the eruptions were not confined anymore but they were free to expand and move towards the outer solar atmosphere.

These eruptions induced an upflow to the external (break-out) current sheet and, thus, they enhanced reconnection. During the eruption, the cool eruptive core is ejected along the reconnected field lines and it widens-up the channel of the upward reconnection jet. Now this jet is broader than a standard jet and it consists of cool and hot plasma. This mechanism, which is driven by an eruption, powers the onset of a "blowout" jet. Our simulations re-produced some of the main characteristics of the "blowout" jets, such as the bright point underneath the erupting field, the formation of the external arcade, the widening of the channel of the jet, etc.. We also showed that "blowout" jets are helical jets that undergo untwisting motion due to the relaxation of twist during

the reconnection between the twisted field lines of the erupting core and the non-twisted ambient field.

At the end of this chapter, we showed that a "blowout" jet undergoes an oscillatory motion, at different heights across the solar atmosphere, during its emission, and this oscillatory motion propagates from lower to higher heights. We found that the propagation velocity is comparable to the local Aflvén speed. This together with the fact that the "blowout" jet undergoes an untwisting motion suggest that we are witnessing the propagation of a torsional Aflvén wave during the untwisting motion of the "blowout" jet. We found similar results when we increased the strength of the ambient field.

In Chapter 6, we carried out a parametric study to examine the effect of the coronal ambient field strength on the onset and evolution of the eruptive phenomena. We used the same initial set-up as in the previous chapter(s), with the difference that we varied the strength of the ambient field from $3\,\mathrm{G}$ to $6\,\mathrm{G}$ and $10\,\mathrm{G}$. We found that one of the main effects is that the stronger ambient field suppresses the vertical expansion of the magnetic envelope of the quadrupolar region due to the higher magnetic pressure above it (which comes from the stronger ambient field). Thus, the height of emergence of the envelope field is determined by the (strength of the) pre-existing magnetic field.

This result has an effect on the emission of jets, which are emitted due to reconnection between the two fields. When the ambient field is relatively weak, it is pushed away from the strong emerging field and reconnection between them is not so persistent. On the other hand, when the ambient field is relatively strong, we find that more jets are ejected due to more efficient and more frequent (over the time evolution of the system) reconnection between the emerging field and the ambient field. As a consequence, we find that more mass and flux is being transferred into the solar corona by the reconnection jets. Also, we find that there are more eruptions when the ambient field is stronger. These eruptions could be confined or ejective, which lead to "blowout" jets. However, we should notice that, especially for the ejective eruptions, the stronger ambient field can release the downward tension of the envelope field more easily but it can also remove flux from the eruptive core more efficiently. Therefore, if the ambient field is too strong, the field lines of the eruptive core could be reconnected completely by the ambient field, leading to severe deformation of the erupting flux rope.

An analysis of the flux, which is transferred into the corona by the jets, showed that the enthalpy flux is the most dominant term. Three terms were considered: the enthalpy flux, the Alfvén wave flux and the kinetic flux. We found that enthalpy flux is about 2-8 times greater than the kinetic flux during the emission of the "blowout" jets. The time evolution of the total energy flux carried by the jets showed that it is sufficient to provide the energy required to accelerate the high speed solar wind. This indicates that the "blowout" jets may play an important role in driving the

solar wind.

As mentioned already in Section 2.2, we should highlight that our numerical model does not include thermal conduction and radiative losses in the energy equation. This causes the heat to be localised, resulting in a higher temperature at various places, such as in regions of strong current sheets. However, we believe that the overall dynamical behaviour of the system (e.g. the onset of recurrent eruptive jets and their mechanism) will not be affected dramatically, by the inclusion of either heat conduction or radiation. To some extent, our hypothesis has been partially confirmed by Fang et al. (2014), who showed that the inclusion of thermal conduction in the energy equation in similar experiments, leads to the ejection of only a small amount of extra mass (not more than 10%, compared to the non-conductive case) into the corona during the emission of the "blowout" jets. Otherwise, they showed that the temporal/spatial evolution of the jets in the conductive and non-conductive cases is very similar.

In the future, it would be interesting to study various topics, which are related to the results of this Thesis. One topic is the nature of the eruptions in emerging flux regions with a quadrupolar configuration. Especially, the role of instabilities (e.g. the torus instability) as a driver of the eruptions. What is the exact mechanism that drives the initial eruption of the flux ropes? Do they become unstable from the beginning (just after their formation) or do they rise in a similar manner to the background emerging field and then they erupt due to a (e.g. break-out) reconnection mechanism?

Another topic to consider for a further study is the effect of the strength of the sub-photospheric field on the eruptions. One should examine whether there is a threshold for the energy of the emerging field (while it is already inside the convection zone), for which the eruptions are not confined but ejective. In this case, do the eruptions evolve into "blowout" jets? If not, does the erupting material account for a CME-like eruption? It will also be very interesting to study the effect of the other parameters, such as the initial flux, the wavelength of the density deficit perturbation, the initial height of the tube, etc., on the eruptions and jets that emanate from the quadrupolar region.

On this basis, an extremely useful study would be to explore what determines the frequency of eruptions and jets. Could one predict the number of eruptions and/or jets, which are triggered from the quadrupolar region over its evolution? One may assume that it is the initial amount of flux of the system that determines the energy, which is available to be spent for the powering of such phenomena. In addition, one can support the idea that activity in the region will continue as long as flux emergence continues. If flux emergence stops, the powering of eruptions and jets will stop too. These are key questions, which will hopefully be answered in the near future.

Bibliography

D. J. Acheson. Instability by magnetic buoyancy. Sol. Phys., 62:23–50, May 1979. doi: 10.1007/BF00150129.

M. Adams, A. C. Sterling, R. L. Moore, and G. A. Gary. A Small-scale Eruption Leading to a Blowout Macrospicule Jet in an On-disk Coronal Hole. ApJ, 783:11, March 2014. doi: 10.1088/0004-637X/783/1/11.

D. Alexander and L. Fletcher. High-resolution Observations of Plasma Jets in the Solar Corona. Sol. Phys., 190:167–184, December 1999. doi: 10.1023/A:1005213826793.

S. K. Antiochos, C. R. DeVore, and J. A. Klimchuk. A Model for Solar Coronal Mass Ejections. ApJ, 510:485–493, January 1999. doi: 10.1086/306563.

T.D. Arber, A.W. Longbottom, C.L. Gerrard, and A.M. Milne. A staggered grid, lagrangian-eulerian remap code for 3-d mhd simulations. *Journal of Computational Physics*, 171(1):151 – 181, 2001. ISSN 0021-9991. doi: http://dx.doi.org/10.1006/jcph.2001.6780. URL `http://www.sciencedirect.com/science/article/pii/S0021999101967804`.

V. Archontis and A. W. Hood. Flux emergence and coronal eruption. A&A, 514:A56, May 2010. doi: 10.1051/0004-6361/200913502.

V. Archontis and A. W. Hood. Magnetic flux emergence: a precursor of solar plasma expulsion. A&A, 537:A62, January 2012. doi: 10.1051/0004-6361/201116956.

V. Archontis and A. W. Hood. A Numerical Model of Standard to Blowout Jets. ApJ, 769:L21, June 2013. doi: 10.1088/2041-8205/769/2/L21.

V. Archontis and T. Török. Eruption of magnetic flux ropes during flux emergence. A&A, 492:L35–L38, December 2008. doi: 10.1051/0004-6361:200811131.

V. Archontis, F. Moreno-Insertis, K. Galsgaard, A. Hood, and E. O'Shea. Emergence of magnetic flux from the convection zone into the corona. A&A, 426:1047–1063, November 2004. doi: 10.1051/0004-6361:20035934.

V. Archontis, F. Moreno-Insertis, K. Galsgaard, and A. W. Hood. The Three-dimensional Interaction between Emerging Magnetic Flux and a Large-Scale Coronal Field: Reconnection, Current Sheets, and Jets. ApJ, 635:1299–1318, December 2005. doi: 10.1086/497533.

V. Archontis, K. Galsgaard, F. Moreno-Insertis, and A. W. Hood. Three-dimensional Plasmoid Evolution in the Solar Atmosphere. ApJ, 645:L161–L164, July 2006. doi: 10.1086/506203.

R. G. Athay, editor. *The solar chromosphere and corona: Quiet sun*, volume 53 of *Astrophysics and Space Science Library*, 1976. doi: 10.1007/978-94-010-1715-2.

E. H. Avrett. The Solar Temperature Minimum and Chromosphere. In A. A. Pevtsov and H. Uitenbroek, editors, *Current Theoretical Models and Future High Resolution Solar Observations: Preparing for ATST*, volume 286 of *Astronomical Society of the Pacific Conference Series*, page 419, 2003.

J. D. Bohlin, S. N. Vogel, J. D. Purcell, N. R. Sheeley, Jr., R. Tousey, and M. E. Vanhoosier. A newly observed solar feature - Macrospicules in He II 304 A. ApJ, 197:L133–L135, May 1975. doi: 10.1086/181794.

G. E. Brueckner and J.-D. F. Bartoe. High Velocity Jets in the "Quiet" Sun as a Possible Source of the Solar Wind and the Heating of the Corona. In *Bulletin of the American Astronomical Society*, volume 10 of BAAS, page 416, March 1978.

G. E. Brueckner and J.-D. F. Bartoe. Observations of high-energy jets in the corona above the quiet sun, the heating of the corona, and the acceleration of the solar wind. ApJ, 272:329–348, September 1983. doi: 10.1086/161297.

H. Chen, Y. Jiang, and S. Ma. An EUV Jet and Hα Filament Eruption Associated with Flux Cancelation in a Decaying Active Region. Sol. Phys., 255:79–90, March 2009. doi: 10.1007/s11207-008-9298-1.

H. D. Chen, Y. C. Jiang, and S. L. Ma. Observations of Hα surges and ultraviolet jets above satellite sunspots. A&A, 478:907–913, February 2008. doi: 10.1051/0004-6361:20078641.

J. W. Cirtain, L. Golub, L. Lundquist, A. van Ballegooijen, A. Savcheva, M. Shimojo, E. DeLuca, S. Tsuneta, T. Sakao, K. Reeves, M. Weber, R. Kano, N. Narukage, and K. Shibasaki. Evidence for Alfvén Waves in Solar X-ray Jets. *Science*, 318:1580, December 2007. doi: 10.1126/science.1147050.

J. L. Culhane, L. K. Harra, A. M. James, K. Al-Janabi, L. J. Bradley, R. A. Chaudry, K. Rees, J. A. Tandy, P. Thomas, M. C. R. Whillock, B. Winter, G. A. Doschek, C. M. Korendyke, C. M. Brown, S. Myers, J. Mariska, J. Seely, J. Lang, B. J. Kent, B. M. Shaughnessy, P. R. Young, G. M. Simnett, C. M. Castelli, S. Mahmoud, H. Mapson-Menard, B. J. Probyn, R. J. Thomas, J. Davila, K. Dere, D. Windt, J. Shea, R. Hagood, R. Moye, H. Hara, T. Watanabe, K. Matsuzaki, T. Kosugi, V. Hansteen, and Ø. Wikstol. The EUV Imaging Spectrometer for Hinode. Sol. Phys., 243:19–61, June 2007. doi: 10.1007/s01007-007-0293-1.

B. de Pontieu, S. McIntosh, V. H. Hansteen, M. Carlsson, C. J. Schrijver, T. D. Tarbell, A. M. Title, R. A. Shine, Y. Suematsu, S. Tsuneta, Y. Katsukawa, K. Ichimoto, T. Shimizu, and S. Nagata. A Tale of Two Spicules: The Impact of Spicules on the Magnetic Chromosphere. PASJ, 59: S655–S662, November 2007. doi: 10.1093/pasj/59.sp3.S655.

B. De Pontieu, S. W. McIntosh, M. Carlsson, V. H. Hansteen, T. D. Tarbell, P. Boerner, J. Martinez-Sykora, C. J. Schrijver, and A. M. Title. The Origins of Hot Plasma in the Solar Corona. *Science*, 331:55, January 2011. doi: 10.1126/science.1197738.

H. L. Demastus, W. J. Wagner, and R. D. Robinson. Coronal Disturbances. I: Fast Transient

Events Observed in the Green Coronal Emission Line During the Last Solar Cycle. Sol. Phys., 31:449–459, August 1973. doi: 10.1007/BF00152820.

K. P. Dere, E. Landi, P. R. Young, G. Del Zanna, M. Landini, and H. E. Mason. CHIANTI - an atomic database for emission lines. IX. Ionization rates, recombination rates, ionization equilibria for the elements hydrogen through zinc and updated atomic data. A&A, 498:915–929, May 2009. doi: 10.1051/0004-6361/200911712.

J.A. Eddy, R. Ise, and George C. Marshall Space Flight Center. *A new sun: the solar results from Skylab*. NASA SP. Scientific and Technical Information Office, National Aeronautics and Space Administration : for sale by the Supt. of Docs., U.S. Govt. Print. Off., 1979. URL `https://books.google.co.uk/books?id=S6jmS0B8NzsC`.

L.T. Elkins-Tanton. *The Sun, Mercury, and Venus*. Solar system. Chelsea House, 2006. ISBN 9780816051939. URL `https://books.google.co.uk/books?id=RD_ftwAACAAJ`.

T. Emonet and F. Moreno-Insertis. The Physics of Twisted Magnetic Tubes Rising in a Stratified Medium: Two-dimensional Results. ApJ, 492:804–821, January 1998. doi: 10.1086/305074.

C. R. Evans and J. F. Hawley. Simulation of magnetohydrodynamic flows - A constrained transport method. ApJ, 332:659–677, September 1988. doi: 10.1086/166684.

Y. Fan. The Emergence of a Twisted Ω-Tube into the Solar Atmosphere. ApJ, 554:L111–L114, June 2001. doi: 10.1086/320935.

Y. Fan. Magnetic Fields in the Solar Convection Zone. *Living Reviews in Solar Physics*, 1:1, July 2004.

F. Fang and Y. Fan. δ-Sunspot Formation in Simulation of Active-region-scale Flux Emergence. ApJ, 806:79, June 2015. doi: 10.1088/0004-637X/806/1/79.

F. Fang, Y. Fan, and S. W. McIntosh. Rotating Solar Jets in Simulations of Flux Emergence with Thermal Conduction. ApJ, 789:L19, July 2014. doi: 10.1088/2041-8205/789/1/L19.

K. Galsgaard, F. Moreno-Insertis, V. Archontis, and A. Hood. A Three-dimensional Study of Reconnection, Current Sheets, and Jets Resulting from Magnetic Flux Emergence in the Sun. ApJ, 618:L153–L156, January 2005. doi: 10.1086/427872.

K. Galsgaard, V. Archontis, F. Moreno-Insertis, and A. W. Hood. The Effect of the Relative Orientation between the Coronal Field and New Emerging Flux. I. Global Properties. ApJ, 666: 516–531, September 2007. doi: 10.1086/519756.

R. A. García, S. Turck-Chièze, S. J. Jiménez-Reyes, J. Ballot, P. L. Pallé, A. Eff-Darwich, S. Mathur, and J. Provost. Tracking Solar Gravity Modes: The Dynamics of the Solar Core. *Science*, 316:1591, June 2007. doi: 10.1126/science.1140598.

L. Golub, E. Deluca, G. Austin, J. Bookbinder, D. Caldwell, P. Cheimets, J. Cirtain, M. Cosmo, P. Reid, A. Sette, M. Weber, T. Sakao, R. Kano, K. Shibasaki, H. Hara, S. Tsuneta, K. Kumagai, T. Tamura, M. Shimojo, J. McCracken, J. Carpenter, H. Haight, R. Siler, E. Wright, J. Tucker, H. Rutledge, M. Barbera, G. Peres, and S. Varisco. The X-Ray Telescope (XRT) for the Hinode Mission. Sol. Phys., 243:63–86, June 2007. doi: 10.1007/s11207-007-0182-1.

G. E. Hale and S. B. Nicholson. *Magnetic observations of sunspots, 1917-1924 ...* 1938.

G. E. Hale, F. Ellerman, S. B. Nicholson, and A. H. Joy. The Magnetic Polarity of Sun-Spots. ApJ, 49:153, April 1919. doi: 10.1086/142452.

J. F. Hansen and P. M. Bellan. Experimental Demonstration of How Strapping Fields Can Inhibit Solar Prominence Eruptions. ApJ, 563:L183–L186, December 2001. doi: 10.1086/338736.

J. Heyvaerts, E. R. Priest, and D. M. Rust. An emerging flux model for the solar flare phenomenon. ApJ, 216:123–137, August 1977. doi: 10.1086/155453.

J. Hong, Y. Jiang, R. Zheng, J. Yang, Y. Bi, and B. Yang. A Micro Coronal Mass Ejection Associated Blowout Extreme-ultraviolet Jet. ApJ, 738:L20, September 2011. doi: 10.1088/2041-8205/738/2/L20.

R. Komm, S. Morita, R. Howe, and F. Hill. Emerging Active Regions Studied with Ring-Diagram Analysis. ApJ, 672:1254-1265, January 2008. doi: 10.1086/523998.

E. P. Kontar, I. G. Hannah, and A. L. MacKinnon. Chromospheric magnetic field and density structure measurements using hard X-rays in a flaring coronal loop. A&A, 489:L57–L60, October 2008. doi: 10.1051/0004-6361:200810719.

T. Kosugi, K. Matsuzaki, T. Sakao, T. Shimizu, Y. Sone, S. Tachikawa, T. Hashimoto, K. Minesugi, A. Ohnishi, T. Yamada, S. Tsuneta, H. Hara, K. Ichimoto, Y. Suematsu, M. Shimojo, T. Watanabe, S. Shimada, J. M. Davis, L. D. Hill, J. K. Owens, A. M. Title, J. L. Culhane, L. K. Harra, G. A. Doschek, and L. Golub. The Hinode (Solar-B) Mission: An Overview. Sol. Phys., 243:3–17, June 2007. doi: 10.1007/s11207-007-9014-6.

J. Krall, J. Chen, R. Santoro, D. S. Spicer, S. T. Zalesak, and P. J. Cargill. Simulation of Buoyant Flux Ropes in a Magnetized Solar Atmosphere. ApJ, 500:992–1002, June 1998. doi: 10.1086/305754.

H. Künzel. Zur Klassifikation von Sonnenfleckengruppen. *Astronomische Nachrichten*, 288:177, December 1965.

E. Landi, P. R. Young, K. P. Dere, G. Del Zanna, and H. E. Mason. CHIANTI - An Atomic Database for Emission Lines. XIII. Soft X-Ray Improvements and Other Changes. ApJ, 763:86, February 2013. doi: 10.1088/0004-637X/763/2/86.

J. E. Leake, M. G. Linton, and T. Török. Simulations of Emerging Magnetic Flux. I. The Formation of Stable Coronal Flux Ropes. ApJ, 778:99, December 2013. doi: 10.1088/0004-637X/778/2/99.

R. B. Leighton, R. W. Noyes, and G. W. Simon. Velocity Fields in the Solar Atmosphere. I. Preliminary Report. ApJ, 135:474, March 1962. doi: 10.1086/147285.

J. R. Lemen, A. M. Title, D. J. Akin, P. F. Boerner, C. Chou, J. F. Drake, D. W. Duncan, C. G. Edwards, F. M. Friedlaender, G. F. Heyman, N. E. Hurlburt, N. L. Katz, G. D. Kushner, M. Levay, R. W. Lindgren, D. P. Mathur, E. L. McFeaters, S. Mitchell, R. A. Rehse, C. J. Schrijver, L. A. Springer, R. A. Stern, T. D. Tarbell, J.-P. Wuelser, C. J. Wolfson, C. Yanari, J. A. Bookbinder, P. N. Cheimets, D. Caldwell, E. E. Deluca, R. Gates, L. Golub, S. Park, W. A. Podgorski, R. I. Bush, P. H. Scherrer, M. A. Gummin, P. Smith, G. Auker, P. Jerram, P. Pool, R. Soufli, D. L.

Windt, S. Beardsley, M. Clapp, J. Lang, and N. Waltham. The Atmospheric Imaging Assembly (AIA) on the Solar Dynamics Observatory (SDO). Sol. Phys., 275:17–40, January 2012. doi: 10.1007/s11207-011-9776-8.

C. Liu, N. Deng, R. Liu, I. Ugarte-Urra, S. Wang, and H. Wang. A Standard-to-blowout Jet. ApJ, 735:L18, July 2011. doi: 10.1088/2041-8205/735/1/L18.

W. Liu, T. E. Berger, A. M. Title, and T. D. Tarbell. An Intriguing Chromospheric Jet Observed by Hinode: Fine Structure Kinematics and Evidence of Unwinding Twists. ApJ, 707:L37–L41, December 2009. doi: 10.1088/0004-637X/707/1/L37.

D. W. Longcope, G. H. Fisher, and S. Arendt. The Evolution and Fragmentation of Rising Magnetic Flux Tubes. ApJ, 464:999, June 1996. doi: 10.1086/177387.

T. Magara. Dynamics of Emerging Flux Tubes in the Sun. ApJ, 549:608–628, March 2001. doi: 10.1086/319073.

T. Magara and D. W. Longcope. Sigmoid Structure of an Emerging Flux Tube. ApJ, 559:L55–L59, September 2001. doi: 10.1086/323635.

T. Magara and D. W. Longcope. Injection of Magnetic Energy and Magnetic Helicity into the Solar Atmosphere by an Emerging Magnetic Flux Tube. ApJ, 586:630–649, March 2003. doi: 10.1086/367611.

W. Manchester, IV, T. Gombosi, D. DeZeeuw, and Y. Fan. Eruption of a Buoyantly Emerging Magnetic Flux Rope. ApJ, 610:588–596, July 2004. doi: 10.1086/421516.

R. Matsumoto and K. Shibata. Three-dimensional MHD simulation of the Parker instability in galactic gas disks and the solar atmosphere. PASJ, 44:167–175, June 1992.

R. Matsumoto, T. Tajima, K. Shibata, and M. Kaisig. Three-dimensional magnetohydrodynamics of the emerging magnetic flux in the solar atmosphere. ApJ, 414:357–371, September 1993. doi: 10.1086/173082.

R. Matsumoto, T. Tajima, W. Chou, A. Okubo, and K. Shibata. Formation of a Kinked Alignment of Solar Active Regions. ApJ, 493:L43–L46, January 1998. doi: 10.1086/311116.

R. L. Moore, D. A. Falconer, J. G. Porter, and S. T. Suess. On Heating the Sun's Corona by Magnetic Explosions: Feasibility in Active Regions and Prospects for Quiet Regions and Coronal Holes. ApJ, 526:505–522, November 1999. doi: 10.1086/307969.

R. L. Moore, J. W. Cirtain, A. C. Sterling, and D. A. Falconer. Dichotomy of Solar Coronal Jets: Standard Jets and Blowout Jets. ApJ, 720:757–770, September 2010. doi: 10.1088/0004-637X/720/1/757.

R. L. Moore, A. C. Sterling, D. A. Falconer, and D. Robe. The Cool Component and the Dichotomy, Lateral Expansion, and Axial Rotation of Solar X-Ray Jets. ApJ, 769:134, June 2013. doi: 10.1088/0004-637X/769/2/134.

K. Moraitis, K. Tziotziou, M. K. Georgoulis, and V. Archontis. Validation and Benchmarking of a Practical Free Magnetic Energy and Relative Magnetic Helicity Budget Calculation in Solar Magnetic Structures. Sol. Phys., 289:4453–4480, December 2014. doi: 10.1007/s11207-014-0590-y.

F. Moreno-Insertis and T. Emonet. The Rise of Twisted Magnetic Tubes in a Stratified Medium. ApJ, 472:L53, November 1996. doi: 10.1086/310360.

F. Moreno-Insertis and K. Galsgaard. Plasma Jets and Eruptions in Solar Coronal Holes: A Three-dimensional Flux Emergence Experiment. ApJ, 771:20, July 2013. doi: 10.1088/0004-637X/771/1/20.

F. Moreno-Insertis, K. Galsgaard, and I. Ugarte-Urra. Jets in Coronal Holes: Hinode Observations and Three-dimensional Computer Modeling. ApJ, 673:L211, February 2008. doi: 10.1086/527560.

S. Morita and S. W. McIntosh. Genesis of AR NOAA10314. In K. Sankarasubramanian, M. Penn, and A. Pevtsov, editors, *Large-scale Structures and their Role in Solar Activity*, volume 346 of *Astronomical Society of the Pacific Conference Series*, page 317, December 2005.

D. Moses, F. Clette, J.-P. Delaboudinière, G. E. Artzner, M. Bougnet, J. Brunaud, C. Carabetian, A. H. Gabriel, J. F. Hochedez, F. Millier, X. Y. Song, B. Au, K. P. Dere, R. A. Howard, R. Kreplin, D. J. Michels, J. M. Defise, C. Jamar, P. Rochus, J. P. Chauvineau, J. P. Marioge, R. C. Catura, J. R. Lemen, L. Shing, R. A. Stern, J. B. Gurman, W. M. Neupert, J. Newmark, B. Thompson, A. Maucherat, F. Portier-Fozzani, D. Berghmans, P. Cugnon, E. L. van Dessel, and J. R. Gabryl. EIT Observations of the Extreme Ultraviolet Sun. Sol. Phys., 175:571–599, October 1997. doi: 10.1023/A:1004902913117.

G. Nisticò, V. Bothmer, S. Patsourakos, and G. Zimbardo. Characteristics of EUV Coronal Jets Observed with STEREO/SECCHI. Sol. Phys., 259:87–108, October 2009. doi: 10.1007/s11207-009-9424-8.

A. R. Paraschiv, A. Bemporad, and A. C. Sterling. Physical properties of solar polar jets. A statistical study with Hinode XRT data. A&A, 579:A96, July 2015. doi: 10.1051/0004-6361/201525671.

S. Parenti. Solar Prominences: Observations. *Living Reviews in Solar Physics*, 11, March 2014. doi: 10.12942/lrsp-2014-1.

E. Pariat, S. K. Antiochos, and C. R. DeVore. A Model for Solar Polar Jets. ApJ, 691:61–74, January 2009. doi: 10.1088/0004-637X/691/1/61.

E. N. Parker. *Cosmical magnetic fields: Their origin and their activity*. 1979.

S. Patsourakos, E. Pariat, A. Vourlidas, S. K. Antiochos, and J. P. Wuelser. STEREO SECCHI Stereoscopic Observations Constraining the Initiation of Polar Coronal Jets. ApJ, 680:L73, June 2008. doi: 10.1086/589769.

W. D. Pesnell, B. J. Thompson, and P. C. Chamberlin. The Solar Dynamics Observatory (SDO). Sol. Phys., 275:3–15, January 2012. doi: 10.1007/s11207-011-9841-3.

W. O. Roberts. A Preliminary Report on Chromospheric Spicules of Extremely Short Lifetime. ApJ, 101:136, March 1945. doi: 10.1086/144699.

I. Sammis, F. Tang, and H. Zirin. The Dependence of Large Flare Occurrence on the Magnetic Structure of Sunspots. ApJ, 540:583–587, September 2000. doi: 10.1086/309303.

A. Savcheva, J. Cirtain, E. E. Deluca, L. L. Lundquist, L. Golub, M. Weber, M. Shimojo,

K. Shibasaki, T. Sakao, N. Narukage, S. Tsuneta, and R. Kano. A Study of Polar Jet Parameters Based on Hinode XRT Observations. PASJ, 59:S771–S778, November 2007. doi: 10.1093/pasj/59.sp3.S771.

P. H. Scherrer, R. S. Bogart, R. I. Bush, J. T. Hoeksema, A. G. Kosovichev, J. Schou, W. Rosenberg, L. Springer, T. D. Tarbell, A. Title, C. J. Wolfson, I. Zayer, and MDI Engineering Team. The Solar Oscillations Investigation - Michelson Doppler Imager. Sol. Phys., 162:129–188, December 1995. doi: 10.1007/BF00733429.

B. Schmieder, Y. Guo, F. Moreno-Insertis, G. Aulanier, L. Yelles Chaouche, N. Nishizuka, L. K. Harra, J. K. Thalmann, S. Vargas Dominguez, and Y. Liu. Twisting solar coronal jet launched at the boundary of an active region. A&A, 559:A1, November 2013. doi: 10.1051/0004-6361/201322181.

C. J. Schrijver. Driving major solar flares and eruptions: A review. *Advances in Space Research*, 43:739–755, March 2009. doi: 10.1016/j.asr.2008.11.004.

C. J. Schrijver, G. Aulanier, A. M. Title, E. Pariat, and C. Delannée. The 2011 February 15 X2 Flare, Ribbons, Coronal Front, and Mass Ejection: Interpreting the Three-dimensional Views from the Solar Dynamics Observatory and STEREO Guided by Magnetohydrodynamic Flux-rope Modeling. ApJ, 738:167, September 2011. doi: 10.1088/0004-637X/738/2/167.

M. Schuessler. Magnetic buoyancy revisited - Analytical and numerical results for rising flux tubes. A&A, 71:79–91, January 1979.

A. Secchi. *Le soleil: texte*. Number pt. 2. Gauthier-Villars, 1877. URL `https://books.google.co.uk/books?id=8Z1JnQEACAAJ`.

Y. Shen, Y. Liu, J. Su, and Y. Deng. On a Coronal Blowout Jet: The First Observation of a Simultaneously Produced Bubble-like CME and a Jet-like CME in a Solar Event. ApJ, 745: 164, February 2012. doi: 10.1088/0004-637X/745/2/164.

K. Shibata and Y. Uchida. A magnetodynamic mechanism for the formation of astrophysical jets. I - Dynamical effects of the relaxation of nonlinear magnetic twists. PASJ, 37:31–46, 1985.

K. Shibata, T. Tajima, R. Matsumoto, T. Horiuchi, T. Hanawa, R. Rosner, and Y. Uchida. Nonlinear Parker instability of isolated magnetic flux in a plasma. ApJ, 338:471–492, March 1989a. doi: 10.1086/167212.

K. Shibata, T. Tajima, R. S. Steinolfson, and R. Matsumoto. Two-dimensional magnetohydrodynamic model of emerging magnetic flux in the solar atmosphere. ApJ, 345:584–596, October 1989b. doi: 10.1086/167932.

K. Shibata, Y. Ishido, L. W. Acton, K. T. Strong, T. Hirayama, Y. Uchida, A. H. McAllister, R. Matsumoto, S. Tsuneta, T. Shimizu, H. Hara, T. Sakurai, K. Ichimoto, Y. Nishino, and Y. Ogawara. Observations of X-ray jets with the YOHKOH Soft X-ray Telescope. PASJ, 44: L173–L179, October 1992a.

K. Shibata, S. Nozawa, and R. Matsumoto. Magnetic reconnection associated with emerging magnetic flux. PASJ, 44:265–272, June 1992b.

K. Shibata, N. Nitta, K. T. Strong, R. Matsumoto, T. Yokoyama, T. Hirayama, H. Hudson, and

Y. Ogawara. A gigantic coronal jet ejected from a compact active region in a coronal hole. ApJ, 431:L51–L53, August 1994. doi: 10.1086/187470.

K. Shibata, T. Yokoyama, and M. Shimojo. Coronal X-ray jets observed with Yohkoh/SXT. *Advances in Space Research*, 17, 1996. doi: 10.1016/0273-1177(95)00567-X.

M. Shimojo, S. Hashimoto, K. Shibata, T. Hirayama, H. S. Hudson, and L. W. Acton. Statistical Study of Solar X-Ray Jets Observed with the YOHKOH Soft X-Ray Telescope. PASJ, 48: 123–136, February 1996. doi: 10.1093/pasj/48.1.123.

M. Shimojo, K. Shibata, and K. L. Harvey. Magnetic Field Properties of Solar X-Ray Jets. Sol. Phys., 178:379–392, 1998. doi: 10.1023/A:1005091905214.

A. C. Sterling, R. L. Moore, D. A. Falconer, and M. Adams. Small-scale filament eruptions as the driver of X-ray jets in solar coronal holes. Nature, 523:437–440, July 2015. doi: 10.1038/nature14556.

X. Sun, J. T. Hoeksema, Y. Liu, T. Wiegelmann, K. Hayashi, Q. Chen, and J. Thalmann. Evolution of Magnetic Field and Energy in a Major Eruptive Active Region Based on SDO/HMI Observation. ApJ, 748:77, April 2012. doi: 10.1088/0004-637X/748/2/77.

S. Takasao, Y. Fan, M. C. M. Cheung, and K. Shibata. Numerical Study on the Emergence of Kinked Flux Tube for Understanding of Possible Origin of δ-spot Regions. ApJ, 813:112, November 2015. doi: 10.1088/0004-637X/813/2/112.

S. Toriumi, Y. Iida, K. Kusano, Y. Bamba, and S. Imada. Formation of a Flare-Productive Active Region: Observation and Numerical Simulation of NOAA AR 11158. Sol. Phys., 289:3351–3369, September 2014. doi: 10.1007/s11207-014-0502-1.

S. Tsuneta, L. Acton, M. Bruner, J. Lemen, W. Brown, R. Caravalho, R. Catura, S. Freeland, B. Jurcevich, M. Morrison, Y. Ogawara, T. Hirayama, and J. Owens. The Soft X-ray Telescope for the SOLAR-A Mission. Sol. Phys., 136:37–67, November 1991. doi: 10.1007/BF00151694.

B. van Leer. Towards the ultimate conservative difference scheme. V - A second-order sequel to Godunov's method. *Journal of Computational Physics*, 32:101–136, July 1979. doi: 10.1016/0021-9991(79)90145-1.

Y.-M. Wang and N. R. Sheeley, Jr. Coronal White-Light Jets near Sunspot Maximum. ApJ, 575: 542–552, August 2002. doi: 10.1086/341145.

Y.-M. Wang, N. R. Sheeley, Jr., D. G. Socker, R. A. Howard, G. E. Brueckner, D. J. Michels, D. Moses, O. C. St. Cyr, A. Llebaria, and J.-P. Delaboudinière. Observations of Correlated White-Light and Extreme-Ultraviolet Jets from Polar Coronal Holes. ApJ, 508:899–907, December 1998. doi: 10.1086/306450.

M. L. Wilkins. Use of artificial viscosity in multidimensional fluid dynamic calculations. *Journal of Computational Physics*, 36:281–303, July 1980. doi: 10.1016/0021-9991(80)90161-8.

G. L. Withbroe, D. T. Jaffe, P. V. Foukal, M. C. E. Huber, R. W. Noyes, E. M. Reeves, E. J. Schmahl, J. G. Timothy, and J. E. Vernazza. Extreme-ultraviolet transients observed at the solar pole. ApJ, 203:528–532, January 1976. doi: 10.1086/154108.

J.-P. Wuelser, J. R. Lemen, T. D. Tarbell, C. J. Wolfson, J. C. Cannon, B. A. Carpenter, D. W.

Duncan, G. S. Gradwohl, S. B. Meyer, A. S. Moore, R. L. Navarro, J. D. Pearson, G. R. Rossi, L. A. Springer, R. A. Howard, J. D. Moses, J. S. Newmark, J.-P. Delaboudiniere, G. E. Artzner, F. Auchere, M. Bougnet, P. Bouyries, F. Bridou, J.-Y. Clotaire, G. Colas, F. Delmotte, A. Jerome, M. Lamare, R. Mercier, M. Mullot, M.-F. Ravet, X. Song, V. Bothmer, and W. Deutsch. EUVI: the STEREO-SECCHI extreme ultraviolet imager. In S. Fineschi and M. A. Gummin, editors, *Telescopes and Instrumentation for Solar Astrophysics*, volume 5171 of Proc. SPIE, pages 111–122, February 2004. doi: 10.1117/12.506877.

T. Yokoyama and K. Shibata. Magnetic reconnection as the origin of X-ray jets and Hα surges on the Sun. Nature, 375:42–44, May 1995. doi: 10.1038/375042a0.

T. Yokoyama and K. Shibata. Numerical Simulation of Solar Coronal X-Ray Jets Based on the Magnetic Reconnection Model. PASJ, 48:353–376, April 1996. doi: 10.1093/pasj/48.2.353.

P. R. Young and K. Muglach. Solar Dynamics Observatory and Hinode Observations of a Blowout Jet in a Coronal Hole. Sol. Phys., 289:3313–3329, September 2014. doi: 10.1007/s11207-014-0484-z.